Light propagation in an inhomogeneous universe

A thesis
submitted for the Degree
of
Doctor of Philosophy in Physics
in the
University of Canterbury

by

Hamish Rose

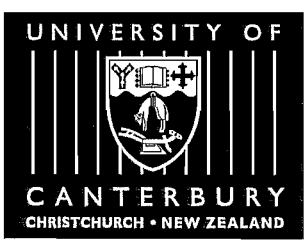

University of Canterbury
2002

Abstract

This thesis examines the effect of inhomogeneities on the magnitude-redshift relationship, focusing particularly on the redshift.

We show that a perturbed FRW universe which has the same global behaviour as an exact FRW universe does not have the same light propagation behaviour due to the relationship between redshift and the radial coordinate being influenced by the inhomogeneities introduced. The change in redshift along a light beam depends on the rate of expansion of space so an understanding of the effect of inhomogeneities on the local rate of expansion of space is necessary in order to study the effect of inhomogeneities on redshift.

We create a new description of the evolution of matter fluctuations in the weakly non-linear regime which also describes a relationship between the matter density and the local expansion rate of space. This is subsequently used in the development of a new method of calculating the relationship between the angular diameter distance and the redshift of a distant object.

We use the new magnitude-redshift relationship in conjunction with the supernovæ data to estimate cosmological parameters and find that

- to a high level of confidence Ω_Λ is non-zero
- the most likely flat universe is one with cosmological parameters close to $\{\Omega_m, \Omega_\Lambda\} = \{0.3, 0.7\}$.

Acknowledgements

I would like to thank my supervisor Jenni Adams for all her help and support. Thanks are also due to William Joyce, Suruj Seunarine, Lewis Ryder for helpful comments, particularly regarding the work contained in chapter 3, Michael Albrow for setting me right on statistical matters, Bryn Currie, Bevan Cresswell, Oliver Dickie and Pauline Harris for a multitude of distractions as well as some enlightening discussions and to UG1 for providing the light entertainment. I am very grateful to Saskia, especially for her encouragement to finish.

Contents

Figures x

Tables xi

1 Introduction **1**

1.1 General Relativity notation 6

1.2 Gravitational Lensing 7

1.2.1 Lens planes 7

1.2.2 Direct Integration 9

1.3 Universe models commonly used to study gravitational lensing . . 10

1.3.1 Swiss - Cheese Universe 11

1.3.2 Perturbed FRW Universe 12

1.3.3 Lemaître-Tolman Universe 12

1.4 Inhomogeneities and redshift 13

1.5 Outline of thesis 15

2 Cosmological parameter extraction using supernovæ **17**

2.1 Introduction 17

2.2 Description of data and analysis 17

2.3 Dependence of results on intermediate redshift supernovæ 22

2.3.1 Simulating additional supernovæ at intermediate redshift . 25

2.3.2 Lowering the mean magnitude of supernovæ at intermediate redshifts 26

2.3.3 Raising the mean magnitude of supernovæ at intermediate redshifts 27

2.3.4 Summary 28

2.4 Conclusions 29

3 Flux Conservation **31**

3.1 Introduction 31

3.2 Photon number count versus coordinate distance 32

3.3 Apparent magnitude versus redshift 33

3.4 Discussion 36

4 Geodesic Deviation **38**

4.1 Mathematical Preliminaries 39

4.2 Timelike Curves 40

4.2.1 Synchronous Gauge 42

4.3 Null Curves 43

4.3.1 Distance Measurements 48

5 Distribution of Matter Inhomogeneities **50**

5.1 Introduction 50

5.2 Matter Power Spectrum 51

5.3 Non-linear evolution of the power spectrum 51

5.4 Computation 60

6 A new method of calculating the luminosity distance 63

6.1 Introduction 63

6.2 Differential equation used to find the luminosity distance 64

6.3 Lookback time - redshift relationship 69

6.4 Magnitude - redshift relationship 73

6.5 Cosmological parameter extraction with lensing 77

6.6 Conclusions 86

7 Conclusions 88

References 91

List of Figures

1.1 Luminosity distance 4

1.2 Angular diameter distance 4

1.3 Wavefront area in different geometries 5

2.1 Supernova magnitudes 19

2.2 Contour plot with $1\sigma - 4\sigma$ confidence regions for all 93 data points 21

2.3 Magnitude – redshift plot showing variation in magnitude possible for $\{0.0 \leq \Omega_m \leq 1.0, 0.0 \leq \Omega_\Lambda \leq 1.0\}$. Also plotted are data points 22

2.4 Supernova magnitudes and binned data points 23

2.5 Confidence regions simulating more supernovæ observations . . . 26

2.6 Confidence regions simulating more supernovæ observations with lower mean magnitudes 28

2.7 As for Figure 2.6 but with the mean raised rather than lowered . 29

4.1 Deviation vectors to the same nearby geodesic differ by a multiple of k 44

4.2 Ricci focusing of light beams 48

5.1 Evolution of density fluctuations. Primordial fluctuation is plotted against fluctuation at current time 54

5.2 Local expansion rate relative to FRW expansion rate as a function of $\delta(t_0)$ 55

5.3 Current matter distribution with $\{\Omega_m, \Omega_\Lambda\} = \{1.0, 0.0\}$ 56

5.4 Current matter distribution scaled with relative volumes and with a log-normal curve fitted to the distribution 57

5.5 Current distribution of local expansion rates for cosmological parameters $\{\Omega_m, \Omega_\Lambda\} = \{1.0, 0.0\}$ 58

5.6 Current matter distribution and best fit log-normal curve for cosmological parameters $\{\Omega_m, \Omega_\Lambda\} = \{1, 1\}$ 58

5.7 Current matter distribution for universe with cosmological parameters $\{\Omega_m, \Omega_\Lambda\} = \{1, 0\}$. 62

5.8 Current expansion rate distribution for cosmological parameters $\{\Omega_m, \Omega_\Lambda\} = \{1, 0\}$ 62

6.1 Difference in light travel time to a source at $z = 1$ between a FRW universe and a universe with 0.1 of matter in clumps ($\alpha = 0.9$) . . 71

6.2 As for figure 6.1 but with $\alpha = 0.5$ 71

6.3 Magnitude difference for a source at $z = 1$ between the FRW calculated value and the modified Dyer-Roeder calculated value with $\alpha = 0.9$ 72

6.4 As for figure 6.3 but with $\alpha = 0.5$ 72

6.5 Difference between FRW magnitude and Dyer-Roeder magnitude with $\alpha = 0.9$ for a source at $z = 1$ 73

6.6 As for figure 6.5 but with $\alpha = 0.5$ 73

6.7 Histogram plot showing frequency of lensed magnitudes relative to the FRW magnitude at $z = 0.6$ for a $\{\Omega_m, \Omega_\Lambda\} = \{0.3, 0.7\}$ universe 74

6.8 Histogram plot showing frequency of lensed magnitudes relative to the FRW magnitude at $z = 0.6$ for a $\{\Omega_m, \Omega_\Lambda\} = \{0.8, 1.7\}$ universe 75

6.9 Histogram plot showing frequency of lensed magnitudes relative to the FRW magnitude at $z = 1.0$ for a $\{\Omega_m, \Omega_\Lambda\} = \{0.8, 1.7\}$ universe 75

6.10 Difference between mean lensed magnitude and FRW magnitude at $z = 0.6$ 76

6.11 Difference between mean lensed magnitude and FRW magnitude at $z = 1.0$ 76

6.12 Standard deviation in m_{lensed} at $z = 0.6$ 76

6.13 Standard deviation in m_{lensed} at $z = 1.0$ 76

6.14 Magnitude-redshift plot showing the best overall fit with lensed magnitudes 78

6.15 Magnitude-redshift plot showing the best fit flat curves with lensed magnitudes 79

6.16 Contour plot showing 1σ to 4σ confidence regions for Ω_m and Ω_Λ calculated using lensed magnitudes with various values for $\mathcal{V}_{CMB}$. 81

6.17 As for figure 6.16 but not including model uncertainties in the χ^2 calculation 81

6.18 Contour plot showing 1σ to 4σ confidence regions for Ω_m and Ω_Λ calculated using the modified Dyer-Roeder distance with various values for α and with $\mathcal{V}_{CMB} = 10^{-6}$ 84

6.19 As for figure 6.18 but not including model uncertainties in the χ^2 calculation 85

6.20 Contour plot showing 1σ to 4σ confidence regions for Ω_m and Ω_Λ calculated using the modified Dyer-Roeder distance with various values for α and with $\mathcal{V}_{CMB} = 10^{-7}$ 85

6.21 As for figure 6.20 but not including model uncertainties in the χ^2 calculation 86

List of Tables

2.1 Supernovæ bins 24

2.2 Most likely cosmological parameters and χ^2_ν for binned data and for binned data simulating more supernovæ observations 25

2.3 Most likely cosmological parameters and χ^2_ν for binned data and for binned data simulating more supernovæ observations which lower the mean magnitude 27

2.4 Most likely cosmological parameters and χ^2_ν for binned data and for binned data simulating more supernovæ observations which raise the mean magnitude 29

5.1 Standard deviation of matter fluctuations for various cosmological parameters and $\mathcal{V}_{CMB}$ 60

6.1 Best fit values of Ω_m and Ω_Λ overall; for a flat universe; and for a $\Omega_\Lambda = 0$ universe with lensing taken into account 80

6.2 Best fit values of Ω_m and Ω_Λ overall and for a flat universe calculated according to the modified Dyer-Roeder distance 83

Chapter 1

Introduction

In observational cosmology it is very important to know how far away the objects being observed are. Unfortunately this apparently simple quantity is rather difficult to determine. For a start in general relativity there is no natural way to define a distance so there are a multitude of different distance definitions. Furthermore the distance determined from a given observational quantity will depend on the assumptions made about the geometry and matter distribution of the universe. Hogg (1999) contains an excellent discussion of the various types of distance indicators in use. In this thesis the luminosity distance is the primary distance indicator discussed and in particular its determination in an inhomogeneous universe.

Exciting results have recently been obtained using the luminosity distance to probe aspects of our model of the universe. The standard cosmological model is the Hot Big Bang universe which states that the universe is expanding and cooling. The Hot Big Bang universe is represented by the Friedmann-Robertson-Walker (FRW) model (Peebles, 1993) which has a time-dependent scale factor, allowing the universe to currently be expanding, and which assumes that the universe is spatially homogeneous and isotropic on large scales.

The observed expansion of the universe (Hubble, 1929) is one of the observational pillars of the Hot Big Bang model. Other observed phenomena which support the Hot Bang Bang universe are the Cosmic Microwave Background radiation (CMB) and the relative abundances of light elements (Peacock, 1999). The CMB

is blackbody radiation reaching us from all directions from the time when the universe cooled enough to allow protons and electrons to combine to form hydrogen atoms and thus became transparent. The radiation has cooled further as it has travelled through the universe. It is evidence for the Big Bang universe as it is additional evidence that the universe is expanding and cooling and because it is highly isotropic.

The Robertson-Walker metric used to describe the FRW universe is

$$\mathrm{d}s^2 = -c^2\mathrm{d}t^2 + a(t)^2\left[\frac{\mathrm{d}r^2}{1-kr^2} + r^2\left(\mathrm{d}\theta^2 + \sin^2\theta\mathrm{d}\psi^2\right)\right] \tag{1.1}$$

where $k = 0$ if the universe is spatially flat, $k = -1$ if it has negative curvature or $k = 1$ if the universe has positive curvature.

If the Robertson-Walker metric is used with the Einstein field equations and the matter content is assumed to be pressureless dust, the Friedmann equation may be obtained,

$$\left(\frac{\dot{a}}{a}\right)^2 = H_0^2\left(\frac{\Omega_m}{a^3} - \frac{kc^2}{a^2H_0^2} + \Omega_\Lambda\right), \tag{1.2}$$

where the scale factor a is normalised to $a = 1$ at the present time, H_0 is Hubble's constant, the present expansion rate of the universe, Ω_m and Ω_Λ have the standard definitions for the current contributions to the energy density of the universe,

$$\Omega_m = \frac{8\pi G\rho_0}{3H_0^2} \qquad \Omega_\Lambda = \frac{\Lambda c^2}{3H_0^2} \tag{1.3}$$

and ρ_0 is the current matter density. The cosmological constant, Λ (Carroll *et al.*, 1992), was originally introduced by Einstein to allow for the possibility of a static universe but later rejected by him. It is generally included as a parameter in modern cosmology and is interpreted as the vacuum energy density. One of the most compelling measurements of a non-zero cosmological constant is the supernovæ experiments (Perlmutter *et al.*, 1998; Riess *et al.*, 1998) which are discussed in chapter 2. The cosmological parameters Ω_m and Ω_Λ are defined so as to represent the current fractions of the critical density required for the universe to be flat – if $\Omega_m + \Omega_\Lambda = 1$ then the universe is spatially flat and $k = 0$. The FRW model is completely specified by setting the three parameters, Ω_m, Ω_Λ

and H_0. Since the real universe is not exactly homogeneous the expansion rate of space may vary from point to point so that H_0 is a local parameter.

The expansion of the universe gives rise to the cosmological redshift whereby the spectral lines in the light of distant galaxies are shifted toward the red end of the spectrum. The change in wavelength of any spectral line between emission and absorption depends on the degree to which the intervening space expands. In an exact FRW universe where the expansion rate is uniform, the redshift is related to the scale factor at absorption, $a(t_0)$, and emission, $a(t_e)$, according to the equation

$$1 + z = \frac{a(t_0)}{a(t_e)}. \tag{1.4}$$

The variation of any distance indicator with redshift can be used to constrain some of the cosmological parameters which describe any particular model of the universe.

Two distance indicators commonly used are the luminosity distance, d_L, (figure 1.1) and the angular diameter distance, d_A, (figure 1.2). The luminosity distance is the distance an astronomer infers an object to be at from its observed luminosity, given that the object's intrinsic luminosity is known. Angular diameter distance is the distance an extended object must be at for it to subtend the solid angle that it does. In this case the object's actual size must be known. In a static, Euclidean space the luminosity distance and the angular diameter distance are identical but in cosmology they satisfy the reciprocity relationship (Schneider *et al.*, 1992),

$$d_L = (1 + z)^2 d_A. \tag{1.5}$$

The two distances are not identical because the luminosity depends on the energy per unit time of the source whereas the angular diameter distance does not. One factor of $1 + z$ is due to each photon in the beam having lower energy at the observer than at the source and the other factor is due to a decreased rate of emission relative to reception.

The luminosity distance is defined to be $d_L = \sqrt{\frac{S}{4\pi L}}$ for a source of intrinsic luminosity S and observed luminosity L. This is in direct analogy with the

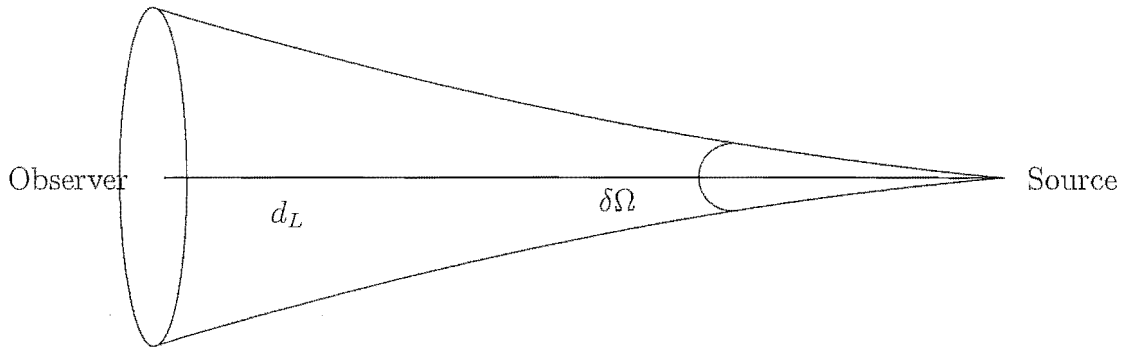

Figure 1.1: Luminosity distance

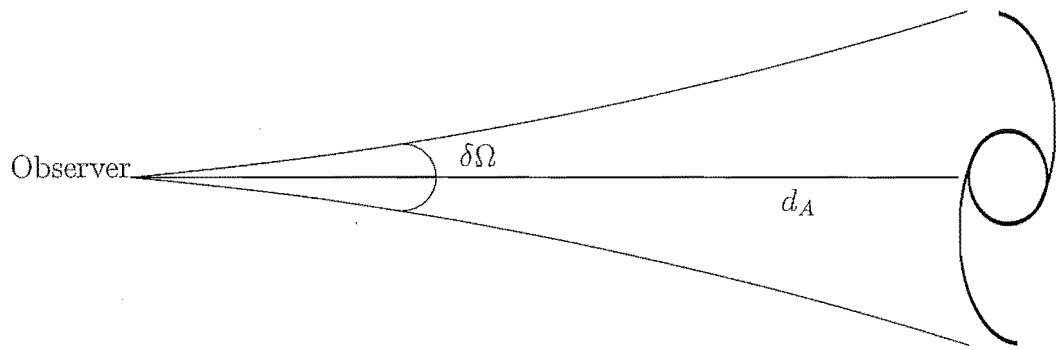

Figure 1.2: Angular diameter distance

standard expression in Euclidean space, $L = S/4\pi d^2$, for how luminosity decreases with distance. The smaller the cross-sectional area of the beam for a given solid angle subtended $\delta\Omega$, the brighter the source appears to be. A brighter source corresponds to a lower distance measurement so if something should cause the beam to be focused along its path, the luminosity distance will decrease relative to the same source with no focusing.

The luminosity distance is affected by the large scale curvature of the universe and by the local matter distribution that the light passes through. The contribution from the local matter distribution is called gravitational lensing. The effect that large scale curvature has on the luminosity distance can be understood by looking at figure 1.3. Consider a galaxy at point s_1 in a two-dimensional flat universe, F, and a galaxy at point s_2 in a two-dimensional spherical universe, S. An observer at the point o is clearly at a greater coordinate distance from s_2 than from s_1, but

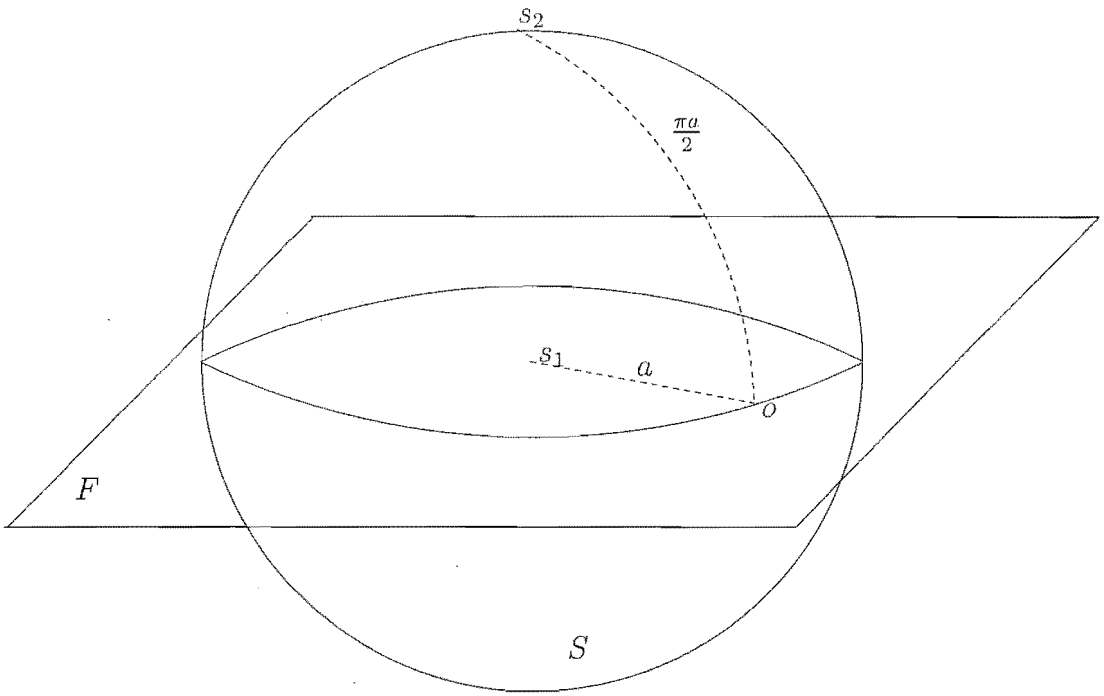

Figure 1.3: Wavefront area in different geometries

would assign the same luminosity distance to each galaxy since the wavefronts from each galaxy have the same area as they cross the observer. It is the effect that large scale curvature has on the luminosity distance that makes that distance measurement useful for determining cosmological parameters.

This is the technique used by the High-z Supernova team and the Supernova Cosmology team (Schmidt *et al.*, 1998; Perlmutter *et al.*, 1998), described in greater detail in chapter 2. By comparing the observed luminosity of supernovæ to theoretical luminosities in universes with different values of Ω_m and Ω_Λ, they show that the best fit to a flat universe is $\Omega_\Lambda \approx 0.7, \Omega_m \approx 0.3$.

The remainder of this chapter is primarily devoted to the methods used to study the propagation of light in an inhomogeneous universe. Section 1.1 contains a brief description of the notation used in this thesis. Section 1.2 describes common methods used to calculate the direct influence of matter on a beam of light and also reviews research which has used some of the approaches described. Section

1.3 lists some of the universe models used to study light propagation. Section 1.4 describes studies which investigate the effect of inhomogeneities on the redshift of distant objects, a subject which is the main focus of this thesis. Finally, section 1.5 outlines the following chapters.

1.1 General Relativity notation

This section describes briefly the notation and symbols used in this thesis when discussing general relativity.

The metric convention $(-+++)$ is used everywhere. Vectorial components are indexed using either Greek indices (μ, ν, λ, π etc.) which may take four values or Roman indices which are restricted to three. Repeated indices in any term are summed over. Commas indicate ordinary derivatives, so that

$$u^{\mu}{}_{,\nu} = \frac{\mathrm{d}u^{\mu}}{\mathrm{d}x^{\nu}}. \tag{1.6}$$

The covariant derivative is indicated with either a semi-colon or a capital 'D' on the derivative, so that

$$u^{\mu}{}_{;\nu} \equiv \frac{\mathrm{D}u^{\mu}}{\mathrm{d}x^{\nu}} = \frac{\mathrm{d}u^{\mu}}{\mathrm{d}x^{\nu}} + \Gamma^{\mu}{}_{\pi\nu}u^{\pi} \tag{1.7}$$

with $\Gamma^{\mu}{}_{\pi\nu}$ the Christoffel symbol.

The Riemann tensor, describing curvature, is denoted $R^{\mu}{}_{\nu\lambda\pi}$. The trace of the Riemann tensor is the Ricci tensor,

$$R^{\mu}{}_{\nu} = R^{\mu\pi}{}_{\pi\nu} \tag{1.8}$$

which may be contracted once again to form the Ricci scalar,

$$R = R^{\mu}{}_{\mu}. \tag{1.9}$$

The trace-free part of the Riemann tensor is the Weyl tensor,

$$C_{\mu\nu\lambda\pi} = R_{\mu\nu\lambda\pi} - \frac{R}{6}\left(g_{\mu\pi}g_{\nu\lambda} - g_{\mu\lambda}g_{\nu\pi}\right) - \frac{1}{2}\left(g_{\mu\lambda}R_{\nu\pi} - g_{\mu\pi}R_{\nu\lambda} - g_{\nu\lambda}R_{\mu\pi} + g_{\nu\pi}R_{\mu\lambda}\right). \tag{1.10}$$

The Weyl tensor is zero in conformally flat spacetimes such as the Friedmann Robertson Walker (FRW) universe. In general it is nonzero in the presence of inhomogeneities.

The energy-momentum tensor is $T^{\mu\nu}$. For all applications considered here, the universe is in a matter dominated period and the matter content is pressureless dust so the energy-momentum tensor, as measured by an observer with 4-velocity u^{μ}, is

$$T^{\mu\nu} = \rho c^2 u^{\mu} u^{\nu}. \tag{1.11}$$

The Einstein field equations,

$$R^{\mu\nu} - \frac{1}{2} R g^{\mu\nu} + \Lambda g^{\mu\nu} = \frac{8\pi G}{c^4} T^{\mu\nu}, \tag{1.12}$$

where G is Newton's gravitational constant and c is the speed of light, describe how the curvature tensors and the energy momentum tensor are connected.

1.2 Gravitational Lensing

When photons pass near a massive object they feel a gravitational force attracting them to it, just as matter does. The light ray is deflected by the massive object, analogously to the way a glass lens can deflect light. A massive body that deflects light is therefore called a gravitational lens. The gravitational lens can brighten images and if the lens is close to the straight line between the source and observer, multiple images can be formed.

There are two frameworks within which effect of inhomogeneities on light propagation is studied, the first of which uses lens planes at the location of massive bodies and the second of which uses direct integration of the equations that describe the histories of neighbouring photons.

1.2.1 Lens planes

The results in this section are from Schneider *et al.* (1992). Gravitational lensing calculations are performed by considering the lensing mass to be contained in a plane tangent to the straight line from the source to the observer. The ray is

considered to travel in a straight line before and after it hit the lens plane. All the deflection is assumed to occur at a point: the light turns a sharp corner. This is considered a good approximation, since the region in which the potential is strong enough to appreciably deflect the light is infinitesimal compared to the distances between the source and the lensing event and between the lensing event and the observer. The Newtonian potential on the plane is calculated, and the deflection angle α of the beam due to the potential can then be determined. For a point mass, the deflection angle is

$$\alpha = \frac{4GM}{c^2\xi} \tag{1.13}$$

where ξ is the distance between the lens and the light beam in the lens plane. For a general lens, the bending angle is a two dimensional vector

$$\boldsymbol{\alpha}(\boldsymbol{\xi}) = \frac{4G}{c^2}\int_{\mathbb{R}^2}\Sigma(\boldsymbol{\xi}')\frac{\boldsymbol{\xi}-\boldsymbol{\xi}'}{|\boldsymbol{\xi}-\boldsymbol{\xi}'|^2}d^2\boldsymbol{\xi}' \tag{1.14}$$

where $\Sigma(\boldsymbol{\xi})$ is the surface mass density on the lens plane obtained by "squeezing" all the mass of the lens into one plane.

Although the lens plane method is designed to describe a single strong lensing event, it is also used to describe continuous weak lensing by using many lens planes (Tomita *et al.*, 1999). In the multi-lens plane method, the region from the source to the observer is divided into a fixed number of planes perpendicular to the line of sight. It is assumed that lensing only occurs in these planes. Matter is distributed in these planes either randomly (Schneider and Weiss, 1988) or using an N-body simulation of, for example, a CDM (Cold Dark Matter) scenario (Wambsganss *et al.*, 1998). The route that a bundle of rays take through the universe is then calculated. In this way an image of an extended source can be constructed.

The lens plane method allows the source to pass through caustics, points where the amplification of the image goes to infinity. When the source passes near a caustic, multiple images can appear which are often quite distorted. Of course, we do not observe any objects which have been infinitely amplified. This apparent contradiction can be resolved by using a wave optics derivation instead of the geometric optics derivation used in the lens plane method as presented here. A wave

optics approach does not result in an infinite magnification due to interference effects. We do, however, observe multiple images of some sources. Calculations made with the lens plane method of the likelihood of multiple imaging in different types of universe can be compared with observed numbers of multiple images to put constraints on various parameters (Kochanek, 1993).

Since the results depend on the particular matter distribution near the path of the photons, it is usual in this and other methods to adopt a Monte-Carlo approach. This provides not just average values of amplification but also some idea of the spread we should expect.

1.2.2 Direct Integration

The direct integration method uses differential geometry to calculate the effect spacetime curvature has on the histories of neighbouring particles, such as photons. Assuming that the curvature can be calculated at every point along the light path, the size and shape of the light beam at any point can then be calculated by direct integration of the appropriate differential equations.

The geodesic deviation equation may be solved for a collection of neighbouring photons to determine the shape of an image. Alternatively, optical scalars may be defined which describe the shape of a beam of light and evolution equations for these optical scalars solved. The mathematical description of these methods may be found in chapter 4. One of the main results is the focusing equation,

$$\frac{\mathrm{d}^2\sqrt{A}}{\mathrm{d}v^2} = -\left(\sigma^2 + R_{\mu\nu}k^\mu k^\nu\right)\sqrt{A}, \tag{1.15}$$

where

- v is any affine parameter along the null geodesic
- σ is the rate of shear of the light beam
- k^μ is the wavevector, $k^\mu = \mathrm{d}x^\mu/\mathrm{d}v$
- $R_{\mu\nu}$ is the Ricci tensor
- A is the cross sectional area of the light beam.

The focusing equation means that contributions to gravitational lensing are due to the local matter density which manifests through the Ricci tensor and is called

Ricci focusing; and due to the presence of strong tidal fields which cause shear such as are caused by asymmetrical matter distribution near the light beam.

Direct integration was used by Holz and Wald (1998) to study lensing in a perturbed FRW universe which is split into regions. The Newtonian potential is calculated for the matter distribution in each region and the curvature tensor calculated from the potential. The geodesic deviation equation is solved over a path through the resultant space to determine the statistics of the magnification, rotation and shear of images. The matter distribution results from randomly placing point masses in a region. Any particular region is not required to have the same total matter content as the underlying FRW universe although on average [1] equality is required to hold. There is no background matter so there is no Ricci focusing except on the rare occasions when the beam passes through a dense clump of matter. The redshift of the light beam is calculated after the photon has traversed each region according to the underlying FRW model.

Bergström *et al.* (2000) generalised the work of Holz and Wald to allow for non-vanishing pressure and for realistic galaxy profiles. Bergström *et al.* found that lensed beams are of the order of up to 1.0 magnitudes different to unlensed beams. They found that the effect is larger at higher redshifts and that the probability distribution of magnitudes is non-Gaussian.

1.3 Universe models commonly used to study gravitational lensing

The particular framework used to study the propagation of a beam of light only partly describes any method used to study gravitational lensing. Of equal importance is the choice of universe model under consideration and the distribution and type of matter. One choice is to assume a FRW geometry and use N-body simulations to describe the matter content (e.g., Wambsganss *et al.*, 1998). This

[1] There exist several definitions of an "average" for general relativity (Boersma, 1998). Holz and Wald do not specify which average they intend to be used although they appear to mean a simple arithmetic average.

section describes several other methods which pay more attention to incorporating the inhomogeneity into the mathematical description of the geometry. It is by no means exhaustive as there are many cosmological models known and the behaviour of light has been studied in many of them.

1.3.1 Swiss - Cheese Universe

The Swiss-Cheese model of the universe is created by taking a FRW universe and removing the matter from spherical regions. The matter that would have been in the spherical region is compressed into a smaller sphere centred on the same point as the original spherical region. The area of the universe outside the spheres thus become the "cheese" and the empty regions become the holes in the cheese.

The cosmological evolution of the Swiss-Cheese universe is identical to that of the underlying FRW universe. Since the FRW model appears to fit very well with observations, the Swiss-Cheese model is an important one. While it is not a very realistic model in terms of structure formation and various other important features of modern cosmology, it is a simple model to deal with and it incorporates some of the important features for light propagation. Photons spend part of their journey in intergalactic (or interstellar) dust, part of it in voids and part near massive objects.

Kantowski (1969) argued that the Swiss-Cheese model is an appropriate one for looking at light propagation and found that the shear has a negligible effect, as does the gravitational redshift. Therefore $\sigma = 0$ in equation (1.15) and all the focusing is due to the Ricci term which describes the local matter distribution term and is a step function in the Swiss-Cheese model. Kantowski *et al.* (1995) returned to the Swiss-Cheese model and concluded that inhomogeneities can have a large effect on measurements of cosmological parameters using supernova data.

The Dyer-Roeder distance (Dyer and Roeder, 1972) obeys the same formula as the luminosity distance in the Swiss-Cheese model. It is derived by assuming that some of the matter in the universe is gathered in clumps and introducing a

clumpiness parameter α

$$\alpha = \frac{\text{matter not bound in clumps}}{\text{total matter}}. \tag{1.16}$$

Further assuming that light beams pass far from all clumps, the clumps do not directly effect light propagation but there is less matter in the light beam so there is less focusing. The Dyer-Roeder distance can be calculated analytically for some special cases.

1.3.2 Perturbed FRW Universe

The FRW line element can be perturbed by inserting the Newtonian gravitational potential ϕ appropriately to attain the perturbed metric

$$\mathrm{d}s^2 = -\left(1+2\phi\right)c^2\mathrm{d}t^2 + \left(1-2\phi\right)a\left(t\right)^2\left[\frac{\mathrm{d}r^2}{1-kr^2} + r^2\left(\mathrm{d}\theta^2 + \sin^2\theta\mathrm{d}\psi^2\right)\right]. \tag{1.17}$$

Coordinate and conformal transformations are often used to change the appearance of equation (1.17) for convenience. Various conditions are imposed on ϕ to try to ensure that on a large scale the perturbed FRW model looks the same as the FRW model. Generally, ϕ is assumed to be small compared to 1 and have small first spatial derivatives compared to second spatial derivatives.

Linder (1998) and others (see references therein) have looked at models which average to the FRW model in some sense, but not others. For example, models which are the same as FRW in a volume averaged sense but have different dynamics (Tolman-Bondi model) or models which are FRW both in a volume averaged sense and dynamically, but not in a line of sight averaged sense (Dyer-Roeder). These models do not, in general, have the same light propagation behaviour as the FRW model.

1.3.3 Lemaître-Tolman Universe

The Lemaître-Tolman model (Krasiński, 1997) is a spherically symmetric inhomogeneous universe. It is one of the simplest generalisations of the FRW model and as such has been well studied. The matter content is dust arranged in concentric

shells about the centre of symmetry. There are two arbitrary functions that are not present in the FRW model and which may be specified on some space-like hypersurface, the matter density and the time since an initial singularity. Care must be taken to ensure that the shells do not cross to avoid additional singularities.

Since the Lemaître-Tolman universe allows the study of gravitational lensing in the context of general relativity without resorting to Newtonian approximations or assuming that the inhomogeneities do not influence the large scale evolution, it has been a natural choice for investigating distance relationships with inhomogeneities present. In particular, Mustapha *et al.* (1998) have formulated the mathematical description of the Lemaître-Tolman model specifically to simplify calculations on the past null cone of an observer.

1.4 Inhomogeneities and redshift

The effect of matter inhomogeneities on the apparent brightness of distant objects is well studied. On the other hand the influence of matter inhomogeneities on the redshift of distant objects is less well studied, especially without restricting the model to flat spatial sections and a zero cosmological constant. Obviously any effects must be understood in order for the magnitude-redshift relationship to be used in an inhomogeneous universe. Studies which use a full general relativistic treatment to derive a magnitude-redshift relationship in an inhomogeneous universe automatically take into account the effect of the inhomogeneities on the redshift. Examples of this include Moffat and Tatarski (1992), who discuss the redshift-lookback time relationship in a Lemaître-Tolman universe and Sasaki (1987) who investigates the magnitude-redshift relationship in a linearly perturbed FRW universe. Lake (1992) matches plane symmetric vacuum spacetimes to plane symmetric dust spacetimes to form a pancake structure which Lake considers to be a planar counterpart to the Swiss-cheese model, which yields anisotropic redshifts. Mustapha *et al.* (1998) also discuss the area distance-redshift relationship in a Lemaître-Tolman universe that has been matched to an

equivalent FRW universe and find significant differences in the distance-redshift relationship. In contradiction however is the work of Sugiura *et al.* (1999) who consider the same problem but find that the distance-redshift relationship is the same as in a FRW universe provided that a particular matching condition is used.

Mavrides (1976) attempts to model the effect of an observer being in a dense region of space with a higher Hubble constant (H_0) locally than globally. Mavrides considers a three region arrangement with a central dense region centred on the observer, an intermediate vacuum region and an exterior region. The interior dense region and the exterior region are represented as flat FRW regions containing pressureless dust with $\Omega_\Lambda = 0$. The intermediate vacuum region is Schwarzschild and is large enough to ensure that the dense region does not affect the average density. This approach includes the effect of the gravitational redshift. Tomita (2001a,b) also investigates the effect of a local value for H_0 that is higher than the global value but with a local void rather than a local overdensity. Tomita (2001b) successfully shows that the presence of a local void is an alternative to a nonzero cosmological constant for understanding the supernovæ data. However, this result is very sensitive to the additional parameters introduced. Turner *et al.* (1992) investigate numerically in a CDM universe the deviation of local measurements of H_0 from the global value and find that the local value of H_0 may be up to 50% different to the global value on scales up to $20h^{-1}$Mpc.

Nottale (1982) considers the same physical situation as Mavrides (1976) but to a different purpose. Nottale considers an overdense region representing a lensing cluster. The source to be observed is behind the cluster and the observer in front. The light ray passes through the centre of the inhomogeneity. Nottale (1982) is unusual in concentrating on the effect that lensing has on redshift and finds a redshift change of $\delta z \approx 200\text{kms}^{-1}$ from a rich cluster of galaxies.

Kurki-Suonio and Liang (1992) compare the matter distribution in redshift space to the matter distribution in spacetime in a Lemaître-Tolman universe and conclude that "it is fundamentally self-inconsistent to use a Friedmann relation between redshift and comoving distance when dealing with inhomogeneities."

None of these methods is very general and most are not physically realistic. The

models which require a vacuum region of exactly the correct size to balance out an overdensity are not realistic. The Lemaître-Tolman model approaches require a spherically symmetric model with the observer normally at or near the centre of symmetry and also impose conditions on the inhomogeneities to avoid shell crossing singularities. One of the major aims of this thesis is to construct a method of calculating a magnitude-redshift relationship which incorporates the effect of inhomogeneities on the redshift as well as on the magnitude. This is achieved by treating the universe as a collection of independently evolving regions through which a light path travels. The light gets redshifted in each region according to the expansion rate of that region. This approach does not include the gravitational redshift as it is only intended for use over very large distances over which the gravitational redshift is assumed to be negligible compared to the cosmological redshift.

1.5 Outline of thesis

This thesis describes some effects of gravitational lensing on apparent magnitudes and the ramifications for cosmological parameter estimation from apparent magnitudes.

Chapter 2 contains a description of the use of high redshift supernovæ for cosmological parameter estimation and an investigation into the degree to which the results of such experiments are dependent on the supernovæ at intermediate redshifts.

Chapter 3 discusses a paper (Weinberg, 1976) which investigates apparent luminosities in a locally inhomogeneous universe and claims that "as long as the clump radii are sufficiently small, gravitational deflection by the clumps will produce the same average effect as would be produced if the mass were spread out homogeneously". It is shown that this statement is incorrect if the problem is considered in terms of the redshift rather than in terms of coordinate distance as a perturbed FRW universe has a different coordinate distance-redshift relationship than the underlying FRW universe. The original material in chapter 3 has been previously

published (Rose, 2001). This result motivates the remainder of the thesis, which is devoted to developing a new method of calculating the apparent magnitude-redshift relationship in an inhomogeneous universe in which each region of space expands at a rate dependent on the local matter density.

Chapter 4 contains a description of the theory of geodesic deviation, which is required for chapters 5 and 6. Chapter 5 describes a new method used to calculate the non-linear evolution of matter perturbations and the concomitant relationship between the matter density and the local rate of expansion of space, which is also required for chapter 6. The resultant matter distribution is shown to be consistent with a log-normal distribution as proposed by Coles and Jones (1991).

Chapter 6 develops a method of calculating the magnitude-redshift relationship which takes into account not only matter inhomogeneities but also a varying local rate of expansion of space. The universe is treated as a collection of regions of size $8h^{-1}$Mpc with a uniform matter density in each region, expanding (or contracting) at a rate determined by the matter density in the region. The Dyer-Roeder distance is modified to create a second new magnitude-redshift relationship which assumes that light paths that we see are less likely to have travelled through dense matter. The influence that modifying the magnitude-redshift relationship has on cosmological parameter estimation from supernovæ data is also discussed.

Chapter 2

Cosmological parameter extraction using supernovæ

2.1 Introduction

As explained in chapter 1 the relationship between magnitude and redshift can be used to constrain Ω_m and Ω_Λ. This chapter concerns the analysis of Perlmutter *et al.* (1998) and Riess *et al.* (2001) using supernovæ data. Section 2.2 briefly describes the supernovæ data and how it is analysed to determine cosmological parameters. The two different datasets are combined and confidence regions for the cosmological parameters Ω_m and Ω_Λ are shown. Section 2.3 takes a closer look at the data and investigates the possible effect on the results of collecting more data in redshift regions which are currently relatively undersampled. It is found that observing more supernovæ with redshifts $0.1 < z < 0.3$ would probably alter the results of the supernovæ experiments alone. Taken in conjunction with the findings from close analysis of the anisotropies of the CMB, that the universe is very close to flat (Netterfield *et al.*, 2002), observing more supernovæ at comparatively low redshifts is unlikely to alter our current picture of the universe.

2.2 Description of data and analysis

Two independent research teams have published magnitude data of type Ia supernovæ. The High-Z Supernovæ Team (Riess *et al.*, 1998) and the Supernovæ

Cosmology Project (Perlmutter *et al.*, 1998) have published data for 50 and 60 supernovæ respectively. There are 18 supernovæ common to each group. Subsequent to the original publications, analysis of a supernova at $z = 1.7 \pm 0.1$ was published (Riess *et al.*, 2001) to bring the total dataset to 93 supernovæ.

Type Ia supernovæ do not all have the same absolute luminosity but a relationship between the width of the B-band light curve and the absolute luminosity is known (Hamuy *et al.*, 1995) and Riess *et al.* (1996) developed empirically the Multi colour Light Curve Shape (MLCS) method which can also be used to standardise type Ia supernovæ. These methods can reduce the intrinsic dispersion in supernovæ luminosities to 0.20 magnitudes which is good enough to allow the use of supernovæ for cosmological parameter estimation. Both groups publish their data in a corrected form. The Supernovæ Cosmology Project publish what the B-band magnitude would be if the supernova was a standard type Ia supernova and the High-Z Supernovæ Team publish the distance modulus, μ_0, for each supernovæ where $\mu_0 = m - M$, the difference between the observed and absolute magnitudes.

Wang (2000) has analysed the published data for the common supernovæ and found that the absolute magnitude in the B-band of a standard supernova in the combined dataset is

$$M_B = -19.33 \pm 0.25. \tag{2.1}$$

This allows the two datasets to be combined and treated as one. Figure 2.1 shows the combined data set with the High-Z Supernovæ Team data converted to B-band magnitudes.

The theoretical distance modulus with luminosity distance d_L in units of Megaparsecs is

$$\mu_t \equiv m - M = 5\log(d_L) + 25. \tag{2.2}$$

The luminosity distance is (Weinberg, 1972)

$$d_L(z;\Omega_m,\Omega_\Lambda,H_0) = cH_0^{-1}(1+z)|\Omega_k|^{-1/2}\times \\ \operatorname{sinn}\left(|\Omega_k|^{-1/2}\int_0^z \left[(1+z)^2(1+\Omega_m z) - z(2+z)\,\Omega_\Lambda\right]^{-1/2} \mathrm{d}z\right) \tag{2.3}$$

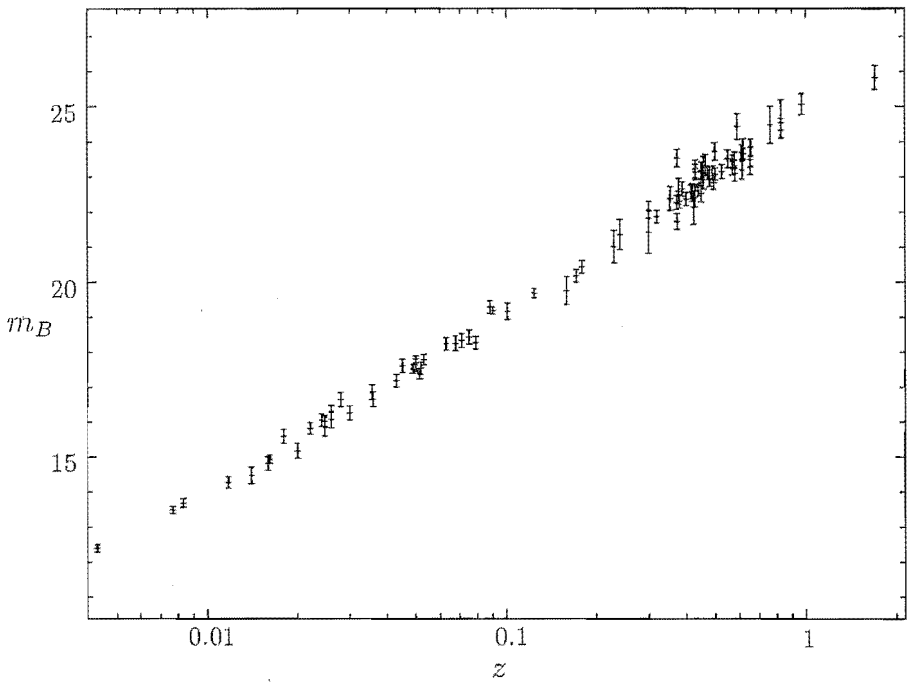

Figure 2.1: Supernova magnitudes

where Ω_k has the standard meaning $\Omega_k = 1 - \Omega_m - \Omega_\Lambda$ and sinn is sinh for $\Omega_k \geq 0$ and sin for $\Omega_k \leq 0$.

Equation (2.2) is conveniently rearranged into the form

$$m_B^{eff} = \mathcal{M} + 5\log(\mathcal{D}_L), \tag{2.4}$$

where $\mathcal{D}_L \equiv H_0 d_L$ is the "Hubble constant free" luminosity distance and $\mathcal{M}$ is a nuisance parameter which must be estimated concomitant with Ω_m and Ω_Λ but which is not needed further. Equation (2.4) may be considered to be a definition of m_B^{eff}, as the parameter $\mathcal{M}$ may absorb any constants required to ensure that (2.4) refers only to the B-band magnitude of a standardised type Ia supernovæ.

To extract the constraints on Ω_m and Ω_Λ implied by the supernovæ data we compare the magnitude expected at the observed redshift in a universe with particular values of Ω_m and Ω_Λ with the observed magnitude. The comparison is performed using χ^2 statistics.

For any set of parameters $\{\Omega_m, \Omega_\Lambda, \mathcal{M}\}$, the magnitude function and the χ^2 goodness of fit statistic may be calculated by performing the following sum over

all data points

$$\chi^2(\Omega_m, \Omega_\Lambda, \mathcal{M}) = \sum_i \frac{\left(m_B^{eff}(z_i; \Omega_m, \Omega_\Lambda, \mathcal{M}) - m_i\right)^2}{\sigma_i^2} \tag{2.5}$$

where the i'th observation is $\{z_i, m_i\}$. The χ^2 statistic is found over a grid of parameter values to find the combination of parameters which best fits the data and is presented in normalised form,

$$\chi^2_\nu = \frac{\chi^2}{\nu} \tag{2.6}$$

where ν is the number of degrees of freedom – the difference between the number of data points and the number of fitted parameters.

Bayesian confidence intervals are constructed as follows. The probability density of parameters $\{\Omega_m, \Omega_\Lambda, \mathcal{M}\}$ given observations $m_B^{eff}(z_i)$ is (Zech, 2002)

$$p(\Omega_m, \Omega_\Lambda, \mathcal{M}|m_B^{eff}) = \frac{p(m_b^{eff}|\Omega_m, \Omega_\Lambda, \mathcal{M})\pi(\Omega_m, \Omega_\Lambda, \mathcal{M})}{\pi(m_b^{eff})} \tag{2.7}$$

where $\pi(\Omega_m, \Omega_\Lambda, \mathcal{M})$ and $\pi(m_b^{eff})$ are the prior densities of the parameters or data respectively. For $\Omega_m \leq 0$, $\pi(\Omega_m, \Omega_\Lambda, \mathcal{M})$ is taken to be zero as a negative matter density is unphysical. FRW universes with a large positive cosmological constant have no initial singularity but collapsed to a finite radius and are now re-expanding (Carroll *et al.*, 1992) and these universes are also rejected. This bouncing universe occurs when

$$\Omega_\Lambda \geq 4\Omega_m \left\{ \text{coss}\left[\frac{1}{3}\,\text{coss}^{-1}\left(\frac{1-\Omega_m}{\Omega_m}\right)\right]\right\}^3, \tag{2.8}$$

where

$$\text{coss} = \begin{cases} \cos & \text{if } \Omega_m \geq 0.5 \\ \cosh & \text{if } \Omega_m \leq 0.5. \end{cases} \tag{2.9}$$

Otherwise the prior densities are taken to be uniform, indicating no preferred parameters.

The Probability Density Function (PDF) is proportional to a Gaussian (Riess *et al.*, 1998)

$$p(\Omega_m, \Omega_\Lambda, \mathcal{M}|m_B^{eff}) \propto \exp(-\frac{\chi^2}{2}) \tag{2.10}$$

and is normalised by integrating over the whole parameter space. The nuisance parameter $\mathcal{M}$ may be integrated out (Zech, 2002) as follows

$$p(\Omega_m, \Omega_\Lambda | m_B^{eff}) = \int_{-\infty}^{\infty} p(\Omega_m, \Omega_\Lambda, \mathcal{M} | m_B^{eff}) \mathrm{d}\mathcal{M}. \tag{2.11}$$

A contour plot in the $\{\Omega_m, \Omega_\Lambda\}$ plane showing 1σ to 4σ confidence regions determined from the supernovæ data is shown in figure 2.2. The best fit parameters are $\{\Omega_m, \Omega_\Lambda\} = \{0.54, 0.9\}$ with a normalised χ^2 value of $\chi^2_\nu = 1.50$. The best fit to a flat universe ($\Omega_m + \Omega_\Lambda = 1$) is $\{\Omega_m, \Omega_\Lambda\} = \{0.36, 0.64\}$ with $\chi^2_\nu = 1.51$. The best fit to a universe with no cosmological constant is $\Omega_m = 0$ with $\chi^2_\nu = 1.56$. As can be seen from figure 2.2, the best fit universe with no cosmological constant is ruled out at a confidence level of 3σ. All three stated best fits find very similar values for $\mathcal{M}$. The values stated for χ^2_ν are higher than the values quoted in Riess *et al.* (1998) and Perlmutter *et al.* (1998) as outliers are not ignored here.

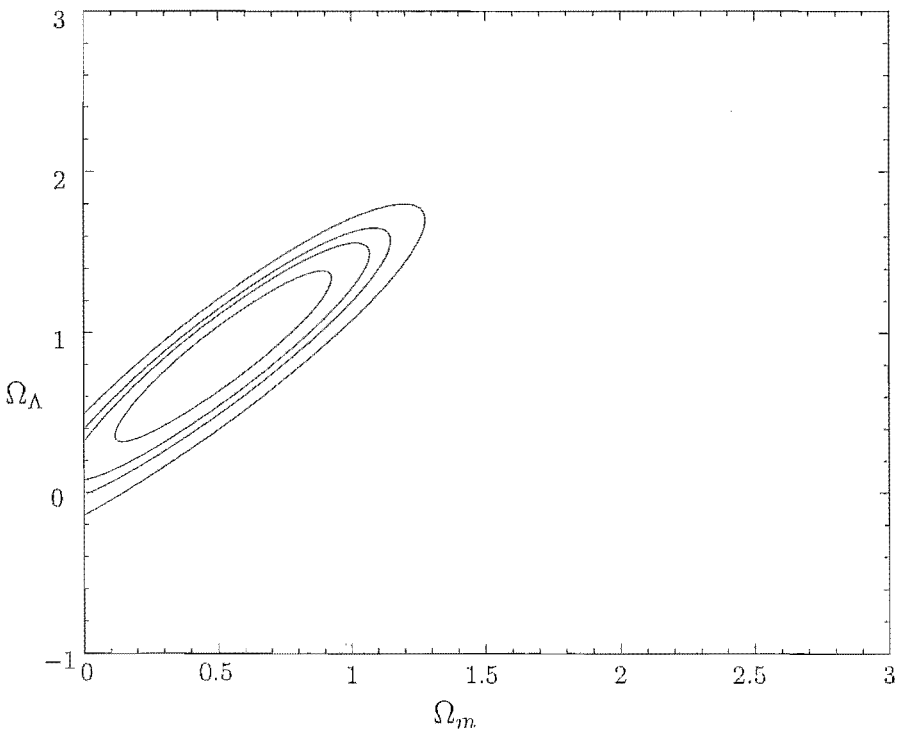

Figure 2.2: Contour plot with $1\sigma - 4\sigma$ confidence regions for all 93 data points

2.3 Dependence of results on intermediate redshift supernovæ

The procedure described in section 2.2 fits data points to a curve with three free parameters. The first parameter, $\mathcal{M}$, sets the vertical position of the curve and is only weakly correlated with the other two parameters, Ω_m and Ω_Λ, which set the shape of the curve. Figure 2.3 illustrates the dependence of the theoretical magnitude-redshift relationship on Ω_m and Ω_Λ. In figure 2.3 the magnitude-redshift relationship is plotted for a large number of combinations of the cosmological parameters within the region $\{0.0 \leq \Omega_m, \Omega_\Lambda \leq 1.0\}$, keeping $\mathcal{M}$ fixed. It can be seen that there is negligible variation at redshifts lower than $z \sim 0.1$ in the magnitude-redshift relationship as Ω_m and Ω_Λ vary. Data points in this region constrain $\mathcal{M}$ but not Ω_m and Ω_Λ. Between $z \sim 0.1$ and $z \sim 0.3$ there is moderate variation. The dependence of the magnitude-redshift relationship on Ω_m and Ω_Λ clearly increases with redshift up to at least $z = 1.7$.

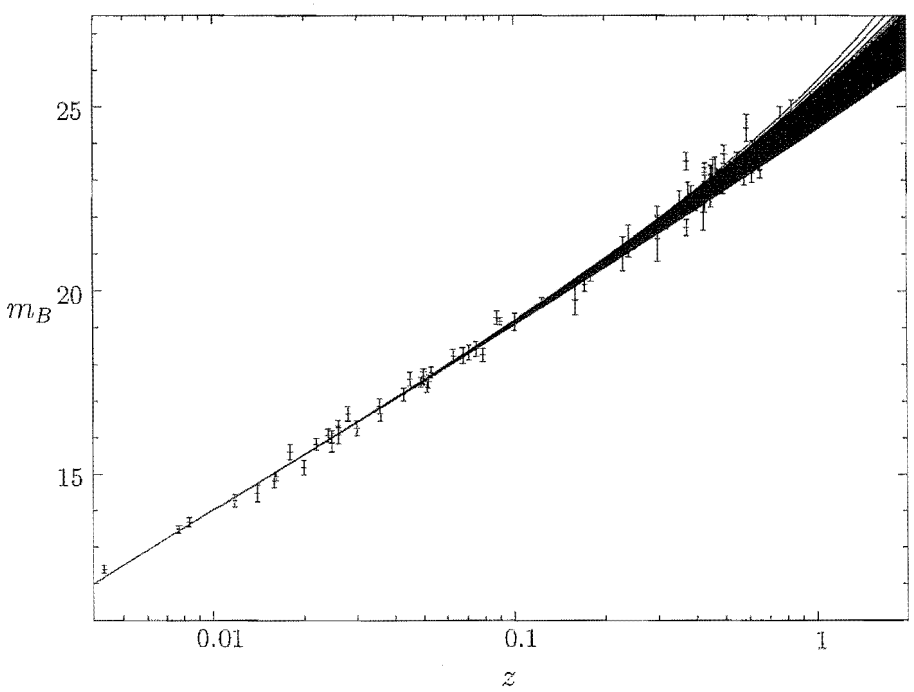

Figure 2.3: Magnitude – redshift plot showing variation in magnitude possible for $\{0.0 \leq \Omega_m \leq 1.0, 0.0 \leq \Omega_\Lambda \leq 1.0\}$. Also plotted are data points

The redshift distribution of supernovæ is not uniform. Table 2.1 shows the number of observed supernovæ in 20 redshift ranges with each range having equal size in $\log(z)$ along with the weighted mean magnitude of supernovæ in that bin and the uncertainty in the mean. The weighted mean magnitudes are weighted according to the uncertainty in the data point (Bevington and Robinson, 1992),

$$\mu = \frac{\sum(m_i/\sigma_i^2)}{\sum(1/\sigma_i^2)} \tag{2.12}$$

and the uncertainty in the weighted mean is

$$\frac{1}{\sigma_\mu^2} = \sum \frac{1}{\sigma_i^2}. \tag{2.13}$$

Figure 2.4 shows the data points after binning, with the bin points plotted 1.5 magnitudes below the raw data points.

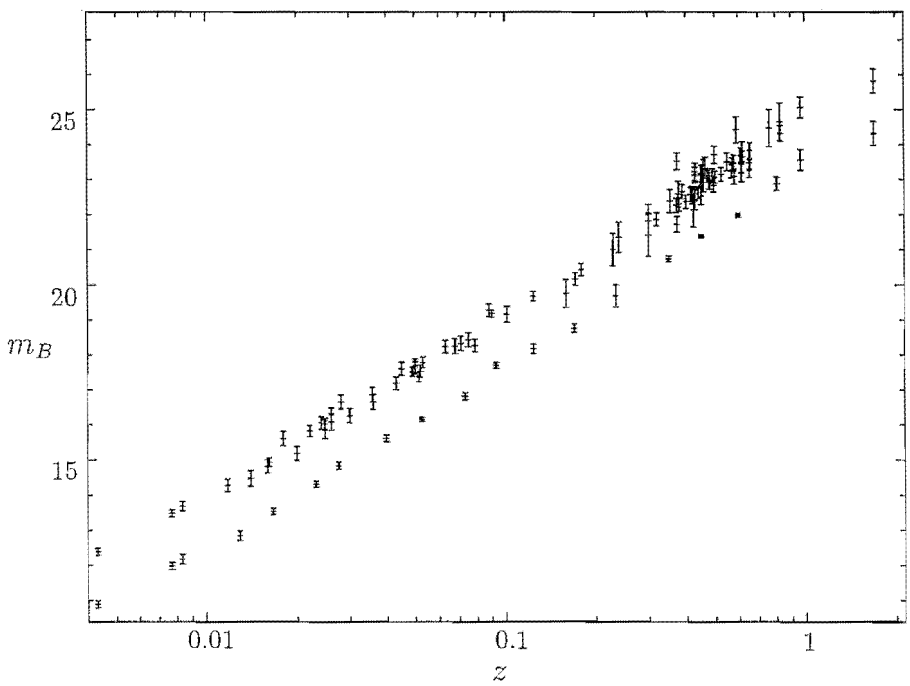

Figure 2.4: Supernova magnitudes. Also shown are binned data points, offset by 1.5 magnitudes

There are 35 supernovæ with redshifts $z \leq 0.115$ and another 47 supernovæ in the three bins covering redshifts $0.283 < z \leq 0.693$. The data in these three higher

Redshift range	No. of SN	Mean redshift	Mean magnitude
0.000 - 0.006	1	0.0043	12.390±0.100
0.006 - 0.008	1	0.0077	13.480±0.100
0.008 - 0.011	1	0.0083	13.680±0.130
0.011 - 0.014	2	0.0129	14.341±0.137
0.014 - 0.019	3	0.0167	15.039±0.091
0.019 - 0.026	5	0.0231	15.814±0.083
0.026 - 0.035	4	0.0275	16.337±0.104
0.035 - 0.047	4	0.0399	17.114±0.098
0.047 - 0.063	7	0.0526	17.658±0.061
0.063 - 0.086	4	0.0732	18.319±0.098
0.086 - 0.115	3	0.0930	19.198±0.082
0.115 - 0.156	1	0.1245	19.680±0.130
0.156 - 0.210	3	0.1707	20.259±0.118
0.210 - 0.283	2	0.2350	21.187±0.314
0.283 - 0.381	9	0.3502	22.239±0.080
0.381 - 0.514	23	0.4500	22.877±0.046
0.514 - 0.693	15	0.5988	23.473±0.058
0.693 - 0.935	3	0.8070	24.380±0.190
0.935 - 1.261	1	0.9700	25.060±0.300
1.261 - 1.700	1	1.7000	26.160±0.340

Table 2.1: Supernovæ bins

redshift bins contribute most of the information we are able to gather about the cosmological parameters from the supernovæ data. The three bins with redshifts covering $0.115 < z \leq 0.283$ are comparatively empty. The uncertainty in these three bins is large compared to bins with more supernovæ and compared to the variation in the magnitude-redshift relationship over the redshift range covered by the bins. This suggests that the constraints on the cosmological parameters could be improved by observing more supernovæ in the redshift range $0.1 < z \leq 0.3$.

The presence of more data points in a bin influences the χ^2 calculation through a smaller uncertainty in the mean for that bin. Gathering more data for any

	Best fit models $(\Omega_m, \Omega_\Lambda)$ and χ^2_ν			
	Reduced uncertainty		Unaltered data	
Overall best fit	(0.32, 0.66)	2.05	(0.55, 0.95)	1.46
Flat universe best fit	(0.34, 0.66)	2.05	(0.35, 0.65)	1.49
$\Lambda = 0$ best fit	(0, 0)	2.30	(0,0)	1.83

Table 2.2: Most likely cosmological parameters and χ^2_ν for binned data and for binned data simulating more supernovæ observations

redshift bin would therefore lower the uncertainty for that bin. Of course, the location of the mean may also change, but we will assume that the data obtained so far is representative and so the mean will shift to another point within the existing 1σ uncertainty for that bin. We can therefore simulate the effect on the analysis of gathering more data in any redshift range by reducing the size of σ_μ for that bin.

2.3.1 Simulating additional supernovæ at intermediate redshift

The bin containing the highest number of supernovæ has 23 supernovæ and an uncertainty on the mean magnitude of ± 0.046 magnitudes. Reducing the size of the uncertainties in the mean in the three bins with redshifts covering $0.115 < z \leq 0.283$ to 0.046 magnitudes simulates the effect of gathering a similar quantity of data in these bins.

Figure 2.5 shows the effect of reducing the uncertainties in the three bins covering $0.115 < z \leq 0.283$ to 0.046 magnitudes. The solid lines show confidence regions calculated after reducing the uncertainties of three bins. They should be compared with the dashed lines which show confidence regions calculated using bins as tabulated in table 2.1. The shape of the confidence regions is very similar but regions calculated with smaller uncertainties are shifted significantly toward the origin. Table 2.2 shows the most likely cosmological parameters and normalised χ^2 for the binned data and for the binned data after reducing the uncertainties in three bins. The most likely flat universe is only slightly different to the results calculated from the unaltered data bins and the most likely universe with no

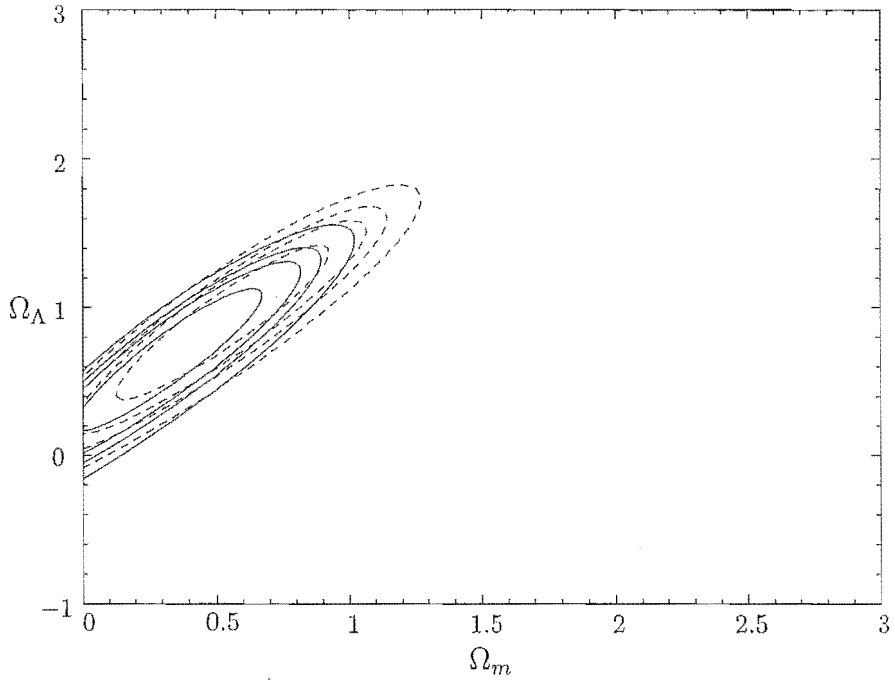

Figure 2.5: Contour plot with $1\sigma - 4\sigma$ confidence regions showing the effect of reducing the uncertainties in three bins. The dashed lines show confidence regions calculated using bins as plotted in figure 2.4. The solid lines show confidence regions calculated after reducing the uncertainties of three bins

cosmological constant is unchanged. As should be expected after reducing the size of some of the uncertainties, the normalised χ^2 value has increased.

2.3.2 Lowering the mean magnitude of supernovæ at intermediate redshifts

Figure 2.6 shows the effect of lowering the mean magnitudes of the three bins covering $0.115 < z \leq 0.283$. The dotted dashed lines are confidence regions calculated after reducing the uncertainties in the three bins and are identical to the solid lines in figure 2.5. The solid lines show confidence regions calculated after also lowering the mean magnitudes in those bins by 0.046 magnitudes. These confidence regions are shifted further toward the origin, with a universe with zero cosmological constant being ruled out at only a 2σ level. The dashed lines show confidence regions calculated after also lowering the mean magnitudes in those

	Best fit models $(\Omega_m, \Omega_\Lambda)$ and χ^2_ν					
	Slightly lowered		Significantly lowered		Unaltered data	
Best fit	(0.18, 0.48)	2.43	(0.0, 0.18)	4.85	(0.55, 0.95)	1.46
Flat universe	(0.32, 0.68)	2.44	(0.32, 0.68)	5.16	(0.35, 0.65)	1.49
$\Lambda = 0$	(0.0, 0.0)	2.62	(0.0, 0.0)	4.94	(0.0, 0.0)	1.83

Table 2.3: Most likely cosmological parameters and χ^2_ν for binned data and for binned data simulating more supernovæ observations which lower the mean magnitude

bins by by the size of the one σ uncertainty in the mean in each of the bins, which is by 0.13, 0.118 and 0.314 magnitudes, in order of increasing z. These confidence regions are shifted still further toward the origin and a zero cosmological constant universe cannot be ruled out with any degree of confidence. Table 2.3 shows the most likely cosmological parameters and normalised χ^2 for the binned data and for the binned data after reducing the uncertainties in three bins and lowering the mean magnitude of those bins. The most likely flat universe is again only slightly different to the results calculated from the unaltered data bins and the most likely universe with no cosmological constant is unchanged. The scenario in which the mean of the three bins is reduced significantly and which does not rule out a universe with no cosmological constant has very high values of χ^2_ν. This simulated data is very unlikely to occur in an FRW universe.

2.3.3 Raising the mean magnitude of supernovæ at intermediate redshifts

Figure 2.7 and table 2.4 show the effect of raising the mean magnitudes of the three bins covering $0.115 < z \leq 0.283$. The opposite effect has taken place to that in figure 2.6, with the confidence regions shifted away from the origin. Indeed, when the mean magnitude is raised by the uncertainty in each bin, a flat universe is rejected at a confidence level of 4σ.

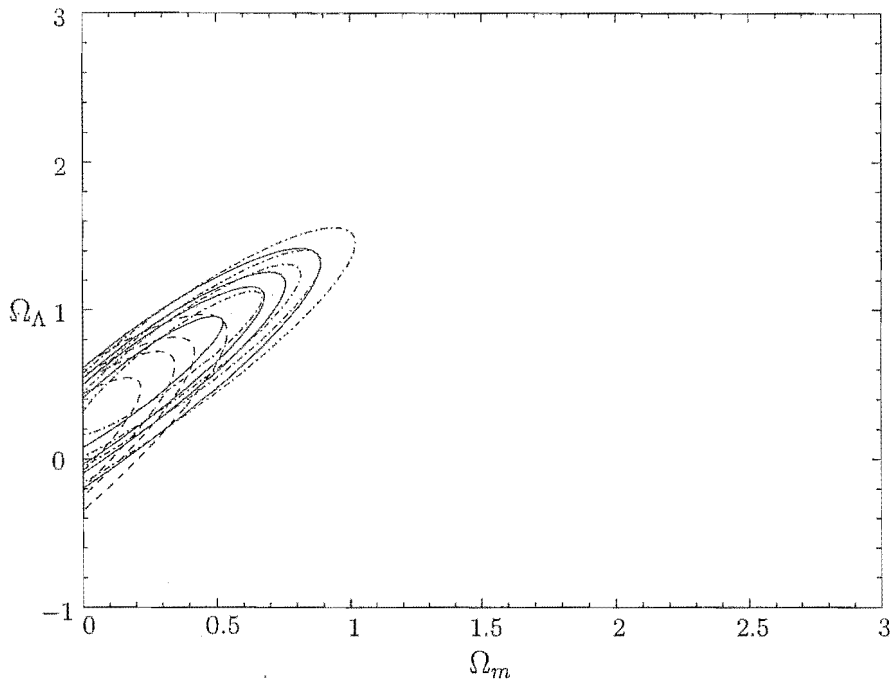

Figure 2.6: Contour plot with $1\sigma - 4\sigma$ sigma confidence regions showing the effect of reducing the uncertainties in three bins and lowering the mean in those bins. The dotted dashed lines show confidence regions calculated after reducing the uncertainties in the three bins, as in figure 2.5. The solid lines show confidence regions calculated after reducing the uncertainties of three bins and lowering the mean of those bins by 0.05 magnitudes. The dashed lines show confidence regions calculated after reducing the uncertainties of three bins and lowering the mean of those bins by σ_μ

2.3.4 Summary

Since a higher value for Ω_Λ tends to increase the luminosity distance of high redshift objects, it is not surprising that lowering the mean magnitudes of three bins makes a lower value of Ω_Λ more likely. What is surprising is the degree of the effect. Shifting three out of twenty data points within their original 1σ uncertainties changes a 4σ result into a null result. However, it should be noted that slightly changing the low redshift data points does not make the $\{\Omega_m, \Omega_\Lambda\} = \{1.0, 0.0\}$ universe any more likely, or significantly change the most likely value for Ω_Λ for a flat universe.

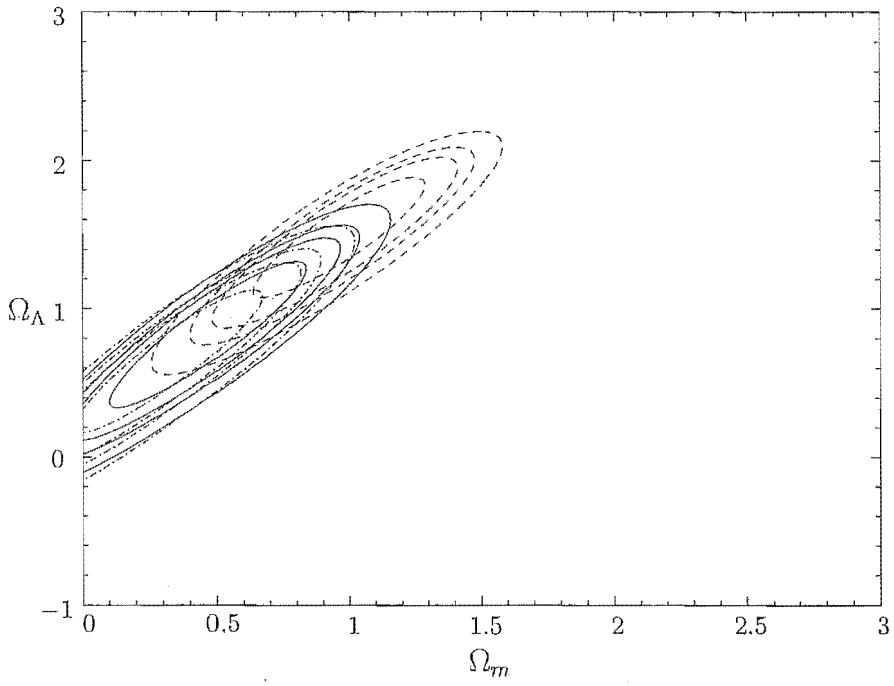

Figure 2.7: As for Figure 2.6 but with the mean raised rather than lowered

	Best fit models $(\Omega_m, \Omega_\Lambda)$ and χ^2_ν					
	Slightly raised		Significantly raised		Unaltered data	
Best fit	(0.48, 0.84)	1.84	(0.98, 1.50)	3.43	(0.55, 0.95)	1.46
Flat universe	(0.34, 0.66)	1.86	(0.34, 0.66)	3.89	(0.35, 0.65)	1.49
$\Lambda = 0$	(0.0, 0.0)	2.20	(0.0, 0.0)	4.61	(0.0, 0.0)	1.83

Table 2.4: Most likely cosmological parameters and χ^2_ν for binned data and for binned data simulating more supernovæ observations which raise the mean magnitude

2.4 Conclusions

The Supernova Cosmology Project (Perlmutter *et al.*, 1998) and the High-Z Supernovæ Team (Riess *et al.*, 1998) have analysed magnitude-redshift data of a set of supernovæ at high redshift. Each group found that to a high degree of confidence the cosmological constant is non-zero and that if the universe is flat the most likely values for the cosmological parameters are close to $\{\Omega_m, \Omega_\Lambda\} = \{0.3, 0.7\}$.

Considered in isolation, further measurements of supernovæ at redshifts between $z =\sim 0.1$ and $z \sim 0.3$ may affect the conclusions drawn from such observations.

When considered in conjunction with the CMB result which indicates a flat universe (Netterfield *et al.*, 2002), further supernovæ observations at low redshifts will not deliver further insights.

Chapter 3

Flux Conservation

3.1 Introduction

Implicit in the analysis performed in the previous chapter is the assumption that the relationship between the apparent magnitude of a distant object and the redshift of that object is unaffected by gravitational lensing.

Weinberg (1976) presents an argument that gravitational lensing does not, on average, affect the apparent magnitude - radial Robertson Walker coordinate relationship. His argument is based on photon number conservation and has been widely accepted, although it has come under some scrutiny. Wu (1990) point out that photon number conservation applies to the luminosity distance, not the apparent magnitude and that a mean deviation of zero in the luminosity distance does not imply a mean deviation of zero in the apparent magnitude, which was also emphasised by Holz and Wald (1998). Ellis *et al.* (1998) reanalyse Weinberg's argument and conclude that it is not valid if caustics are present, which only occurs with strong fields. Mustapha *et al.* (1998) consider spherically symmetric dust shell universes and find that a deviation from the FRW result is possible. Claudel (2000) considers Newtonian perturbations in the weak field limit and finds that, to first order in $\kappa = 8\pi G/c^2$, there is no deviation from the FRW result.

Weinberg's original argument is presented in section 3.2. In section 3.3 we demonstrate using metric perturbations that the presence of inhomogeneities in the

universe does, on average, affect the apparent magnitude - redshift relationship. The material here has been previously published as Rose (2001).

3.2 Photon number count versus coordinate distance

Consider an exact FRW universe containing a source at (comoving coordinate) $r = 0$ that emits N photons isotropically (due to, say, a cataclysmic event). A sphere drawn around the source with $r = r_{\rm obs}$ has surface area $4\pi a_{\rm obs}^2 r_{\rm obs}^2$, where $a(t)$ is the cosmological scale factor. Photon number must be conserved so the same number of photons passes through the sphere as are emitted by the source so an astronomer at $r = r_{\rm obs}$ with a telescope of area A will observe n photons satisfying

$$\frac{4\pi a_{\rm obs}^2 r_{\rm obs}^2}{A} = \frac{N}{n}. \tag{3.1}$$

Now consider the above situation with the matter inside the sphere distributed unevenly, thus lensing the photons. The number of photons observed by the astronomer may be different when compared to the previous situation. However, the total number of photons passing through the sphere is unchanged. If the area of the sphere at $r = r_{\rm obs}$ has not changed then any increase or decrease in photons seen by the astronomer must be compensated by a decrease or increase respectively in the number of photons observed by other astronomers. Furthermore, if there are a large number of astronomers at different points on the sphere at $r = r_{\rm obs}$ then the average number of photons they observe must be distributed about n with a standard deviation that approaches 0 as their combined telescopes cover the sphere. Conversely, a single astronomer who observes a large number of similar events in different directions should expect to observe, on average, n photons from each event.

Weinberg's argument is based on the assumption that the area of the sphere centred on $r = 0$ and with radius $r = r_{\rm obs}$ is not affected by the mass distribution. The area of the sphere is a dynamic quantity that depends not only on r but also on $a(t)$. If inhomogeneities affect the time photons take to travel from $r = 0$ to $r = r_{\rm obs}$ then inhomogeneities must also affect the area of the sphere. If this is

the case then photon conservation does not imply that the observed apparent magnitude relationship is identical to the FRW apparent magnitude relationship. In section 3.3 this is shown to be the case.

3.3 Apparent magnitude versus redshift

Consider a perturbed FRW dust universe with line element

$$\mathrm{d}s^2 = -c^2\mathrm{d}t^2 + a(t)^2(1-h(r,t))^2\left(\frac{\mathrm{d}r^2}{1-kr^2} + r^2\mathrm{d}\theta^2 + r^2\sin^2\theta\mathrm{d}\phi^2\right) \tag{3.2}$$

and an energy momentum tensor

$$T = \begin{bmatrix} \rho_b(t)(1+\delta(r,t)) & 0 & 0 & 0 \\ 0 & 0 & 0 & 0 \\ 0 & 0 & 0 & 0 \\ 0 & 0 & 0 & 0 \end{bmatrix}. \tag{3.3}$$

The quantities $\delta(r,t)$ and $h(r,t)$ describe the departure from homogeneity and $a(t)$ and $\rho_b(t)$ are the scale factor and density in a corresponding unperturbed FRW universe. The coordinates are comoving and peculiar motions are neglected so T contains no terms dependent on the velocity of matter. Equations (3.2) and (3.3) describe a universe that has the same geometry as a FRW universe with scale factor $a(t)$ and density $\rho_b(t)$, but which has concentric shells which may be over or under dense.

The metric has determinant

$$\sqrt{-g} = \frac{ca^3(1-h)^3r^2\sin\theta}{\sqrt{1-kr^2}}. \tag{3.4}$$

Spherical symmetry has been retained so that any astronomer at $r = r_{\mathrm{obs}}$ makes the same observations of a source at $r = 0$ (as in section 3.2) as any other astronomer at $r = r_{\mathrm{obs}}$. Spherical symmetry is an unnatural condition to impose upon inhomogeneities but allowing spherically symmetric inhomogeneities is one of the simplest generalisations of the exact FRW model.

Conditions are imposed upon the perturbed universe to ensure that it does not depart far from the underlying FRW universe. The inhomogeneities are small in both amplitude ($|\delta| \ll 1$ everywhere) and length. The length requirement is satisfied by requiring that in every region small enough that the scale factor, $a(t)$, changes little in the time taken for the photon to travel through it, δ averages to 0. Thus we impose the condition

$$\int_\lambda \frac{\delta(r(\lambda), t(\lambda))}{a(t(\lambda))} \mathrm{d}\lambda = 0 \tag{3.5}$$

where λ is any parameterisation along the geodesic. Finally, $h(r,t) = 0$ at both the source and the observer's locations since the only effect under consideration here is due to matter inhomogeneities between the source and the observer.

In the inhomogeneous case, equation (3.1) is no longer valid as the surface area of the sphere centred on the source at $r = 0$ and with radius r_{obs} is now $4\pi a_{\mathrm{obs}}^2 r_{\mathrm{obs}}^2 (1 - h(r_{\mathrm{obs}}, t_{\mathrm{obs}}))^2$. Due to the assumption that $h = 0$ at both the source and observer the correct expression reduces to equation (3.1).

To determine the relationship between h and δ we use the stress energy conservation law. Following Peebles (1993, page 276) (but note the different definition of h which allows the calculation to be carried out to all orders), the stress energy conservation law leads to

$$\frac{1}{\sqrt{-g}} \partial_\mu (\sqrt{-g} T^\mu{}_0) = \frac{1}{2} g_{\mu\nu,0} T^{\mu\nu} = 0 \tag{3.6}$$

or

$$\frac{\dot{\rho}_b}{\rho_b} + \frac{\dot{\delta}}{1+\delta} = -\frac{3\dot{a}}{a} + \frac{3\dot{h}}{1-h}. \tag{3.7}$$

Since $\dot{\rho}_b/\rho_b = -3\dot{a}/a$ in the unperturbed universe,

$$\frac{\dot{\delta}}{1+\delta} = \frac{3\dot{h}}{1-h} \tag{3.8}$$

which has solution

$$1 - h = (1+\delta)^{-\frac{1}{3}}. \tag{3.9}$$

The integration constant has been determined by requiring that when $\delta = 0$, $h = 0$.

By integrating along a radial null geodesic from emission at $(t, r) = (t_{\rm em}, 0)$ to observation at $(t, r) = (t_{\rm obs}, r)$, the radial coordinate where a photon arrives at the observer in the perturbed universe can be determined and compared to the radial coordinate of the observer in the FRW universe. The null geodesic is parameterised by the affine parameter λ so that the position of the photon is $(t(\lambda), r(\lambda))$. For the radial geodesic, r and t are both monotonically increasing functions of λ and we may reparameterise the geodesic in terms of t; that is, we may define a function $r(t)$ so that $(t, r(t))$ is the position of the photon at time t. Similarly, $h(t)$ and $\delta(t)$ are defined to be the values of h and δ at the photon's position at time t.

A null geodesic in the perturbed FRW universe satisfies

$$\mathrm{d}s^2 = 0 \Rightarrow c\mathrm{d}t = a(t)(1 - h(r,t))\frac{\mathrm{d}r}{\sqrt{1-kr^2}}. \tag{3.10}$$

Rearranging equation (3.10) and integrating, one obtains

$$\int_{t_{\rm em}}^{t_{\rm obs}} \frac{c\mathrm{d}t}{a(t)(1-h(t))} = \int_0^{r_{\rm obs}} \frac{\mathrm{d}r}{\sqrt{1-kr^2}}, \tag{3.11}$$

Similarly, in the FRW universe

$$\int_{t_{\rm em}}^{t_{\rm obs}} \frac{c\mathrm{d}t}{a(t)} = \int_0^{r_{\rm FRW}} \frac{\mathrm{d}r}{\sqrt{1-kr^2}}. \tag{3.12}$$

Substituting for $1 - h$ from equation (3.9) and making the second order approximation $(1+\delta)^{1/3} \approx 1 + \delta/3 - \delta^2/9$, equation (3.11) becomes

$$\int_{t_{\rm em}}^{t_{\rm obs}} \frac{c\mathrm{d}t}{a(t)} + \frac{1}{3}\int_{t_{\rm em}}^{t_{\rm obs}} \frac{c\delta(t)\mathrm{d}t}{a(t)} - \frac{1}{9}\int_{t_{\rm em}}^{t_{\rm obs}} \frac{c\delta(t)^2\mathrm{d}t}{a(t)} = \int_0^{r_{\rm obs}} \frac{\mathrm{d}r}{\sqrt{1-kr^2}}. \tag{3.13}$$

Equations (3.12) and (3.13) are both written using comoving coordinates and proper time and so may be compared directly. The first term in equation (3.13) may be replaced using equation (3.12) and the second term is 0 due to equation (3.5) leaving

$$\frac{1}{9}\int_{t_{\rm em}}^{t_{\rm obs}} \frac{c\delta(t)^2\mathrm{d}t}{a(t)} = \int_{r_{\rm obs}}^{r_{\rm FRW}} \frac{\mathrm{d}r}{\sqrt{1-kr^2}}. \tag{3.14}$$

Since $\delta^2 \geq 0$ and $a > 0$ then $r_{\rm FRW} \geq r_{\rm obs}$ and $r_{\rm obs} = r_{\rm FRW}$ only if $\delta = 0$ at all points along the lightcone. Both under and over densities contribute positively to the integral on the left hand side of equation (3.14). We may use this to compare the observed number of photons in the perturbed universe and the FRW universe. From equation (3.1),

$$\frac{n_{\rm obs}}{n_{\rm FRW}} = \frac{NA}{4\pi r_{\rm obs}^2 a(t_{\rm obs})^2} \frac{4\pi r_{\rm FRW}^2 a(t_{\rm obs})^2}{NA} \tag{3.15}$$

$$= \frac{r_{\rm FRW}^2}{r_{\rm obs}^2} \geq 1. \tag{3.16}$$

For a given redshift, apparent magnitudes in a perturbed universe are greater than those in an unperturbed one. Gravitational lensing can cause magnification for all observers without violating conservation of photon number.

3.4 Discussion

The calculation in section 3.3 is very general in that it does not depend upon the distribution of matter beyond the requirement of spherically symmetric matter perturbations about the source. Furthermore, because the argument is based on the non-linearity of the relationship between matter and the metric it is easy to see how it may applied in more complicated models. However, it does rely on one critical assumption – that the presence of inhomogeneities does not influence the evolution of the universe.

Due to the assumptions made and the special position of the source, the result obtained in section 3.3 need not apply to any particular observation in the real universe. Indeed, the probability that the condition of equation (3.5) is correct for any particular observation is negligible. If, on balance, a light beam passes through more over or under dense space than average the first order term in equation (3.13) will contribute and the source may appear brighter or dimmer than in the FRW case.

The focusing theorem (Schneider *et al.*, 1992, page 132) shows that a light beam is magnified if it is affected by gravitational lensing but does not go through a

caustic. In light of the focusing theorem the result in section 3.3 is not surprising; however it appears to be in contradiction with the results of Mustapha *et al.* (1998). Mustapha *et al.* (1998) investigate Lemaître-Tolman symmetric dust universes and find that distant objects may appear brighter or dimmer than they would in the corresponding FRW model depending on the distance and on the specific matter distribution. They find the corresponding FRW universe by matching the mass and scale of the LTB universe to FRW limit but make no assumptions about the evolution of the LTB universe. Indeed, Buchert (2000) shows that an inhomogeneous universe is exceedingly unlikely to have the same dynamics as a FRW universe of the same density.

Zotov and Stoeger (1992) discuss averaging Einstein's equations for Schwarzschild regions, representing galaxies, on an expanding background. They found that the scale factor for the averaged universe is $S(t)^2 = R(t)^2(1 - K)$, where $R(t)$ is the scale factor for the expanding background. Since K is nonzero and positive $S(t) < R(t)$. This decrease in the scale factor for the inhomogeneous case has the same effect on the observed magnitude of distant objects as does the inequality (3.16). However, the result is not in terms of the redshift so says nothing about the distance-redshift relationship.

The calculation in section 3.3 is based on the assumption that the perturbed universe has exactly the same global evolution as the underlying FRW universe, an assumption that may not be correct. The conclusion of section 3.3 is that universes with small, localised departures from homogeneity which do not affect the dynamics of the universe do not have the same distance-redshift as the corresponding exact FRW universe. That is, we cannot expect the real, inhomogeneous universe to both evolve like an exact FRW universe and to have the same light propagation behaviour as the same exact FRW universe.

Chapter 4

Geodesic Deviation

The theory of geodesic deviation describes how the relative separation of nearby geodesics varies due to gravitational effects. It is shown that the behaviour of a congruence of geodesics can be characterised by its rate of expansion (θ), shear (σ) and rotation (ω) and evolution equations are found for these quantities. These equations will be used in chapter 5 to find the matter distribution in the weakly non-linear regime and in chapter 6 to describe the magnitude-redshift relationship. The results presented here may also be found, for example, in Hawking and Ellis (1973), Peebles (1993) and Wald (1984).

In section 4.1 a congruence is defined and some standard results derived. In particular it is shown that the evolution of a connection vector between neighbouring geodesics can be described as a linear map and hence as an expansion, shear and rotation. In section 4.2 evolution equations for θ, σ and ω are found for timelike curves. In section 4.2.1 these evolution equations are applied to the worldlines of the particles of a pressureless dust. It is shown that for this example θ is the expansion rate of a local patch of space and a pair of differential equations may be formed to describe the expansion rate and matter density of a local patch of space without requiring large scale homogeneity. Finally, in section 4.3 evolution equations for θ, σ and ω are derived for null curves and in section 4.3.1 these results are used to find a differential equation for the cross-sectional area of a beam of light as it travels through an inhomogeneous universe.

4.1 Mathematical Preliminaries

Consider a three parameter family of geodesics $x^\mu = \gamma^\mu_w(y^i)$, where y^i parameterises the family so that specifying y^i specifies a particular geodesic and w is the parameter along each geodesic. $\gamma^\mu_w(y^i)$ forms a congruence, that is, locally exactly one geodesic passes through each point of space-time. The vector field

$$v^\mu = \frac{\mathrm{d}\gamma^\mu}{\mathrm{d}w} = \frac{\mathrm{d}x^\mu}{\mathrm{d}w} \tag{4.1}$$

is tangent to the family of geodesics and so satisfies

$$\frac{\mathrm{D}v^\mu}{\mathrm{d}w} \equiv \frac{\mathrm{d}v^\mu}{\mathrm{d}x^\nu}v^\nu + \Gamma^\mu{}_{\nu\lambda}v^\nu v^\lambda = 0. \tag{4.2}$$

The vector

$$\xi^\mu = \frac{\mathrm{d}\gamma^\mu}{\mathrm{d}y^i}\delta y^i = \frac{\mathrm{d}x^\mu}{\mathrm{d}y^i}\delta y^i \tag{4.3}$$

connects the geodesics $\gamma(y^i)$ and $\gamma(y^i + \delta y^i)$ and is called the connection vector. It is the behaviour of ξ that will be used to investigate the behaviour of the congruence of geodesics.

To begin with, we show that $\xi^\mu v^\nu_{;\mu} = v^\mu \xi^\nu_{;\mu}$ as follows,

$$\begin{aligned}
\xi^\mu \frac{\mathrm{D}v^\nu}{\mathrm{d}x^\mu} =& \xi^\mu \frac{\mathrm{d}v^\nu}{\mathrm{d}x^\mu} + \Gamma^\nu{}_{\mu\lambda}v^\lambda \xi^\mu \\
=& \frac{\mathrm{d}x^\mu}{\mathrm{d}y^i}\frac{\mathrm{d}v^\nu}{\mathrm{d}x^\mu}\delta y^i + \Gamma^\nu{}_{\mu\lambda}v^\lambda \xi^\mu \\
=& \frac{\mathrm{d}v^\nu}{\mathrm{d}y^i}\delta y^i + \Gamma^\nu{}_{\mu\lambda}v^\lambda \xi^\mu \\
=& \frac{\mathrm{d}^2 x^\nu}{\mathrm{d}w\partial y^i}\delta y^i + \Gamma^\nu{}_{\mu\lambda}v^\lambda \xi^\mu \\
=& \frac{\mathrm{d}\xi^\nu}{\mathrm{d}w} + \Gamma^\nu{}_{\mu\lambda}v^\lambda \xi^\mu \\
\xi^\mu \frac{\mathrm{D}v^\nu}{\mathrm{d}x^\mu} =& v^\mu \frac{\mathrm{D}\xi^\nu}{\mathrm{d}x^\mu}.
\end{aligned} \tag{4.4}$$

The significance of (4.4) may be understood by considering $\frac{\mathrm{D}\xi^\mu}{\mathrm{d}w}$. We have

$$\frac{\mathrm{D}\xi^\mu}{\mathrm{d}w} = v^\nu \xi^\mu{}_{;\nu} = v^\mu{}_{;\nu}\xi^\nu = A^\mu{}_\nu \xi^\nu \tag{4.5}$$

where we have made the definition $A_{\mu\nu} = u_{\mu;\nu}$. Thus we see that the connection vector ξ^μ is not parallely transported and $A^\mu{}_\nu$ is a linear map that describes how the displacement between neighbouring geodesics is stretched and rotated.

One further property of ξ^μ is important before going on to investigate $A^\mu{}_\nu$, namely the relationship

$$\frac{\mathrm{D}\left(\xi^\mu v_\mu\right)}{\mathrm{d}w} = \left(\xi^\mu v_\mu\right)_{;\nu} v^\nu = \xi^\mu{}_{;\nu} v_\mu v^\nu = \xi^\nu v^\mu{}_{;\nu} v_\mu = \frac{1}{2}\xi^\nu \left(v^\mu v_\mu\right)_{;\nu} = 0. \qquad (4.6)$$

The second equality is due to v_μ being geodesic and therefore satisfying $v_{\mu;\nu}v^\nu = 0$ and the third is due to (4.4). Since $\xi^\mu v_\mu$ is constant along a geodesic, the behaviour of the part of ξ^μ that is not orthogonal to v^μ is physically uninteresting so all interesting results may be obtained by only considering ξ^μ such that $\xi^\mu v_\mu = 0$.

Everything up to this point has been independent of the nature of v_μ, but it is now necessary to distinguish between timelike and lightlike curves. When timelike curves are under consideration u_μ will be used in place of v_μ and tensors in equations applying to timelike curves are "tilded" ($\widetilde{h}_{\mu\nu}$ etc). Similarly, when lightlike curves are under consideration k_μ will be used in place of v_μ and tensors in equations applying to lightlike curves are "hatted" ($\widehat{h}_{\mu\nu}$ etc). Timelike curves are considered first.

4.2 Timelike Curves

The linear map $A_{\mu\nu}$ may be decomposed into quantities which represent the rates of expansion, shear and rotation and which characterise the behaviour of the congruence. In this section the evolution equations for the rates of shear, expansion and rotation are derived and applied to a specific example in the synchronous gauge. This allows the derivation of evolution equations for the local matter density and the local expansion rate of space.

The projection tensor $\widetilde{h}^\mu{}_\nu = g^\mu{}_\nu + u^\mu u_\nu$ projects into the space orthogonal to u_μ. Recalling that (4.6) means that all quantities of interest are orthogonal to u_μ, $\widetilde{h}^\mu{}_\nu$ projects into the subspace of interest to us. The projection tensor satisfies

the expected properties of a projection operator, that is

$$\widetilde{h}^{\mu}{}_{\nu}v^{\nu}=0, \qquad \widetilde{h}^{\mu}{}_{\lambda}\widetilde{h}^{\lambda}{}_{\nu}=\widetilde{h}^{\mu}{}_{\nu}, \qquad \mathrm{Tr}(\widetilde{h})\equiv\widetilde{h}^{\mu}{}_{\mu}=3. \tag{4.7}$$

The rates of expansion, shear and rotation of the congruence are defined to be

$$\begin{aligned}\widetilde{\theta} =&\widetilde{A}^{\mu\nu}\widetilde{h}_{\mu\nu},\\ \widetilde{\sigma}_{\mu\nu} =&\widetilde{A}_{(\mu\nu)}-\frac{1}{3}\widetilde{\theta}\widetilde{h}_{\mu\nu},\\ \widetilde{\omega}_{\mu\nu} =&\widetilde{A}_{[\mu\nu]}\end{aligned} \tag{4.8}$$

so that $\widetilde{A}_{\mu\nu}$ is decomposed as

$$\widetilde{A}_{\mu\nu}=\frac{1}{3}\widetilde{\theta}\widetilde{h}_{\mu\nu}+\widetilde{\sigma}_{\mu\nu}+\widetilde{\omega}_{\mu\nu}. \tag{4.9}$$

The tensors defined in equations (4.8) can be characterised by the scalars

$$\begin{aligned}\widetilde{\sigma}^2 =&\frac{1}{2}\widetilde{\sigma}_{\mu\nu}\widetilde{\sigma}^{\mu\nu},\\ \widetilde{\omega}^2 =&\frac{1}{2}\widetilde{\omega}_{\mu\nu}\widetilde{\omega}^{\mu\nu}.\end{aligned} \tag{4.10}$$

The rates of change of $\widetilde{\theta}$, $\widetilde{\sigma}_{\mu\nu}$ and $\widetilde{\omega}_{\mu\nu}$ along the geodesic can be calculated as follows:

$$\begin{aligned}\frac{\mathrm{D}\widetilde{A}_{\mu\nu}}{\mathrm{d}w}=\frac{\mathrm{d}x^{\lambda}}{\mathrm{d}w}\frac{\mathrm{D}\widetilde{A}_{\mu\nu}}{\mathrm{d}x^{\lambda}}=u^{\lambda}\widetilde{A}_{\mu\nu;\lambda} =&u^{\lambda}u_{\mu;\nu\lambda}\\ =&u^{\lambda}u_{\mu;\lambda\nu}+R^{\pi}{}_{\nu\mu\lambda}u_{\pi}u^{\lambda}\\ =&(u_{\mu;\lambda}u^{\lambda})_{;\nu}-u^{\lambda}{}_{;\nu}u_{\mu;\lambda}+R^{\pi}{}_{\nu\mu\lambda}u_{\pi}u^{\lambda}\\ =&-\widetilde{A}^{\lambda}{}_{\nu}\widetilde{A}_{\mu\lambda}+R^{\pi}{}_{\nu\mu\lambda}u_{\pi}u^{\lambda}.\end{aligned} \tag{4.11}$$

Taking the trace of (4.11) gives the equation

$$\begin{aligned}\frac{\mathrm{d}\widetilde{\theta}}{\mathrm{d}w} =&-\frac{1}{3}\widetilde{\theta}^2-\widetilde{\sigma}_{\mu\nu}\widetilde{\sigma}^{\mu\nu}+\widetilde{\omega}_{\mu\nu}\widetilde{\omega}^{\mu\nu}-R_{\mu\nu}u^{\mu}u^{\nu}\\ =&-\frac{1}{3}\widetilde{\theta}^2-2\widetilde{\sigma}^2+2\widetilde{\omega}^2-R_{\mu\nu}u^{\mu}u^{\nu}.\end{aligned} \tag{4.12}$$

Equation (4.12) is known as Raychaudhuri's equation. The trace-free symmetric part of (4.11) is

$$\begin{aligned}\frac{\mathrm{D}\widetilde{\sigma}_{\mu\nu}}{\mathrm{d}w} =&-\frac{2}{3}\widetilde{\theta}\widetilde{\sigma}_{\mu\nu}-\widetilde{\sigma}_{\mu\lambda}\widetilde{\sigma}^{\lambda}{}_{\nu}+\widetilde{\omega}_{\mu\lambda}\widetilde{\omega}^{\lambda}{}_{\nu}+\frac{1}{3}\widetilde{h}_{\mu\nu}\left(\widetilde{\sigma}_{\pi\lambda}\widetilde{\sigma}^{\pi\lambda}-\widetilde{\omega}_{\pi\lambda}\widetilde{\omega}^{\pi\lambda}\right)\\ &+C_{\pi\nu\mu\lambda}u^{\pi}u^{\lambda}+\frac{1}{2}\widetilde{h}_{\mu\pi}\widetilde{h}_{\nu\lambda}R^{\pi\lambda}-\frac{1}{6}\widetilde{h}_{\mu\nu}\widetilde{h}_{\pi\lambda}R^{\pi\lambda},\end{aligned} \tag{4.13}$$

where $C_{\pi\nu\mu\lambda}$ is the Weyl tensor. Finally, the anti-symmetric part of (4.11) is

$$\frac{\mathrm{D}\widetilde{\omega}_{\mu\nu}}{\mathrm{d}w} = -\frac{2}{3}\widetilde{\theta}\widetilde{\omega}_{\mu\nu} - 2\widetilde{\sigma}^{\lambda}{}_{[\mu}\widetilde{\sigma}_{\nu]\lambda}. \tag{4.14}$$

Equations (4.13) and (4.14) have been included for completeness but will not be used again. In the next section we consider the form of (4.12) in the synchronous gauge.

4.2.1 Synchronous Gauge

The line element for the metric describing spacetime is taken to be

$$\mathrm{d}s^2 = -c^2\mathrm{d}t^2 + g_{ij}\mathrm{d}x^i\mathrm{d}x^j \tag{4.15}$$

where the coordinates are chosen to be comoving with the fluid. Note that a $3+1$ splitting of spacetime assumes that $\widetilde{\omega} = 0$ to ensure that a unique ct coordinate can be assigned to any event. Selection of the synchronous gauge is a loss of generality as it requires that clocks may be synchronised globally. This requirement is true of models commonly used to study cosmology, including the FRW model.

The parameter along the geodesic curves is chosen to be the time coordinate, ct, so that $u_\mu = (1,0,0,0)$ and $u^\mu u_\mu = -1$. With the time coordinate t, (4.9) becomes

$$c\widetilde{A}_{\mu\nu} = \frac{1}{3}\widetilde{\theta}\widetilde{h}_{\mu\nu} + \widetilde{\sigma}_{\mu\nu} + \widetilde{\omega}_{\mu\nu}. \tag{4.16}$$

u_μ may be thought of as representing the worldlines of objects (such as particles, observers or galaxies) which are comoving with the coordinate system and hence with the fluid. In a universe that is FRW this is equivalent to objects that are comoving with the Hubble flow.

The Ricci tensor in (4.12) may now be replaced using Einstein's field equations,

$$R^{\mu\nu} - \frac{1}{2}Rg^{\mu\nu} + \Lambda g^{\mu\nu} = \frac{8\pi G}{c^4}T^{\mu\nu} \tag{4.17}$$

and the energy-momentum tensor for pressureless dust,

$$T^{\mu\nu} = \rho c^2 u^\mu u^\nu \tag{4.18}$$

which together yield

$$R^{\mu\nu}u_\mu u_\nu = \frac{4\pi G\rho}{c^2} - \Lambda. \tag{4.19}$$

Therefore (4.12) becomes

$$\frac{\mathrm{d}\widetilde{\theta}}{\mathrm{d}t} = -\frac{1}{3}\widetilde{\theta}^2 - 2\widetilde{\sigma}^2 - 4\pi G\rho + \Lambda c^2. \tag{4.20}$$

By requiring conservation of energy-momentum ($T^{\mu\nu}{}_{;\nu} = 0$) we may also find an equation for the evolution of the matter density in terms of $\widetilde{\theta}$.

$$\begin{aligned} 0 = T^{\mu\nu}{}_{;\nu}\,u_\mu =& (\rho c^2 u^\mu u^\nu)_{;\nu} u_\mu \\ =& \rho_{;\nu} c^2 u^\mu u^\nu u_\mu + \rho c^2 u^\mu{}_{;\nu} u^\nu u_\mu + \rho c^2 u^\mu u^\nu{}_{;\nu} u_\mu \\ \frac{\mathrm{d}\rho}{\mathrm{d}t} =& -\rho u^\nu{}_{;\nu} = -\rho\widetilde{\theta}. \end{aligned} \tag{4.21}$$

Equation (4.21) shows that $\widetilde{\theta}$ does indeed describe expansion. If $\widetilde{\theta}$ is the normalised expansion rate of a volume V, $\widetilde{\theta} = \frac{\mathrm{d}V}{\mathrm{d}t}/V$ then (4.21) is merely a statement that the mass inside the volume is conserved.

4.3 Null Curves

We now turn to null curves, with tangent vector k^μ and parameter v. In section 4.2 the projection tensor $\widetilde{h}^\mu{}_\nu = g^\mu{}_\nu + u^\mu u_\nu$ was used to project relevant quantities into the spacelike hypersurface orthogonal to u^μ. There are two reasons for doing so. Firstly, (4.6) says the part of the deviation vector orthogonal to the geodesic remains orthogonal. The part of the deviation vector that is not orthogonal to the geodesic may only vary in one direction, that is, v_μ, and therefore is not very interesting. Secondly, as shown in figure 4.1 different deviation vectors to the same nearby geodesic geodesic differ by a multiple of v_μ. It is only useful to consider one of the connection vectors that connects two nearby geodesics. In the timelike case, restricting ξ_μ so that $\xi^\mu v_\mu = 0$ fulfils both conditions. The second vector in figure 4.1, $\widetilde{\xi}^\mu = \xi^\mu + \alpha v^\mu$, does not satisfy $\xi^\mu v_\mu = 0$ unless v^μ is null so an additional restriction is required in the null case. An equivalence class is therefore created containing all vectors that can be formed by adding a multiple

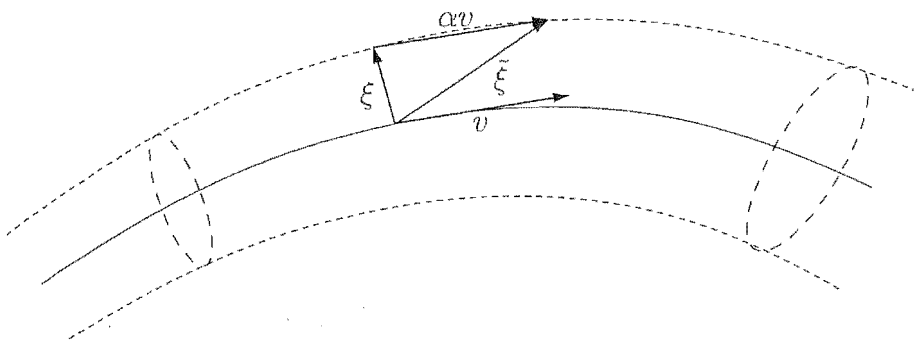

Figure 4.1: Deviation vectors to the same nearby geodesic differ by a multiple of k

of v^μ to ξ^μ. Only one vector of the equivalence class is considered. The additional restriction imposed in the null case reduces to two the dimension of the subspace containing the deviation vectors which are considered interesting.

We introduce a set of basis vectors $\{\mathbf{E}_1^\mu, \mathbf{E}_2^\mu, \mathbf{E}_3^\mu, \mathbf{E}_4^\mu\}$ with $\mathbf{E}_3^\mu \equiv k^\mu$ and $\mathbf{E}_4^\mu$ is another null vector satisfying $g_{\mu\nu}\mathbf{E}_3^\mu\mathbf{E}_4^\nu = 1$. $\mathbf{E}_1^\mu$ and $\mathbf{E}_2^\mu$ are spacelike unit vectors orthogonal to each other as well as to both $\mathbf{E}_3^\mu$ and $\mathbf{E}_4^\mu$. The basis vectors are parallely transported along the geodesic to provide a basis at every point along the geodesic and they retain these properties under parallel transport. As an example, in Minkowski space for a light beam propagating in the z direction these vectors might be

$$\begin{aligned}
\mathbf{E}_1^\mu &= (0,1,0,0) \\
\mathbf{E}_2^\mu &= (0,0,1,0) \\
\mathbf{E}_3^\mu &= \frac{1}{\sqrt{2}}(1,0,0,1) \\
\mathbf{E}_4^\mu &= \frac{1}{\sqrt{2}}(-1,0,0,1)\,.
\end{aligned} \tag{4.22}$$

The vectors $\{\mathbf{E}_1^\mu, \mathbf{E}_2^\mu, \mathbf{E}_3^\mu\}$ span the vector space containing all vectors orthogonal to k^μ. The vectors $\{\mathbf{E}_1^\mu, \mathbf{E}_2^\mu, \mathbf{E}_4^\mu\}$ span the vector space containing all equivalence classes of vectors that differ only by a multiple of k^μ. Therefore we are only interested in deviation vectors in the vector space spanned by $\{\mathbf{E}_1^\mu, \mathbf{E}_2^\mu\}$.

We take the components of ξ^μ with respect to the basis vectors $\{\mathbf{E}_1^\mu, \mathbf{E}_2^\mu\}$ to be

d_1 and d_2 so that

$$\xi^\mu(v) = \sum_{a=1,2} d_a(v)\mathbf{E}_a^\mu. \tag{4.23}$$

Taking the second covariant derivative of (4.23) and contracting with $\mathbf{E}_b^\nu g_{\mu\nu}$ yields

$$\frac{\mathrm{d}^2 d_a}{\mathrm{d}v^2} = \frac{\mathrm{D}^2\xi^\mu}{\mathrm{d}v^2}\mathbf{E}_a^\nu g_{\mu\nu} \tag{4.24}$$

since $\mathbf{E}_a^\mu$ undergoes parallel transport. The left hand side of (4.24) contains an ordinary derivative as d_a is not a vector but simply two scalars.

As in section 4.2 there is a projection tensor $\widehat{h}^\mu{}_\nu$ which projects into the vector space spanned by $\{\mathbf{E}_1, \mathbf{E}_2\}$. The trace of $\widehat{h}$ is two as the space is two dimensional. The definitions of the rates of expansion, shear and rotation follow as in section (4.2):

$$\widehat{\theta} = \widehat{A}^{\mu\nu}\widehat{h}_{\mu\nu}, \tag{4.25}$$

$$\widehat{\sigma}_{\mu\nu} = \widehat{A}_{(\mu\nu)} - \frac{1}{2}\widehat{\theta}\widehat{h}_{\mu\nu}, \tag{4.26}$$

$$\widehat{\omega}_{\mu\nu} = \widehat{A}_{[\mu\nu]} \tag{4.27}$$

so that

$$\widehat{A}_{\mu\nu} = \frac{1}{2}\widehat{\theta}\widehat{h}_{\mu\nu} + \widehat{\sigma}_{\mu\nu} + \widehat{\omega}_{\mu\nu}. \tag{4.28}$$

In section 4.2 evolution equations for the rates of expansion, shear and rotation were found using the evolution equation for $\widetilde{A}$. In the null case they will be found by considering the behaviour of the connection vector ξ^μ. We begin by deriving

the geodesic deviation equation,

$$\begin{aligned}
\frac{\mathrm{D}^2\xi^\mu}{\mathrm{d}v^2} &= k^\nu \left(k^\lambda \xi^\mu_{;\lambda}\right)_{;\nu} \\
&= k^\nu \left(\xi^\lambda k^\mu_{;\lambda}\right)_{;\nu} && \text{by (4.4)} \\
&= k^\nu \xi^\lambda_{;\nu} k^\mu_{;\lambda} + k^\nu \xi^\lambda k^\mu_{;\lambda\nu} \\
&= \xi^\nu k^\lambda_{;\nu} k^\mu_{;\lambda} + k^\nu \xi^\lambda k^\mu_{;\nu\lambda} + R^\mu{}_{\pi\nu\lambda} k^\pi k^\nu \xi^\lambda && \text{by (4.4) and Ricci's identity} \\
&= \xi^\nu k^\lambda_{;\nu} k^\mu_{;\lambda} + \xi^\nu k^\lambda k^\mu_{;\lambda\nu} + R^\mu{}_{\pi\nu\lambda} k^\pi k^\nu \xi^\lambda && \text{relabelling indices} \\
&= \xi^\nu \left(k^\lambda k^\mu_{;\lambda}\right)_{;\nu} + R^\mu{}_{\pi\nu\lambda} k^\pi k^\nu \xi^\lambda \\
\frac{\mathrm{D}^2\xi^\mu}{\mathrm{d}v^2} &= R^\mu{}_{\pi\nu\lambda} k^\pi k^\nu \xi^\lambda && \text{by (4.2).}
\end{aligned} \tag{4.29}$$

In flat space-time, the Riemann tensor is zero and (4.29) is $\frac{\mathrm{D}^2\xi^\mu}{\mathrm{d}s^2} = 0$. This means that geodesics that are initially parallel will remain parallel which is the expected behaviour in flat space-time, whereas in curved space-time the geodesics do not remain parallel.

Substituting (4.29) into (4.24) with ξ^λ on the right hand side of (4.29) given by (4.23), we obtain a deviation equation for the components of ξ^μ,

$$\frac{\mathrm{d}^2 d_a}{\mathrm{d}v^2} = \sum_{b=1,2} R_{\mu\pi\nu\lambda} \mathbf{E}^\mu_a k^\pi k^\nu \mathbf{E}^\lambda_b d_b. \tag{4.30}$$

Using the relationship (4.5), the covariant derivative of d_a may be expressed in terms of the rates of expansion, shear and rotation:

$$\begin{aligned}
\frac{\mathrm{D}\xi^\mu}{\mathrm{d}v} &= \widehat{A}^\mu{}_\nu \xi_\nu \\
\sum_{a=1,2} \frac{\mathrm{d}d_a}{\mathrm{d}v} \mathbf{E}^\mu_a &= \sum_{a=1,2} \widehat{A}^\mu{}_\nu d_a \mathbf{E}^\nu_a \\
\Rightarrow \qquad \frac{\mathrm{d}d_a}{\mathrm{d}v} &= \sum_{b=1,2} \widehat{A}_{\mu\nu} d_b \mathbf{E}^\mu_a \mathbf{E}^\nu_b \\
&= \sum_{b=1,2} \left(\frac{1}{2}\widehat{\theta}\widehat{h}_{\mu\nu} + \widehat{\sigma}_{\mu\nu} + \widehat{\omega}_{\mu\nu}\right) d_b \mathbf{E}^\mu_a \mathbf{E}^\nu_b \\
\frac{\mathrm{d}d_a}{\mathrm{d}v} &= \sum_{b=1,2} \left(\frac{1}{2}\widehat{\theta}\delta_{ab} + \widehat{\sigma}_{ab}\right) d_b,
\end{aligned} \tag{4.31}$$

where the two by two shear matrix $\widehat{\sigma}_{ab}$ is formed by contracting the four dimensional shear $\widehat{\sigma}_{\mu\nu}$ tensor with $\mathbf{E}^{\mu}_{a}\mathbf{E}^{\nu}_{b}$. The simplification that occurs with the last equality due to $\widehat{h}_{\mu\nu}\mathbf{E}^{\mu}_{a}\mathbf{E}^{\nu}_{b} = \delta_{ab}$ since $\mathbf{E}^{\mu}_{1}$ and $\mathbf{E}^{\mu}_{2}$ are orthogonal and $\widehat{\omega}_{\mu\nu}\mathbf{E}^{\mu}_{a}\mathbf{E}^{\nu}_{b} = 0$ since $\widehat{\omega}_{\mu\nu}$ is anti-symmetric.

Since $\widehat{\sigma}_{ab}$ is two by two, trace-free and symmetric, it must be of the form

$$\widehat{\sigma}_{ab} = \begin{bmatrix} \sigma_1 & \sigma_2 \\ \sigma_2 & -\sigma_1 \end{bmatrix}_{ab} \tag{4.32}$$

and so satisfies

$$\begin{aligned} \sum_{b=1,2} \widehat{\sigma}_{ab}\widehat{\sigma}_{bc} &= \left(\begin{bmatrix} \sigma_1 & \sigma_2 \\ \sigma_2 & -\sigma_1 \end{bmatrix} \begin{bmatrix} \sigma_1 & \sigma_2 \\ \sigma_2 & -\sigma_1 \end{bmatrix} \right)_{ac} \\ &= \begin{bmatrix} \sigma_1^2 + \sigma_2^2 & 0 \\ 0 & \sigma_1^2 + \sigma_2^2 \end{bmatrix}_{ac} = \delta_{ac}\widehat{\sigma}^2 \end{aligned} \tag{4.33}$$

where $\widehat{\sigma}^2 \equiv \sigma_1^2 + \sigma_2^2$.

Taking the derivative of (4.31) and substituting into (4.30) we obtain

$$\sum_{b=1,2} \left[\left(\frac{1}{2}\frac{\mathrm{d}\widehat{\theta}}{\mathrm{d}v} + \frac{1}{4}\widehat{\theta}^2 + \widehat{\sigma}^2 \right) \delta_{ab} + \frac{\mathrm{d}\widehat{\sigma}_{ab}}{\mathrm{d}v} + \widehat{\theta}\widehat{\sigma}_{ab} \right] d_b = \sum_{b=1,2} R_{\mu\pi\nu\lambda}\mathbf{E}^{\mu}_{a}k^{\pi}k^{\nu}\mathbf{E}^{\lambda}_{b}d_b. \tag{4.34}$$

The left hand side of (4.34) has a trace-free part (involving $\widehat{\sigma}$) and a part proportional to δ_{ab}. The right hand side can similarly be decomposed:

$$\begin{aligned} R_{\mu\pi\nu\lambda}\mathbf{E}^{\mu}_{a}k^{\pi}k^{\nu}\mathbf{E}^{\lambda}_{b} &= \Big[C_{\mu\pi\nu\lambda} + \frac{1}{2}\left(g_{\mu\nu}R_{\lambda\pi} - g_{\mu\lambda}R_{\nu\pi} + g_{\pi\nu}R_{\lambda\mu} - g_{\pi\lambda}R_{\nu\lambda} \right) + \\ &\qquad \frac{R}{6}\left(g_{\mu\lambda}g_{\nu\pi} - g_{\mu\nu}g_{\lambda\pi} \right) \Big] \mathbf{E}^{\mu}_{a}k^{\pi}k^{\nu}\mathbf{E}^{\lambda}_{b} \\ &= C_{\mu\pi\nu\lambda}\mathbf{E}^{\mu}_{a}k^{\pi}k^{\nu}\mathbf{E}^{\lambda}_{b} - \frac{1}{2}R_{\nu\pi}k^{\nu}k^{\pi}\delta_{ab}, \end{aligned} \tag{4.35}$$

where the first equality is the standard decomposition of the Riemann tensor into the trace-free part (the Weyl tensor) and the trace part; and the second equality is due to the orthogonality of $\mathbf{E}_1$ and $\mathbf{E}_2$.

Equating the trace-free and trace parts of (4.34) yields the following pair of

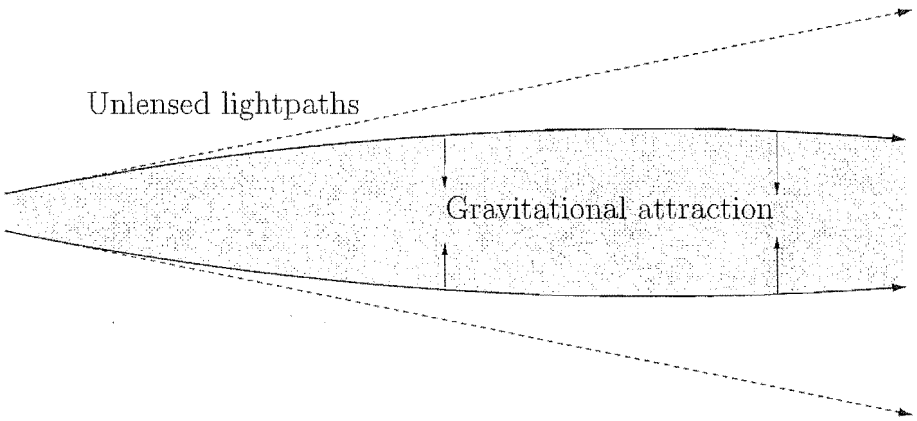

Figure 4.2: Ricci focusing of light beams

equations:

$$\frac{\mathrm{D}\widehat{\theta}}{\mathrm{d}v} + \frac{1}{2}\widehat{\theta}^2 + 2\widehat{\sigma}^2 = -R_{\nu\pi}k^\nu k^\pi \tag{4.36}$$

$$\frac{\mathrm{D}\widehat{\sigma}_{ab}}{\mathrm{d}v} + \widehat{\theta}\widehat{\sigma}_{ab} = C_{\mu\pi\nu\lambda}\mathbf{E}_a^\mu k^\pi k^\nu \mathbf{E}_b^\lambda. \tag{4.37}$$

4.3.1 Distance Measurements

Just as $\widetilde{\theta}$ in section 4.2 is the normalised volume expansion rate of space ($\widetilde{\theta} = \dot{V}/V$) when the timelike curves under consideration are the worldlines of stationary particles, $\widehat{\theta}$ in section (4.3) is the normalised expansion rate of the cross-sectional area of a light beam when the null curves under consideration are worldlines of a light beam ($\widehat{\theta} = \frac{\mathrm{d}A}{\mathrm{d}v}/A$). Since all cosmological distance measurements are based on the area of a light beam, (4.36) describes the evolution of a distance measurement along a light beam.

By transforming (4.36) into a differential equation for $\sqrt{A}$ and replacing the Ricci term using Einstein's field equations for pressureless dust, we arrive at the focusing equation

$$\frac{\mathrm{d}^2\sqrt{A}}{\mathrm{d}v^2} = -\left[\widehat{\sigma}^2 + \frac{4\pi G\rho}{c^2}\left(u_\mu k^\mu\right)^2\right]\sqrt{A}. \tag{4.38}$$

Equation (4.38) shows the different contributions to gravitational lensing. The $\widehat{\sigma}$ term is the shear term and is due to tidal forces acting on the light beam.

Although the derivation here does not allow for the formation of multiple images due to the assumption that the light rays form a congruence, the shear term is generally associated with strong lensing that causes multiple imaging. The ρ term is the direct influence of matter and is called Ricci focusing. It may be thought of as the gravitational attraction of matter inside the beam acting on the light rays as shown in figure (4.2). Equation (4.38) is called the focusing equation because the terms on the right hand side are positive definite and therefore lower the rate of increase of the cross-sectional area of the light beam.

The focusing equation will be used in chapter 6 to calculate the magnitude of distant objects. The magnitude calculation in chapter 6 requires knowledge of the distribution of matter and of the relationship between density and the rate of expansion of space. This is gained using the results of section 4.2.1 and is the subject of the next chapter.

Chapter 5

Distribution of Matter Inhomogeneities

5.1 Introduction

Chapter 3 shows that a complete study of gravitational lensing on cosmological scales must include the effect of inhomogeneities on the redshift of distant objects. The necessary mathematical tools are presented in chapter 4 and chapter 6 contains a description of a new method of calculating the magnitude-redshift relationship which incorporates the influence of inhomogeneities on the redshift. This new method requires knowledge of both the matter distribution and how the expansion rate of space varies with the matter density. This chapter describes the weakly non-linear evolution of density fluctuations and the time dependent relationship between density and expansion rate.

Section 5.2 briefly describes some of the terminology used to describe matter distributions. Section 5.3 describes a method used to explore the weakly non-linear regime of the growth of matter inhomogeneities. Since the main goal in chapter 6 is to quantify the contribution to lensing from the effect that local expansion rates have to the redshift of a light beam, the usual ways to model the growth of matter perturbations are not used. Section 5.4 describes the method used to quickly generate random numbers conforming to the matter distribution at a given time in a universe with given cosmological parameters and the local expansion rate of a region with a given matter density at that time and for that universe.

5.2 Matter Power Spectrum

The power spectrum of matter inhomogeneities is (Padmanabhan, 1993)

$$P(k) = \langle |\delta_{\mathbf{k}}|^2 \rangle, \tag{5.1}$$

which is the ensemble average of the square of the Fourier transform of the density contrast, where the density contrast δ is the departure from the background density ρ_b,

$$\delta(x) = \frac{\rho(x) - \rho_b}{\rho_b}. \tag{5.2}$$

Due to spatial isotropy of the matter distribution, $P(\mathbf{k}) = P(k)$ where $k = |\mathbf{k}|$.

The theory of inflation predicts that at the completion of the period of inflation $\delta_{\mathbf{k}}$ is a random variable with a Gaussian distribution. Since $\delta(\mathbf{x})$ is a sum of random Gaussian variables with zero mean, it too is a random Gaussian variable with zero mean. It can be shown that the variance satisfies

$$\langle \delta^2(\mathbf{x}) \rangle = \frac{1}{2\pi^2} \int_0^\infty P(k) k^2 \mathrm{d}k. \tag{5.3}$$

The linear evolution of the power spectrum may be calculated by perturbing the FRW equation. In the matter dominated universe the power spectrum evolves as

$$P_k(t) \propto a(t). \tag{5.4}$$

As modes grow in amplitude they move out of the linear regime. Linear and nonlinear modes grow at different rates, thus destroying the Gaussian distribution of the power spectrum.

5.3 Non-linear evolution of the power spectrum

The linear theory of matter fluctuations is thought to work well for primordial fluctuations but it is clear that there are regions of space at the present time with $\delta \gg 1$ where the linear evolution breaks down. The density contrast between the average densities of galaxies and clusters of galaxies and the background density

can be calculated from the approximate masses and sizes of these types of objects. The density contrasts on these two scales are of the order of 10^5 and $10 - 10^3$ respectively.

No analytic description of the non-linear evolution of the power spectrum is known. Peacock and Dodds (1996) use an N-body simulation to investigate the nonlinear evolution of the power spectrum. Although this and other methods such as smoothed particle hydrodynamics and the Zel'dovich approximation have been well studied, the focus of these approaches is galaxy formation and therefore of limited use when considering the intergalactic medium. Furthermore, while they provide a description of the matter distribution they are not designed to provide any information about the local expansion rate of space.

An alternative method is presented here which is suited to the non-linear evolution of lower density regions which do not form galaxies as well to as to slightly higher density regions and which also produces information about the local expansion rate of space. Non-gravitational interactions are ignored as is pressure so the method is unsuited to studies of structure formation. The method is easy to perform numerically for any universe, is applicable to non-linear evolution and naturally provides information on not only the density but also the local expansion rate of space.

From (4.20 - 4.21), the density at a point evolves as

$$\frac{\mathrm{d}\rho}{\mathrm{d}t} = -\theta\rho, \tag{5.5}$$

$$\frac{\mathrm{d}\theta}{\mathrm{d}t} = \Lambda - \frac{1}{3}\theta^2 - 4\pi G\rho. \tag{5.6}$$

These equations are non-perturbative but (5.6) is not exact as it neglects the anisotropic expansion (shear) and the rotation of the cosmolgical fluid. No explicit assumptions are made about the global nature of the universe but neglecting shear is tantamount to assuming that the universe is approximately FRW as an anisotropic universe will tend to induce shear. In particular it is not assumed that the universe is spherically symmetric, as the line element (4.15) does not require spherically symmetry. Spherical symmetry is not assumed in the remainder of this thesis. Equations (5.5) and (5.6) apply to the density (ρ_b) and expansion

rate (θ_b) in an exact FRW universe as well as to the density and expansion rate at a point. We can therefore calculate an evolution equation for δ.

$$\begin{aligned}
\frac{\mathrm{d}\rho}{\mathrm{d}t} = \frac{\mathrm{d}\rho_b(1+\delta)}{\mathrm{d}t} &= -\theta\rho \\
(1+\delta)\frac{\mathrm{d}\rho_b}{\mathrm{d}t} + \rho_b\frac{\mathrm{d}\delta}{\mathrm{d}t} &= -\theta\rho_b(1+\delta) \\
-(1+\delta)\theta_b\rho_b + \rho_b\frac{\mathrm{d}\delta}{\mathrm{d}t} &= -\theta\rho_b(1+\delta) \\
\Longrightarrow \qquad \frac{\mathrm{d}\delta}{\mathrm{d}t} &= (\theta_b - \theta)(1+\delta) \qquad (5.7)
\end{aligned}$$

It is convenient to work in scaled variables, $H_0 t$, θ/H_0 and $\hat{\rho} \equiv \rho_b/\rho_0$, with ρ_0 the current matter density. Using the standard definitions, $\Omega_m = 8\pi G\rho_0/3H_0^2$ and $\Omega_\Lambda = \Lambda/3H_0^2$ we then have as evolution equations for $\hat{\rho}$, δ, θ and θ_b,

$$\frac{\mathrm{d}\hat{\rho}}{\mathrm{d}(H_0 t)} = -\frac{\theta_b}{H_0}\hat{\rho}, \qquad (5.8)$$

$$\frac{\mathrm{d}\delta}{\mathrm{d}(H_0 t)} = \left(\frac{\theta_b}{H_0} - \frac{\theta}{H_0}\right)(1+\delta) \qquad (5.9)$$

$$\frac{\mathrm{d}(\theta/H_0)}{\mathrm{d}(H_0 t)} = 3\Omega_\Lambda - \frac{3}{2}\Omega_m\hat{\rho}(1+\delta) - \frac{1}{3}\left(\frac{\theta}{H_0}\right)^2 \qquad (5.10)$$

$$\frac{\mathrm{d}(\theta_b/H_0)}{\mathrm{d}(H_0 t)} = 3\Omega_\Lambda - \frac{3}{2}\Omega_m\hat{\rho} - \frac{1}{3}\left(\frac{\theta_b}{H_0}\right)^2. \qquad (5.11)$$

Equations (5.8) and (5.10) are integrated backwards from $H_0 t_0$ (the current age of the universe) to find the density and expansion rate of the universe at an early time, chosen to be at the CMB (recombination) or when the scale factor a was 1/1100 of its present value. $H_0 t_0$ is a model dependent quantity given by (Peebles, 1993)

$$H_0 t_0 = \int_1^\infty y^{-1}[\Omega_m y^3 + (1 - \Omega_m - \Omega_\Lambda)y^2 + \Omega_\Lambda]^{-1/2}\mathrm{d}y. \qquad (5.12)$$

The initial conditions used in the integration are $\{\hat{\rho}, \theta_b/H_0\} = \{1, 3\}$. The factor of three appears as θ is a volume expansion rate whereas a is a linear expansion rate.

The initial condition can now be set for θ. At the time of the CMB last scattering, t_{CMB}, the local expansion rate, θ, is assumed to be the same as the background expansion rate, θ_b. As the density perturbations are very small at t_{CMB} and

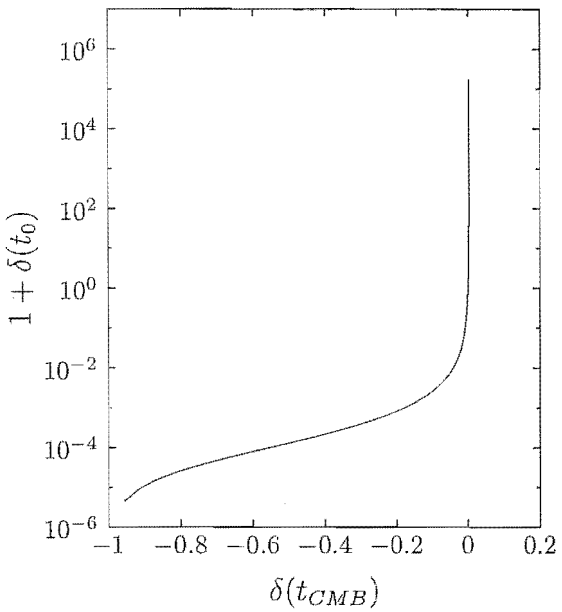

Figure 5.1: Evolution of density fluctuations. Primordial fluctuation is plotted against fluctuation at current time

the difference between θ and θ_b is driven by the density perturbations this is a reasonable assumption. Equations (5.8 - 5.11) are integrated forwards from t_{CMB} to $H_0 t_0$ for many values of $\delta(t_{CMB})$. This calculation results in a relationship between the initial density contrast in any region and the density contrast in that region at any later time up until the present; and another relationship between the initial density contrast and the expansion rate of any region at any later time up until the present.

The results are shown in figures 5.1 and 5.2 for a universe with $\Omega_m = 1$, $\Omega_\Lambda = 0$. Figure 5.1 shows the mapping between $\delta(t_{CMB})$ and $\delta(t_0)$. Negative values of δ, indicating underdense regions, evolve to even less dense regions. Overdense regions with $\delta > 0$ evolve to even more overdense regions, eventually collapsing as the expansion rate θ becomes negative. Since the model does not allow for pressure or any other mechanism to halt collapse, these regions quickly diverge. Figure 5.2 shows the expansion rate relative to the background expansion rate of regions with different densities. The local expansion rate is greater than the background expansion rate for $\delta < 0$ and less than the background rate for $\delta > 0$, becoming negative for high δ.

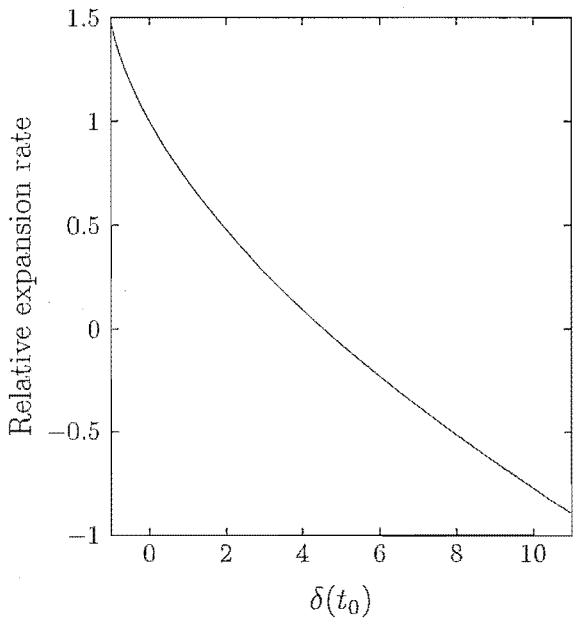

Figure 5.2: Local expansion rate relative to FRW expansion rate as a function of $\delta(t_0)$

The current matter distribution may be obtained by weighting each point of figure 5.1, the relationship between the density contrast at t_{CMB} and the present density contrast, with the appropriate initial probability. Figure 5.3 shows the distribution of matter today calculated from a Gaussian matter distribution at t_{CMB} with $\sigma^2 = 10^{-6}$. Since σ is used for other variables in this thesis, $\mathcal{V}_{CMB}$will be used instead to label the width of the matter distribution at t_{CMB}. All other parameters are as for figure 5.1. The probability distribution is skewed to the right suggesting that $\langle\delta\rangle > 0$. This is due in part to volume biasing – dense regions expand slower than average [1] (or collapse) and therefore take up a smaller fraction of space. The converse is true for underdense regions. Figure 5.3 therefore represents the probability density that a randomly selected region will have a given density, assuming that all regions had the same initial size. Figure 5.4 takes this factor into account by scaling the results from figure 5.3 by the relative volume of regions with given density so it represents the probability density that a randomly selected point in space will have a given density. The peak of the distribution is less than zero, indicating that the most common density is underdense. The mean of this distribution is $\langle\delta(t_0)\rangle = 0.62$ with a variance of

[1]The term "average" here refers to a simple arithmetic average over regions.

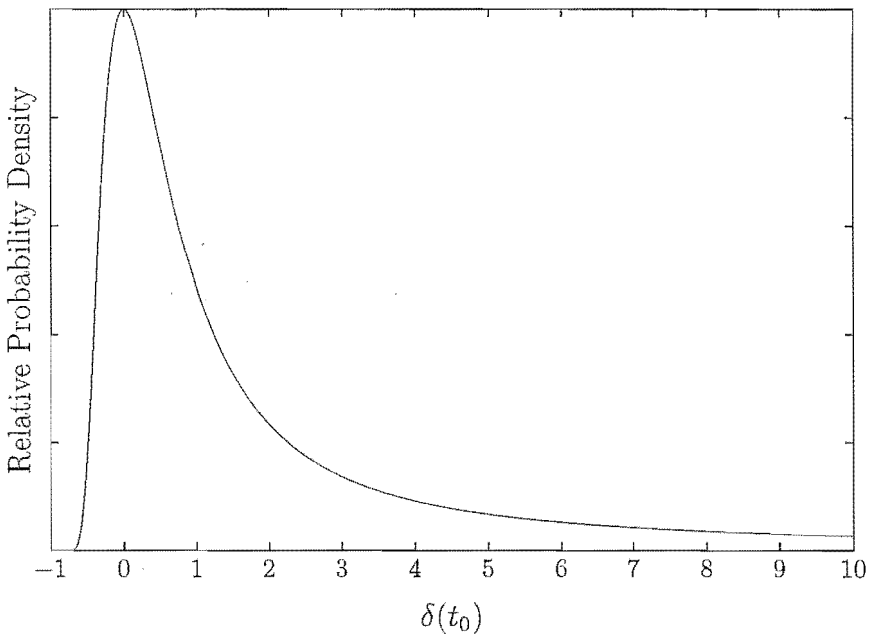

Figure 5.3: Current matter distribution with $\{\Omega_m, \Omega_\Lambda\} = \{1.0, 0.0\}$ and $\mathcal{V}_{CMB} = 10^{-6}$

$\sigma_\delta^2 = 1.94$. It is somewhat surprising that the mean is greater than zero. This may be due to limitations in the model, or it may be a real effect since δ is not the deviation from the mean but the deviation from the "background", or what the density would be in an equivalent FRW universe with the same values for the cosmological parameters. Buchert (2000) shows that an inhomogeneous universe is unlikely to have the same average expansion rate or density as an FRW universe with the same average density and the same cosmological constant and that the departure from the exact FRW is difficult to calculate. It would therefore be presumptive to draw any conclusions from the fact that $\langle\delta\rangle > 0$, either that there is any physical significance or that the model is deficient. Coles and Jones (1991) propose a log-normal distribution for the continuous density field and the best fit log-normal curve for the distribution is also shown in figure 5.4. The log-normal curve is a reasonable fit to the distribution.

Since the relationship between the matter density and the local expansion rate is known (figure 5.2), the distribution of θ may be obtained from the distribution of δ. This is shown in figure 5.5 for the matter distribution in figure 5.4. The mean is $\langle\theta(t_0)\rangle = 2.56H_0$ which is less than the background expansion rate: $\theta_b(t_0) = 3H_0$.

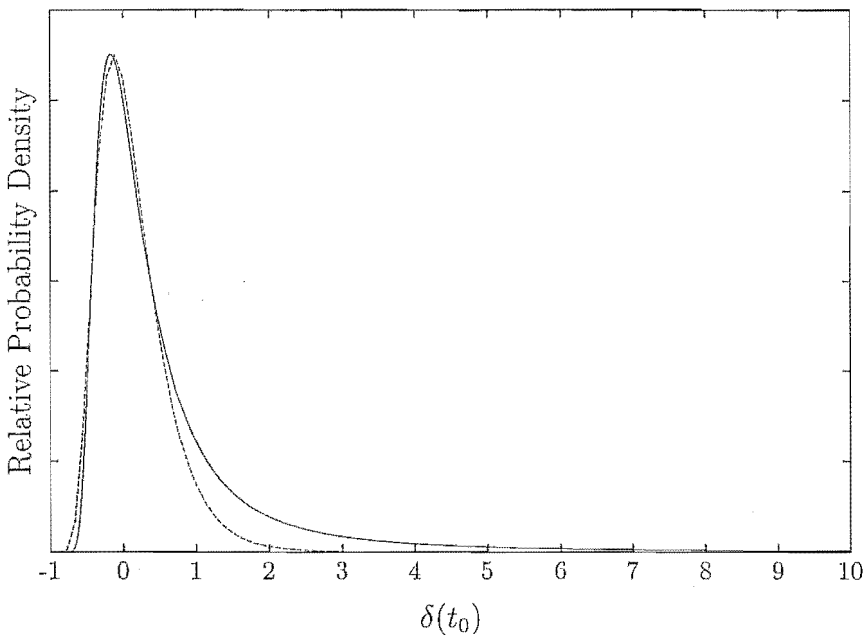

Figure 5.4: Current matter distribution as in figure 5.3 but scaled with relative volumes. Also shown (dotted lines) is a log-normal curve fitted to the distribution

This deviation is directly related to the deviation of $\langle\delta(t_0)\rangle$ from $\delta_b(t_0)$ and the same comments apply.

A different set of cosmological parameters leads to slightly different distributions. Figure 5.6 shows the current matter distribution for a different set of cosmological parameters, namely $\{\Omega_m, \Omega_\Lambda\} = \{1, 1\}$, as well as the best log-normal curve for the distribution. The peak is slightly further to the left when compared with figure 5.4 and the tail extends further to the right. This is partly due to the fact that the $\{\Omega_m, \Omega_\Lambda\} = \{1, 1\}$ universe is older than the $\{\Omega_m, \Omega_\Lambda\} = \{1, 0\}$ model (with $H_0 t_0 = 0.785$ for the former and $H_0 t_0 = 0.667$ for the latter) and partly due to universes evolving differently.

The matter distribution has clearly evolved away from the initial Gaussian distribution. This is necessary, as physically δ can never be less than -1 so the distribution cannot be symmetric when it goes non-linear. Figure 5.4 shows a log-normal curve $f = A\exp\left(-\left(\log(1+\delta) - \zeta\right)^2/\sigma'^2\right)$ fitted to the distribution. Best fit parameters are $\{A, \zeta, \sigma'\} = \{1.10, -0.13, 0.58\}$. It is a reasonably good fit to the distribution, especially close to zero. The log-normal curve shares the

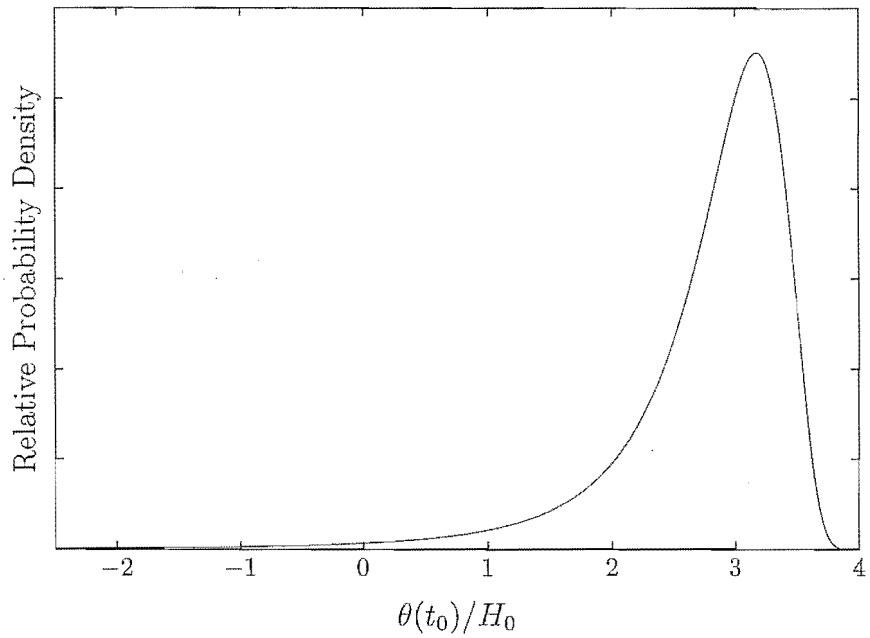

Figure 5.5: Current distribution of local expansion rates with $\{\Omega_m, \Omega_\Lambda\} = \{1.0, 0.0\}$ and $\mathcal{V}_{CMB} = 10^{-6}$

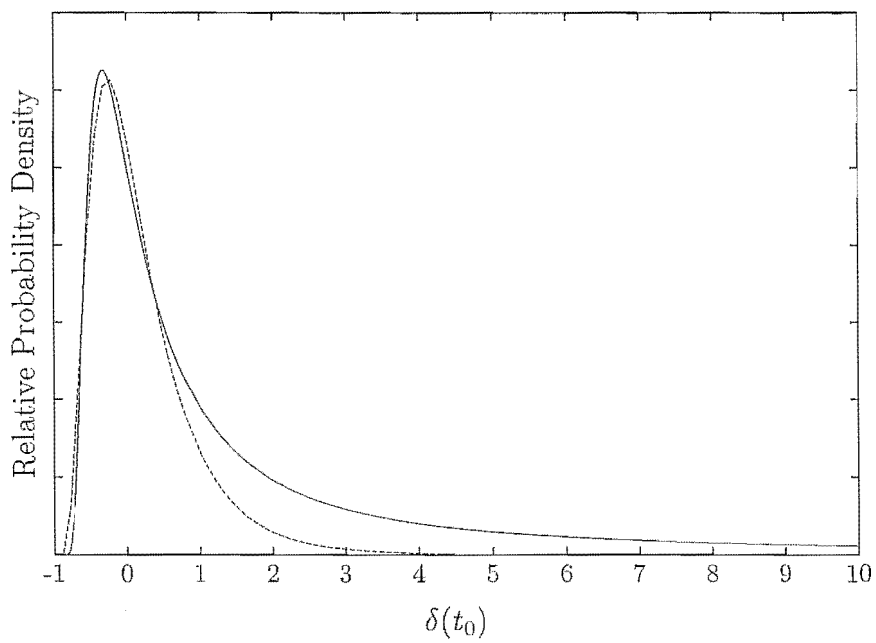

Figure 5.6: Current matter distribution for cosmological parameters $\{\Omega_m, \Omega_\Lambda\} = \{1, 1\}$. Also shown (dotted lines) is a log-normal curve fitted to the distribution

main features of the calculated matter distribution, namely a sharp peak with a long tail to the right but a very short tail to the left.

The log-normal distribution is a simple one which always has $\rho > 0$, unlike the Gaussian distribution. Nusser and Haehnelt (1999) also show that a log-normal distribution describes well the smoothed dark matter distribution in an N-body simulation. Despite the simplicity of the model presented in this chapter, the matter distribution it produces is very similar to the log-normal distribution which has strong justification. Coles and Jones (1991) cite a number of factors as motivation for the log-normal distribution for the continuous density field.

- Observations of galaxy distribution possibly reveal a log-normal distribution, although number counts of galaxies may be a biased tracer of the continuous field
- Generalising the Central Limit Theorem to non-linear noise produces log-normal random fields rather than Gaussian ones so that non-linear random processes can lead to log-normal matter distributions
- A kinematical theory with a Gaussian initial peculiar velocity field that grows linearly naturally has a log-normal matter distribution
- Biased galaxy formation from Gaussian linear fluctuations results in a log-normal distribution of the number of galaxies per unit mass inside a supercluster

The method used here to find matter distributions does not depend on the size of region under consideration but the use of them does. For example, a commonly cited quantity is σ_8, the rms density fluctuation averaged over spheres of size $8h^{-1}$Mpc. Although there is some disagreement as to the precise value of σ_8, it is of the order of unity (Peacock, 1999). Due to this result, the size of region used in chapter 6 will be $8h^{-1}$Mpc. Table 5.1 shows the rms matter fluctuations for various cosmological parameters and value of $\mathcal{V}_{CMB}$. The values of $\mathcal{V}_{CMB}$ which result in a present rms density fluctuation of around 1 are $\mathcal{V}_{CMB} = 10^{-6}$ and $\mathcal{V}_{CMB} = 10^{-7}$.

$\mathcal{V}_{CMB}$	$(\Omega_m,\Omega_\Lambda)$	Standard deviation	$\mathcal{V}_{CMB}$	$(\Omega_m,\Omega_\Lambda)$	Standard deviation
10^{-5}	(0.3,0.7)	2.59	10^{-7}	(0.3,0.7)	0.12
10^{-5}	(1.0,0.0)	2.72	10^{-7}	(1.0,0.0)	0.16
10^{-5}	(1.0,1.0)	2.76	10^{-7}	(1.0,1.0)	0.33
10^{-5}	(0.5,1.5)	2.79	10^{-7}	(0.5,1.5)	0.98
10^{-6}	(0.3,0.7)	0.84	10^{-8}	(0.3,0.7)	0.04
10^{-6}	(1.0,0.0)	1.39	10^{-8}	(1.0,0.0)	0.05
10^{-6}	(1.0,1.0)	2.25	10^{-8}	(1.0,1.0)	0.08
10^{-6}	(0.5,1.5)	2.62	10^{-8}	(0.5,1.5)	0.13

Table 5.1: Standard deviation of matter fluctuations for various cosmological parameters and $\mathcal{V}_{CMB}$

5.4 Computation

The matter distribution and the relationship between density and expansion rate that were found in the previous section are to be used to calculate the predicted magnitude of distant objects. Since the nature of such a calculation is probabilistic it must be performed many times to find the mean and standard deviation of the magnitude. To do this efficiently a function $F(p,t)$ is constructed which transforms a uniformly distributed random variable, p, into a random variable conforming to the required matter distribution at a given time; and a function $G(\delta,t)$ which yields the local expansion rate at a given time of a region with density δ. This section describes the construction of F and G.

For any combination of cosmological parameters and the width $\mathcal{V}_{CMB}$ of the Gaussian describing the initial matter perturbations, the background expansion rate and matter density at t_{CMB} are calculated as described in Section 5.3. A number n of different values for $\delta(t_{CMB})$ are selected and denoted $\delta_i(t_{CMB})$ with $i = 1..n$. The $\delta_i(t_{CMB})$ are not spaced uniformly as the curves in figures 5.4 and 5.6 change the most close to $\delta = 0$. Half of the values are between $\pm\sqrt{\mathcal{V}_{CMB}}$ with the other half spread between ± 1. Since the distributions are quite smooth n can be small and we found $n = 50$ to be satisfactory. Each δ_i is evolved forwards in time simultaneously with θ_i/H_0 and V_i/V_b using (5.9) and (5.10). Values

for $\{\delta_i(t), \theta_i(t)/H_0, V_i(t)/V_b(t)\}$ are kept for a large number of uniformly spaced intermediate times.

The probability density at time t of a random point in space having density $\rho_b(1 + \delta_i(t))$ is proportional to

$$P(\delta_i(t)) \propto \frac{V_i}{V_b} \exp\left(-\frac{\delta_i(t_{CMB})}{\mathcal{V}_{CMB}}\right). \tag{5.13}$$

This is simply a Gaussian probability distribution scaled by relative volumes as discussed in Section 5.3. At each intermediate time, the probability distribution is integrated in order to normalise it since the total probability must be one,

$$\int_{-1}^{\infty} P(\delta(t))\mathrm{d}\delta \equiv 1. \tag{5.14}$$

The inverse of the function $F(p,t)$ is simply the integral of the normalised probability distribution (Press, 1992). A number of points in $F^{-1}(\delta, t)$ are calculated by integration,

$$F(\delta_i, t) = \int_{-1}^{\delta_i} P(\delta(t))\mathrm{d}\delta \tag{5.15}$$

and an Akima spline through these points is constructed. A separate spline is constructed for each time at which the matter distribution has been calculated. This completes the formation of $F(p,t)$. The construction of $G(p,t)$ is simpler, requiring only a spline through the pairs of values $\{\delta_i(t), \theta_i(t)/H_0\}$ for each intermediate time.

Figures 5.7 and 5.8 show the result of generating a very large number of random δ and θ using $F(p,t)$ and $G(p,t)$ for the $\{\Omega_m, \Omega_\Lambda\} = \{1, 0\}$ cosmology at the current time. A comparison with figures 5.4 and 5.5 clearly show that the distributions are the same, thus validating the method used to quickly generate random densities with the correct distribution.

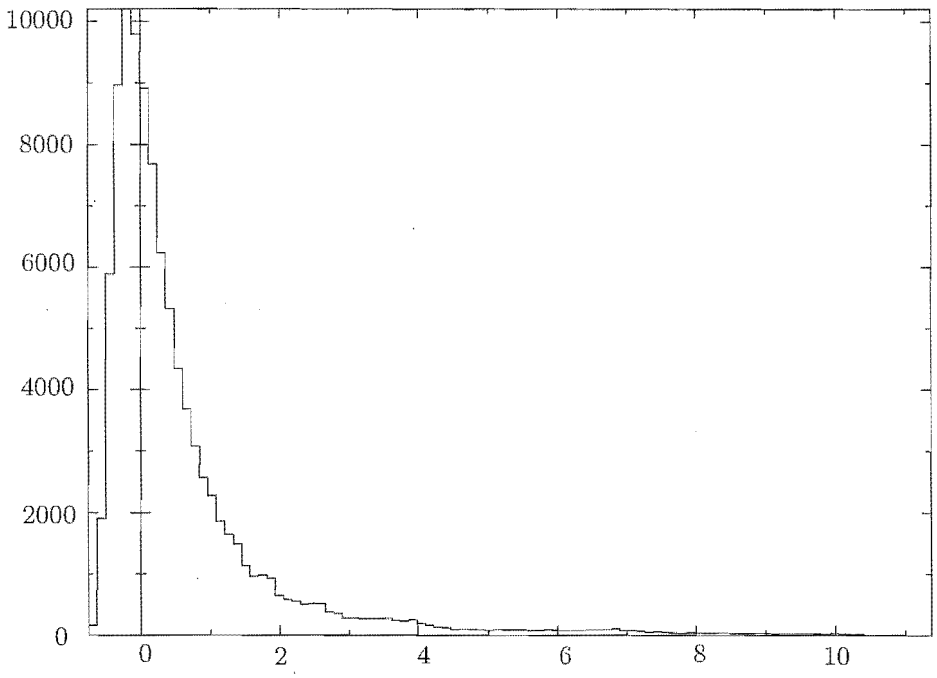

Figure 5.7: Current matter distribution for cosmological parameters $\{\Omega_m, \Omega_\Lambda\} = \{1, 0\}$

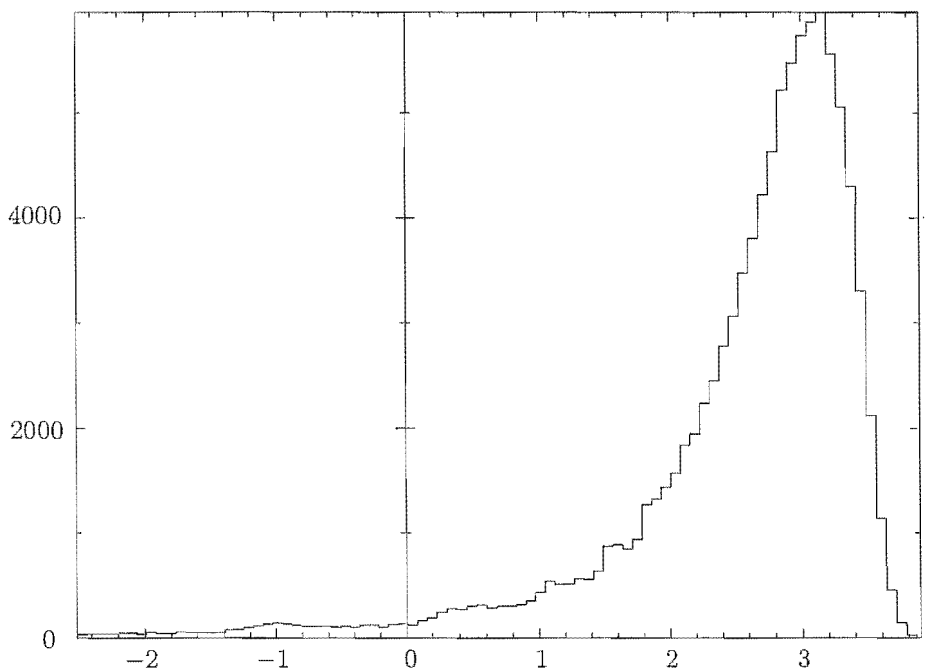

Figure 5.8: Current expansion rate distribution for cosmological parameters $\{\Omega_m, \Omega_\Lambda\} = \{1, 0\}$

Chapter 6

A new method of calculating the luminosity distance

6.1 Introduction

This chapter investigates the effect on the magnitude-redshift relationship of a varying local rate of expansion of space due to matter inhomogeneities and the influence that modifying the magnitude-redshift relationship has on cosmological parameter estimation from supernovæ data. Section 6.2 derives the equations used to calculate the magnitude-redshift relationship starting from the results presented in chapter 4. Section 6.3 investigates the relationship between the lookback time and redshift, especially in a situation where a typical lightpath tends to go through underdense regions. Section 6.4 looks at the magnitude-redshift relationship and compares the magnitudes of unlensed objects to the magnitudes of lensed objects, as calculated using the equations derived in section 6.2. The distribution of the magnitudes of lensed objects is also discussed. Section 6.5 uses the magnitude relationship derived in section 6.2 and the supernovæ data to determine cosmological parameters.

It is appropriate to recap here all the assumptions made up to this point. We divide the universe up into regions of space of a uniform size of $8h^{-1}$Mpc. The matter content is pressureless dust. The regions are non-rotating and have small rates of shear relative to their rates of expansion. Although nowhere is it explicitly assumed that the universe approximates a FRW universe, assuming a negligible

rate of shear is tantamount to assuming an on-average FRW universe as a non-isotropic matter distribution will give rise to shear. The velocities of the particles in these regions are also neglected.

6.2 Differential equation used to find the luminosity distance

In section 4.3.1 the focusing equation,

$$\frac{\mathrm{d}^2\sqrt{A}}{\mathrm{d}v^2} = -\left[\widehat{\sigma}^2 + \frac{4\pi G\rho}{c^2}\left(u_\mu k^\mu\right)^2\right]\sqrt{A} \tag{6.1}$$

was derived.

As a beam of light crosses a region of space, the affine parameter v, the time t and the redshift z all vary and all may be expressed in terms of the others. The exact relationship between any pair depends on the cosmological parameters and is also influenced by gravitational lensing due to the appearance of $\widetilde{\theta}$ in (6.6) and (6.7). z either increases or decreases depending on the sign of $\widetilde{\theta}$ and neither t nor v may be applied to observations directly as they cannot be directly observed. Since the matter distribution is dependent on t, it is most convenient to use t to parameterise (6.1).

There is a freedom in the affine parameter that must be fixed before finding any relationship between v, t and z. Since we have $k^\mu = \mathrm{d}x^\mu/\mathrm{d}v$, the freedom may be fixed by setting

$$u_\mu k^\mu = \frac{c}{H_0}(1+z). \tag{6.2}$$

The factor of $1+z$ appears in (6.2) as k is the wave vector and hence varies with the frequency of the light. In the synchronous gauge (see section 4.2.1), $u_j \equiv 0$, so $\mathrm{d}t/\mathrm{d}v$ may be easily found as follows,

$$\begin{aligned}\frac{c}{H_0}(1+z) = u_\mu k^\mu = u_\mu\frac{\mathrm{d}x^\mu}{\mathrm{d}v} = u_0\frac{\mathrm{d}x^0}{\mathrm{d}v} = 1\frac{\mathrm{d}ct}{\mathrm{d}v}\\ \Rightarrow \frac{\mathrm{d}t}{\mathrm{d}v} = \frac{1+z}{H_0}.\end{aligned} \tag{6.3}$$

Taking the covariant derivative of (6.2), contracting with k^ν and noting that $(u_\mu k^\mu)_{;\nu} k^\nu = u_{\mu;\nu} k^\mu k^\nu = A_{\mu\nu} k^\mu k^\nu$ (see page 40), we have, using (4.16)

$$\frac{c}{H_0}\frac{\mathrm{d}z}{\mathrm{d}v} = \left(u_\mu k^\mu\right)_{;\nu} k^\nu = -\frac{1}{c}\left(\frac{1}{3}\widetilde{\theta h}_{\mu\nu} + \widetilde{\sigma}_{\mu\nu} + \widetilde{\omega}_{\mu\nu}\right) k^\mu k^\nu, \tag{6.4}$$

where $\widetilde{h}$, $\widetilde{\theta}$, $\widetilde{\sigma}$ and $\widetilde{\omega}$ have the same meanings as in section 4.2. The sign of the last equation has been chosen to ensure that z increases with distance when the expansion rate is positive. The freedom to insert a minus sign is due to setting the direction of v to point into the future.

Recalling that $k^\mu k_\nu = 0$ and that $u^\mu u_\nu = -1$, (6.4) may be simplified by splitting k^μ into a part parallel to u^μ and a part, e^μ, which is orthogonal to u^μ and is a spacelike unit vector,

$$k^\mu = -\frac{c}{H_0}(1+z)(u^\mu + e^\mu). \tag{6.5}$$

Since $\widetilde{h}$ is defined to be $\widetilde{h}^\mu{}_\nu \equiv g^\mu{}_\nu + u^\mu u_\nu$ (see section 4.2), $\widetilde{h}^\mu{}_\nu u_\mu u^\nu = 0$ and $\widetilde{h}^\mu{}_\nu e_\mu e^\nu = 1$. Thus (6.4) now becomes

$$\begin{aligned}
\frac{c}{H_0}\frac{\mathrm{d}z}{\mathrm{d}v} &= -\frac{1}{c}\left(\frac{1}{3}\widetilde{\theta h}_{\mu\nu} + \widetilde{\sigma}_{\mu\nu} + \widetilde{\omega}_{\mu\nu}\right)\frac{c^2}{H_0^2}(1+z)^2\left(u^\mu + e^\mu\right)\left(u^\nu + e^\nu\right) \\
H_0\frac{\mathrm{d}z}{\mathrm{d}v} &= -\left(\frac{1}{3}\widetilde{\theta h}_{\mu\nu} + \widetilde{\sigma}_{\mu\nu}\right)(1+z)^2 e^\mu e^\nu \\
&\approx -\frac{1}{3}\widetilde{\theta}(1+z)^2.
\end{aligned} \tag{6.6}$$

In the last step the assumption has been made that the isotropic expansion of space is much greater than the rate of shear of space, $\widetilde{\sigma} \ll \widetilde{\theta}$ with the consequence that $\widetilde{\sigma}$ has been neglected. When this assumption is not valid, equation (6.6) may still be approximately correct as the shear term is directional through the e^μ dependence. As the light beam travels through different regions we may expect that in a universe which is homogeneous on large scales that the contributions to equation (6.6) from shear cancel out.

Finally, using (6.3), (6.6) becomes

$$\frac{\mathrm{d}z}{\mathrm{d}t} \approx -\frac{\widetilde{\theta}}{3}(1+z). \tag{6.7}$$

Returning now to the focusing equation and using (6.3) to perform a change of variables from v to t and substituting (6.2) and (6.7), (6.1) becomes

$$\frac{\mathrm{d}^2\sqrt{A}}{\mathrm{d}(H_0 t)^2} - \frac{\widetilde{\theta}}{3H_0}\frac{\mathrm{d}\sqrt{A}}{\mathrm{d}H_0 t} + \frac{4\pi G\rho}{H_0^2}\sqrt{A} = 0. \tag{6.8}$$

The rate of shear of the light beam has been neglected to obtain (6.8). This is a different assumption to neglecting the shear in the derivation of (6.6) as the rate of shear of a light beam is different to the rate of shear of space and also because the shear in (6.1) always has the effect of focusing the light beam. However, for weak lensing the effect of the shear of the light beam is small and may be neglected, as discussed by Kantowski (1969).

To transform (6.8) from an evolution equation for the area of a light beam into an evolution equation for the luminosity distance, we first use the definition of the angular diameter distance d_A as the two distance definitions are simply related as is discussed in chapter 1. With $\delta\Omega$ the solid angle that the object subtends on the sky and A the area of the object on the size, the angular diameter distance is simply (Schneider *et al.*, 1992)

$$d_A = \sqrt{\frac{A}{\delta\Omega}} \tag{6.9}$$

so that the evolution equation for d_A is

$$\frac{\mathrm{d}^2 d_A}{\mathrm{d}(H_0 t)^2} - \frac{\widetilde{\theta}}{3H_0}\frac{\mathrm{d}d_A}{\mathrm{d}H_0 t} + \frac{4\pi G\rho}{H_0^2} d_A = 0. \tag{6.10}$$

Equation (6.10) is the equation used to calculate the angular diameter distance for the main results of this chapter. The first initial condition is trivially

$$d_A = 0 \qquad \text{at} \qquad t = t_0. \tag{6.11}$$

The second initial condition follows from requiring that the Euclidean distance is a limiting case of the angular diameter distance at small distances, which leads to

$$\frac{\mathrm{d}d_A}{\mathrm{d}(H_0 t)} = -\frac{c}{H_0} \qquad \text{at} \qquad t = t_0. \tag{6.12}$$

Equation (6.10) differs from the standard result by allowing the local expansion rate of space, $\widetilde{\theta}$, and the local matter density, ρ, to vary from point to point. By

replacing $\widetilde{\theta}$ and ρ with the expansion rate and matter density in the FRW universe, the FRW result is recovered. For easy comparison with standard results this is presented here with ρ_{FRW} evolving from the current matter density ρ_0 according to

$$\rho_{FRW} = \frac{\rho_0}{a(t)^3} = \rho_0(1+z)^3 \tag{6.13}$$

since $1 + z = 1/a(t)$ in the FRW universe. $\widetilde{\theta}_{FRW}$ is given by the Friedmann equation, equation (1.2),

$$\widetilde{\theta}_{FRW} = 3\frac{\dot{a}}{a} = 3H_0\sqrt{\Omega_m(1+z)^3 + \Omega_\Lambda + (1-\Omega_m-\Omega_\Lambda)(1+z)^2}. \tag{6.14}$$

Using (6.7) to transform (6.10) and substituting (6.13) and (6.14) gives the FRW differential equation for d_A:

$$\begin{aligned}\left[\Omega_m(1+z)^2 + \Omega_\Lambda(1+z)^{-1} + (1-\Omega_m-\Omega_\Lambda)(1+z)\right]\frac{\mathrm{d}^2 d_A}{\mathrm{d}z^2} \\ + \left[\frac{7}{2}\Omega_m(1+z) + 2\Omega_\Lambda(1+z)^{-2} + 3(1-\Omega_m-\Omega_\Lambda)\right]\frac{\mathrm{d}d_A}{\mathrm{d}z} \\ + \frac{3}{2}\Omega_m d_A = 0.\end{aligned} \tag{6.15}$$

The Dyer-Roeder distance (Dyer and Roeder, 1972) (but see also Kantowski (1969)) modifies (6.15) to account for matter clumping. Dyer and Roeder reason that the matter terms in the coefficients of the derivatives in (6.15) arise due to transforming coordinates from v to z and that on average the matter distribution will not effect such a coordinate transformation. Therefore the only influence matter clumping may have on the angular diameter distance is through the last term in (6.15). If the universe has a fraction $1-\alpha$ of matter in clumped objects and observed light beams do not pass near any clumps so that shear is negligible then only a fraction α of the total matter will contribute to the last term of (6.15). The Dyer-Roeder distance is therefore

$$\begin{aligned}\left[\Omega_m(1+z)^2 + \Omega_\Lambda(1+z)^{-1} + (1-\Omega_m-\Omega_\Lambda)(1+z)\right]\frac{\mathrm{d}d_A^2}{\mathrm{d}z^2} \\ + \left[\frac{7}{2}\Omega_m(1+z) + 2\Omega_\Lambda(1+z)^{-2} + 3(1-\Omega_m-\Omega_\Lambda)\right]\frac{\mathrm{d}d_A}{\mathrm{d}z} \\ + \frac{3}{2}\alpha\Omega_m d_A = 0.\end{aligned} \tag{6.16}$$

The value of α is not well known, although Mörtsell *et al.* (2001) show that future observations of supernovæ should allow us to determine the fraction of compact objects in the universe. Kantowski and Thomas (2001) have attempted to determine α from existing supernovæ data and find the data are inadequate for the task.

The assumption that the average expansion rate of the universe does not depend on the matter distribution is crucial to the derivation of the Dyer-Roeder distance. Buchert (2000) has shown this assumption to be incorrect. If we then assume that the matter distribution *does* affect the expansion rate of the universe, we must ask if this in turn affects the calculation of the luminosity distance and the determination of cosmological parameters from the supernovæ data.

The magnitude of a distant object may be calculated from the luminosity distance according to (2.4):

$$m_B^{eff} = \mathcal{M} + 5\log(\mathcal{D}_L), \tag{6.17}$$

where $d_L = (1+z)^2 d_A$ according to the reciprocity relation (Schneider *et al.*, 1992), $\mathcal{D}_L \equiv H_0 d_L$ is the "Hubble constant free" luminosity distance and $\mathcal{M}$ is a nuisance parameter.

To compute the angular diameter distance we solve (6.10) backwards from $t = t_0$ for any combination of the cosmological parameters $\{\Omega_m, \Omega_\Lambda\}$. The redshift, z, is simultaneously solved using (6.7).

The universe through which the beam of light travels is divided into regions of a uniform size of $8h^{-1}$Mpc since the amplitude of the present rms matter fluctuations averaged over this scale are known, as discussed at the end of section 5.3. The region size varies with $a \approx 1/(1+z)$. This is no longer an exact relationship as in the inhomogeneous universe the redshift depends on the matter density of the regions that the light beam traverses. For each region random values for the matter density and local expansion rate are chosen according to the distribution described in Chapter 5.4. Values for d_A are stored at each redshift at which a supernova magnitude is known.

When $\theta < 0$ the region is contracting – the region is dense enough to break away

from the expansion of the universe but is not yet dense enough for rotation or pressure to stop the contraction. The redshift will then decrease across the region rather than increase as is usual.

Since the matter density and the local expansion rate in (6.10) are random variables, d_A is not a definite function but rather one that can have a range of values at a given redshift. The differential equation (6.10) is therefore solved many times for a given model and the mean effective magnitude, $m_B^{eff}(z)$, and the standard deviation in effective magnitude, $\sigma_{\text{model}}(z)$, calculated for every redshift at which a supernova has been observed. The model uncertainty, σ_{model}, is incorporated into the calculation of the χ^2 calculation to give a new goodness of fit statistic:

$$\chi^2 = \sum_i \frac{\left(m_B^{eff}(z_i) - m_i\right)^2}{\sigma_i^2 + \sigma_{\text{model}}^2(z_i)}. \tag{6.18}$$

6.3 Lookback time - redshift relationship

An examination of (6.7) reveals that if the average expansion rate of space that a light beam traverses in an inhomogeneous universe is the same as the expansion rate of space in a homogeneous universe, then the light beam will be redshifted by the same amount in each case. Obtaining an integral equation from (6.7),

$$\begin{aligned} \int_0^z \frac{\mathrm{d}(1+z')}{1+z'} &= \int_{t_1}^{t_0} \frac{\widetilde{\theta}}{3}\mathrm{d}t \\ \ln(1+z) &= \int_{t_1}^{t_0} \frac{\widetilde{\theta}}{3}\mathrm{d}t \end{aligned} \tag{6.19}$$

where the integral is understood to be over the path of the light beam from the source at $\{z,t\} = \{z,t_1\}$ to the observer at $\{z,t\} = \{0,t_0\}$, we see that the redshift results from the integral of $\widetilde{\theta}$ over the path of the light beam. The influence on the redshift of regions with high expansion rates will tend to cancel the effect from regions with low expansion rates. We expect to see some variation in the lookback time-redshift relationship as some light paths will go through more overdense regions and some will go through more underdense regions but since light from distant sources goes through many different regions the variation is

likely to be small. Since (6.19) shows that the redshift does not depend linearly on the expansion rate, the mean redshift at a given lookback time is not necessarily the redshift related to the mean integrated expansion rate. This effect is expected to be very small, especially for sources at high redshifts, as the variation in the lookback time-redshift relationship over different lightpaths is expected to be small.

Although the results of section 5.3 indicate that the average expansion rate in an inhomogeneous universe may well be different to the expansion rate in a homogeneous universe with the same cosmological parameters, the magnitude and even direction of this effect are unknown. On the other hand, the assumptions under which the Dyer-Roeder distance is derived include light beams which reach us from distant parts of the universe passing through regions of space which are, on average, underdense due to some fraction of the total matter content being bound in clumps. Since most of the light path is through underdense regions which expand faster than the average, objects at a given redshift are closer to us than they would be according to the FRW redshift-distance relationship and therefore the light travel time is lower and they appear brighter than we would otherwise expect. A distance-redshift relationship which takes this into account will be called the modified Dyer-Roeder distance. The modified Dyer-Roeder distance obeys (6.10) with a matter distribution adjusted to ensure that the average matter density of regions through which the light beam travels is a α times the average matter density.

The light travel time to an object at a redshift of $z = 1$ is calculated under the assumption that the light beams travel through regions of space which contain, on average, a fraction α of the average density of space and that these regions expand at a different rate to the average. This calculation was performed over a grid of cosmological parameters in the plane $0 \leq \Omega_m, \Omega_\Lambda \leq 1$ and the light travel time compared to the light travel time in the corresponding FRW universe. Figures 6.1 and 6.2 show the difference between light travel time calculated using the assumptions behind the modified Dyer-Roeder distance and calculated in a FRW universe, in units of $H_0 t$. Figure 6.1 is with $\alpha = 0.9$ and figure 6.2 is with $\alpha = 0.5$.

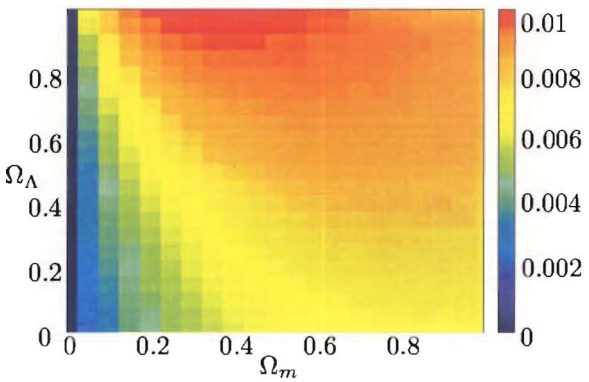

Figure 6.1: Difference in light travel time in units of $H_0 t$ to a source at $z = 1$ between a FRW universe and a universe with 0.1 of matter in clumps ($\alpha = 0.9$). Positive values indicate a higher light travel time in the FRW universe

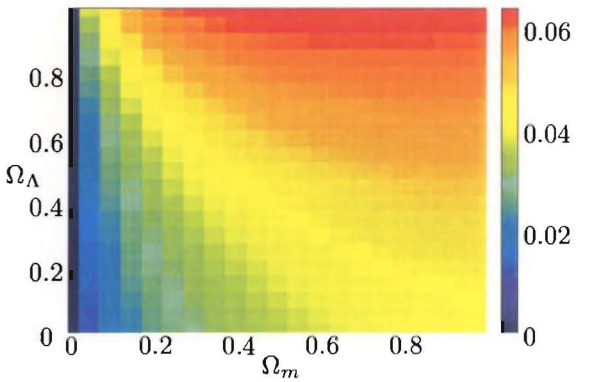

Figure 6.2: As for figure 6.1 but with $\alpha = 0.5$

Results are shown over the plane $0 \leq \Omega_m, \Omega_\Lambda \leq 1$, with the degree of the effect given by the shading and a legend to the right of the plot.

Since all effects are proportional to the matter density, there is a difference of 0 along the line $\Omega_m = 0$ and, as a rule, the effect grows with increasing Ω_m. The effect also grows with increasing Ω_Λ as universes with high Ω_Λ tend to be older. This can be seen in figure 6.1 where the highest difference is at $\{\Omega_m, \Omega_\Lambda\} = \{0.3, 1.0\}$, a model which has an age of $H_0 t_0 \approx 1.08$ whereas the $\{\Omega_m, \Omega_\Lambda\} = \{1.0, 1.0\}$ model has an age of $H_0 t_0 \approx 0.78$.

The magnitude of an object at $z = 1$ according to the modified Dyer-Roeder distance relationship is compared to the magnitude as calculated using the FRW magnitude-redshift relationship in figures 6.3 and 6.4 which show the difference between the two magnitude calculations. Negative values indicate that the modified Dyer-Roeder magnitude is lower than the FRW magnitude; or that the source appears brighter than the FRW calculation leads us to expect. Figure 6.3 is with $\alpha = 0.9$ and figure 6.4 is with $\alpha = 0.5$.

The Dyer-Roeder distance predicts that observed objects appear dimmer than the FRW relationship due to decreased Ricci focusing while the effect of the

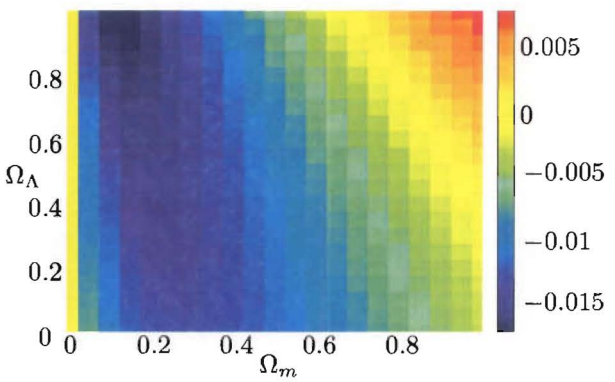

Figure 6.3: Magnitude difference for a source at $z = 1$ between the FRW calculated value and the modified Dyer-Roeder calculated value with $\alpha = 0.9$. Positive values indicate that the object is observed to be brighter in the FRW universe

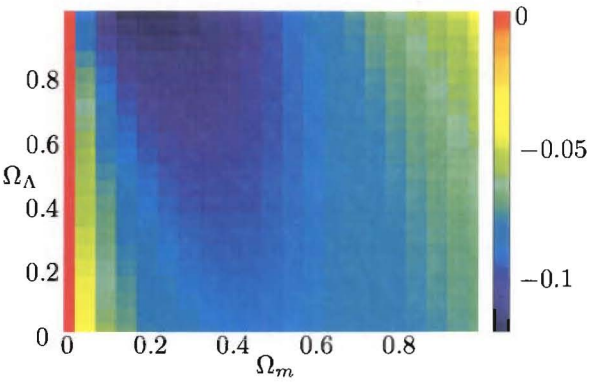

Figure 6.4: As for figure 6.3 but with $\alpha = 0.5$

modifications to take a variable local rate of expansion into account is to make observed objects at a given redshift appear brighter. Figure 6.3 shows that these two effects come remarkably close to cancelling each other out with $\alpha = 0.9$, as for some regions of parameter space the modified Dyer-Roeder distance predicts that objects at $z = 1$ appear brighter than the FRW relationship predicts and for some regions it is the other way around. On the other hand, figure 6.4 shows that with $\alpha = 0.5$ the effect of the decreased Ricci focusing outweighs the effect of the variable local rate of expansion of space and the modified Dyer-Roeder distance is greater than the FRW distance over the entire grid. The effect is in general much smaller than the Dyer-Roeder distance alone - for comparison figures 6.5 and 6.6 show the difference between the Dyer-Roeder magnitude and the FRW magnitude with $\alpha = 0.9$ and $\alpha = 0.5$ respectively.

The modified Dyer-Roeder magnitude is moderately different to the FRW magnitude, especially with low values of α. Differences of about 0.1 magnitudes are large when compared to the size of the uncertainty on the mean magnitude of the bins describing the supernovæ data. The uncertainty in the bins ranges from 0.046 magnitudes to 0.340 magnitudes with most values being close to 0.1

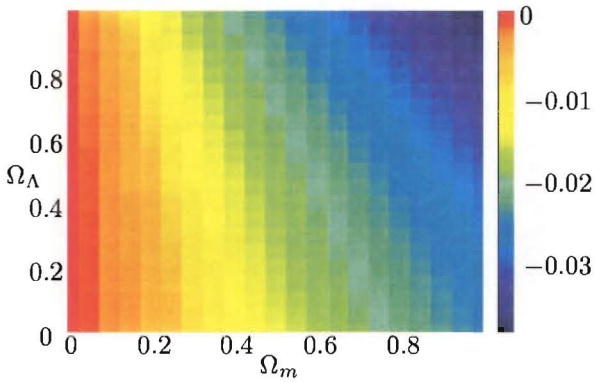

Figure 6.5: Difference between FRW magnitude and Dyer-Roeder magnitude with $\alpha = 0.9$ for a source at $z = 1$. Positive values indicate that the object is observed to be brighter in the FRW universe

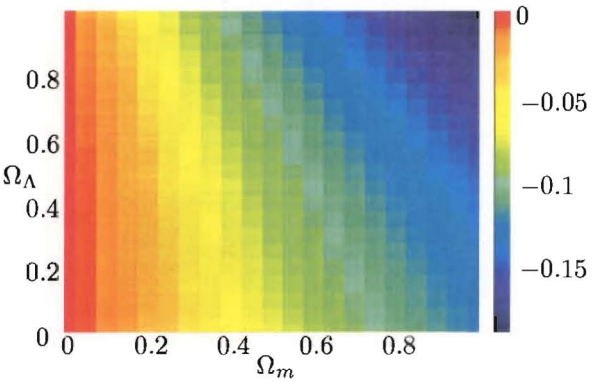

Figure 6.6: As for figure 6.5 but with $\alpha = 0.5$

magnitudes. We should therefore expect that when analysed with the modified Dyer-Roeder magnitude-redshift relationship rather than the FRW magnitude-redshift relationship, the supernovæ data will give different results for the most likely values of Ω_m and Ω_Λ. Since high values of Ω_Λ tend to make objects dimmer and the effect of implementing the modified Dyer-Roeder distance with low values of α is to make objects brighter, a lower value of Ω_Λ is likely to be necessary if the modified Dyer-Roeder magnitude is representative of the real magnitude. A higher value of Ω_m is also likely since the modified Dyer-Roeder magnitude calculation assumes that part of the matter content of the universe does not contribute to the evolution of magnitude with redshift.

The use of the modified Dyer-Roeder distance for cosmological parameter estimation from the supernovæ data will be discussed further in section 6.5.

6.4 Magnitude - redshift relationship

In section 6.2 we describe a method of calculating the magnitude-redshift relationship which takes account of a varying Ricci focusing component due to matter

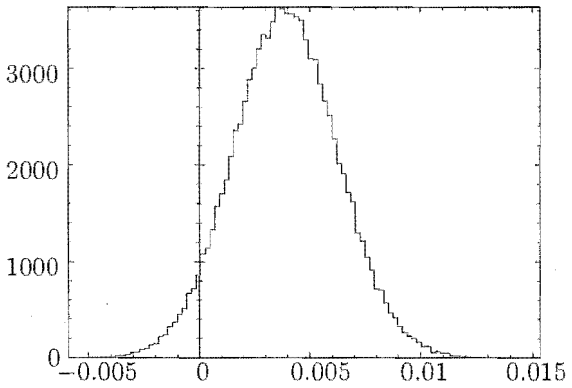

Figure 6.7: Histogram plot showing frequency of lensed magnitudes relative to the FRW magnitude at $z = 0.6$ for a $\{\Omega_m, \Omega_\Lambda\} = \{0.3, 0.7\}$ universe

inhomogeneities and a relationship between the affine parameter and the redshift which differs from the relationship in a FRW universe due to the local expansion rate of space depending on the local matter density. In this section the result of performing such calculations is compared with the FRW magnitude-redshift relationship and the dependence of the difference on the cosmological parameters is shown.

Since the method involves tracing a light path through a particular inhomogeneous matter distribution, an object at a given redshift may have a range of magnitudes. A typical distribution of lensed magnitudes at $z = 0.6$ and in a universe with the initial matter perturbations set at t_{CMB} to be $\mathcal{V}_{CMB} = 10^{-7}$ and with cosmological parameters $\{\Omega_m, \Omega_\Lambda\} = \{0.3, 0.7\}$ is shown in figure 6.7. The calculated magnitudes are binned and presented as a histogram plot. The horizontal axis is the magnitude difference between the lensed magnitude and the magnitude calculated in a FRW universe with the same cosmological parameters and the vertical axis is the frequency. The distribution falls to the right, indicating that the lensed magnitudes are predominantly dimmer than the FRW magnitude. The distribution of magnitudes is very close to a normal distribution and the standard deviation of the lensed magnitudes is of the same order as the deviation of the mean of the lensed magnitudes from the lensed magnitudes.

The distribution of lensed magnitudes depends on the cosmological parameters

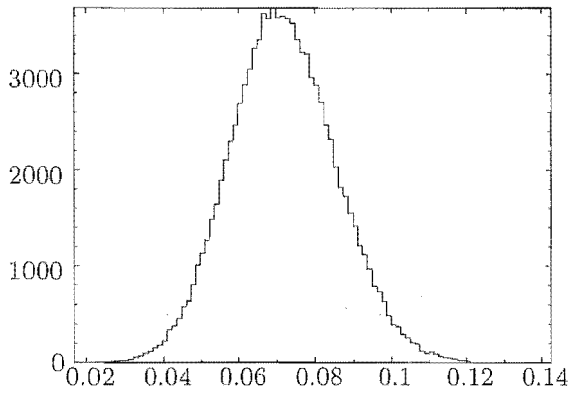

Figure 6.8: Histogram plot showing frequency of lensed magnitudes relative to the FRW magnitude at $z = 0.6$ for a $\{\Omega_m, \Omega_\Lambda\} = \{0.8, 1.7\}$ universe

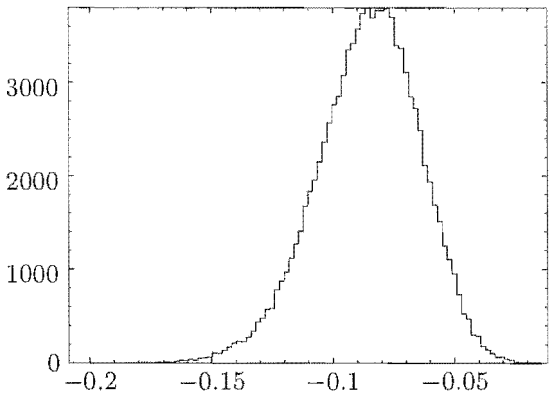

Figure 6.9: Histogram plot showing frequency of lensed magnitudes relative to the FRW magnitude at $z = 1.0$ for a $\{\Omega_m, \Omega_\Lambda\} = \{0.8, 1.7\}$ universe

and on the redshift, as may be seen from figures 6.8 and 6.9 which are calculated in a universe with $\{\Omega_m, \Omega_\Lambda\} = \{0.8, 1.7\}$ at $z = 0.6$ and $z = 1.0$ respectively. Lensing has had a much greater effect in this model, with the the standard deviation of the lensed magnitudes and the difference between the mean of the lensed magnitudes and the FRW magnitude both greater than the same quantities in figure 6.7. At the higher redshift lensing has magnified almost every lightpath, the opposite effect to that at the lower redshift.

The primary characteristics of the effect of gravitational lensing on the magnitudes of distant objects, that is, the deviation of the mean magnitude from the FRW magnitude and the standard deviation of the lensed magnitudes vary continuously with the cosmological parameters. The difference between the mean lensed magnitude and the FRW magnitude at $z = 0.6$ and $z = 1.0$ are shown in figures 6.10 and 6.11 for a grid of parameters, with Ω_m and Ω_Λ each varying between 0 and 1. At $z = 0.6$ the mean lensed magnitudes are greater than the FRW magnitudes for all combinations of parameters shown on the plot and the effect increases with both Ω_m and Ω_Λ. This is not the case at $z = 1.0$. Since the mean of the distribution used for $\widetilde{\theta}$ is slightly lower than the value used for the FRW calculation, the brightening effect present in the modified Dyer-Roeder also occurs to a small degree here. The lensing effect is also very small for the

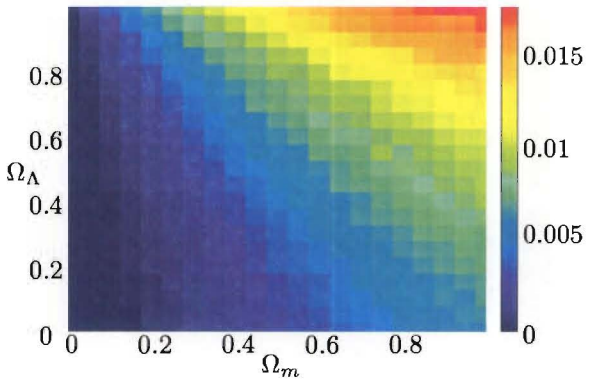

Figure 6.10: Difference between mean lensed magnitude and FRW magnitude at $z = 0.6$

Figure 6.11: Difference between mean lensed magnitude and FRW magnitude at $z = 1.0$

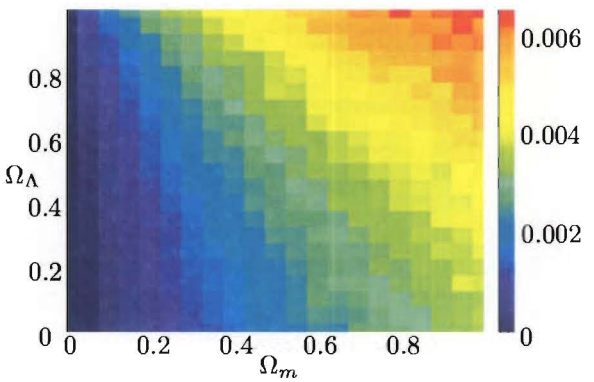

Figure 6.12: Standard deviation in m_{lensed} at $z = 0.6$

Figure 6.13: Standard deviation in m_{lensed} at $z = 1.0$

combinations of cosmological parameters shown so this slight inaccuracy in the calculation is enough to completely counteract the lensing at a redshift of $z = 1.0$.

Figure 6.12 shows the standard deviation of the observed magnitudes at $z = 0.6$ for each model on the grid and figure 6.13 is similar but calculated at $z = 1.0$. At both redshifts the standard deviation is greater for larger Ω_m in line with expectations. The standard deviations are smaller at the higher redshift. This is due to the light beams traversing a higher number of regions so the probability of any one light beam going through more overdense regions than underdense regions is lower, simply due to the central limit principle.

The lensed magnitudes calculated in this section are not substantially different

to the unlensed FRW magnitudes when Ω_m and Ω_Λ are between 0 and 1 and the differences are small compared to the uncertainties in the mean magnitudes in the binned supernovæ data. At higher values of Ω_m and Ω_Λ this is not necessarily the case, as figure 6.9 shows.

6.5 Cosmological parameter extraction with lensing

With initial matter density perturbations set at the CMB with $\mathcal{V}_{CMB} = 10^{-7}$ the differences between lensed magnitudes and unlensed magnitudes are small. When compared with the uncertainties in the supernovæ magnitude measurements, we should not expect lensing of the type discussed here to greatly affect the results obtained by the supernova experiments. There are three exceptions to this generalisation. Firstly, as figures 6.8 and 6.9 show, the intrinsic spread of magnitudes possible, called the model uncertainty, can become large with high values of Ω_Λ. High uncertainties will result in lower χ^2 values. Secondly, as figure 6.4 shows, the modified Dyer-Roeder magnitude is significantly different to the FRW magnitude for low values of α. Finally, if the initial matter density perturbations are large, with $\mathcal{V}_{CMB} > 10^{-7}$ then all the effects discussed in sections 6.3 and 6.4 become larger.

The importance of the model uncertainty at high values of Ω_Λ may be seen by comparing the magnitude-redshift plots in figures 6.14 and 6.15. Figure 6.14 is a magnitude plot showing the best overall fit with $\mathcal{V}_{CMB} = 10^{-6}$ which is at $\{\Omega_m, \Omega_\Lambda\} = \{0.32, 1.08\}$ as well as the FRW magnitude-redshift relationship for the same parameters and the FRW magnitude-redshift relationship for the best flat universe fit. The vertical lines with no endcaps are the 1σ model uncertainties and the plotted points represent the data bins. The curves are all very similar for most of the plot, only starting to significantly diverge above $z = 0.5$. The two FRW curves stay close and continue to stay close to the data points whereas the lensed magnitudes at high redshifts are lower than the data points. Due to the large uncertainties on the data points at high redshifts the discrepancy between the data and the lensed magnitudes does not contribute much to the

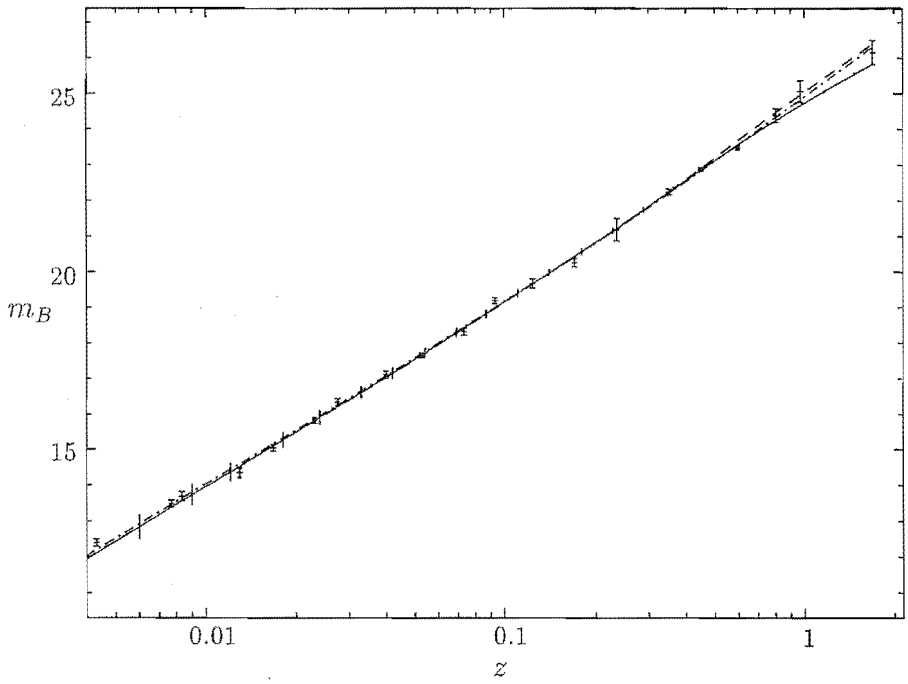

Figure 6.14: Magnitude-redshift plot showing the $\{\Omega_m, \Omega_\Lambda\} = \{0.32, 1.08\}$ lensed magnitudes (solid curve), the $\{\Omega_m, \Omega_\Lambda\} = \{0.32, 1.08\}$ FRW magnitudes (dashed curve) and the $\{\Omega_m, \Omega_\Lambda\} = \{0.34, 0.66\}$ FRW magnitudes (dotted dashed curve)

χ^2 statistic whereas the large model uncertainties on the lensed magnitudes at lower redshifts keeps the χ^2 statistic low. Every data point bar one is on the theoretical curve for lensed magnitudes to within the combined uncertainties. By way of comparison, figure 6.15 is a magnitude plot showing the best flat universe fit with $\mathcal{V}_{CMB} = 10^{-6}$ and the best FRW flat universe fit. The curves are very similar and the model uncertainties are much lower at the lower value of Ω_Λ. It is clear that the greatest effect from lensing on parameter estimation using χ^2 fitting is due to the model uncertainties at high Ω_Λ.

The magnitude-redshift relationship is calculated as described in section 6.2 over a grid of parameters and the χ^2 value calculated for each one according to (6.18). Table 6.1 shows the best fit parameters under a variety of different scenarios. The best fit parameters are calculated for values of $\mathcal{V}_{CMB}$ between 10^{-5} and 10^{-8} for both binned data points and raw data points and both including and ignoring the model uncertainty. Several different best fits are found for each scenario.

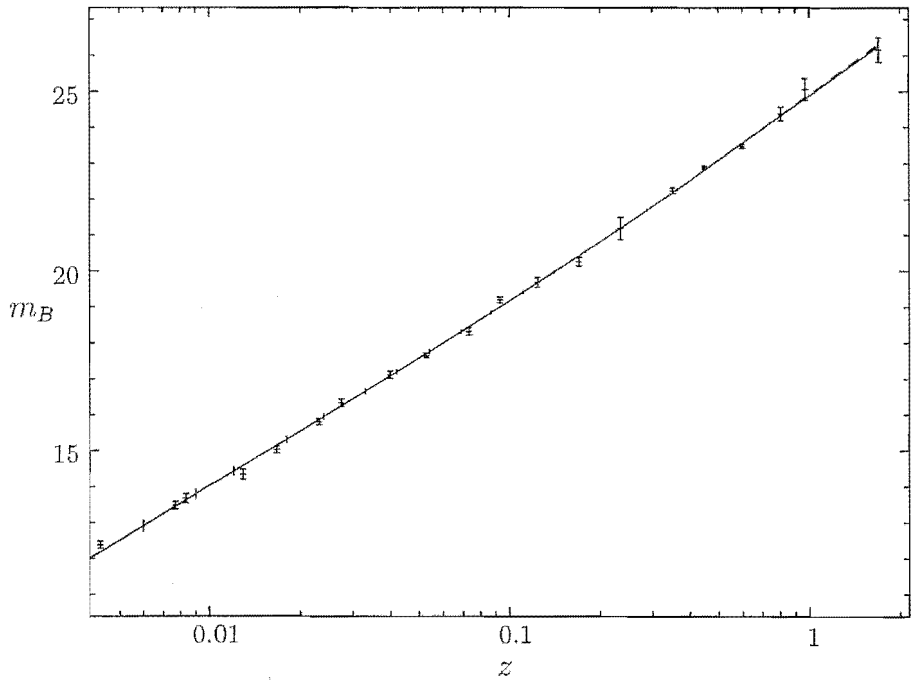

Figure 6.15: Magnitude-redshift plot showing the best fit flat curves with lensed magnitudes (solid curve) and FRW magnitudes (dashed curve)

The different fits found are the overall best fit, the best fit to a flat universe ($\Omega_m + \Omega_\Lambda = 1$) and the best fit to a universe with no cosmological constant ($\Lambda = 0$). For each best fit the normalised χ^2 value is shown.

The best $\Omega_\Lambda = 0$ fits are all at $\Omega_m = 0$ and since there is no lensing when there is no matter, all $\Omega_m = 0$ fits with the same number of free parameters have the same χ^2. With the exception of the high $\mathcal{V}_{CMB}$ scenario the best flat universe fits are all close to $\{\Omega_m, \Omega_\Lambda\} = \{0.35, 0.65\}$, indicating that the main result of Riess *et al.* (1998) and Perlmutter *et al.* (1998) is robust with respect to gravitational lensing of the form under consideration here. The overall best fit is moderately different for each scenario. In the FRW calculation, the precise location of the overall best fit is not considered to have great consequence as there is a large region in parameter space where the χ^2 values are very close and which contains both the overall best fit and the best fit to a flat universe. This is not the case here as when the model uncertainty is included in the χ computation the flat universe is a significantly poorer fit than the overall best fit for all but the lowest

	Best fit parameters $(\Omega_m, \Omega_\Lambda)$ and χ^2_ν						Model	
$\mathcal{V}_{CMB}$	Overall best fit		Flat universe		No Λ		uncertainty	Binned
10^{-5}	(0.20,0.80)	1.29	(0.20,0.80)	1.29	(0,0)	1.56	Yes	No
10^{-5}	(0.18,0.78)	0.71	(0.18,0.82)	0.75	(0,0)	1.83	Yes	Yes
10^{-5}	(0.16,0.66)	1.51	(0.18,0.82)	1.55	(0,0)	1.56	No	No
10^{-5}	(0.16,0.66)	1.53	(0.18,0.82)	1.76	(0,0)	1.83	No	Yes
10^{-6}	(0.34,1.12)	1.24	(0.30,0.70)	1.41	(0,0)	1.56	Yes	No
10^{-6}	(0.32,1.08)	0.66	(0.30,0.70)	1.03	(0,0)	1.83	Yes	Yes
10^{-6}	(0.30,0.70)	1.50	(0.30,0.70)	1.50	(0,0)	1.56	No	No
10^{-6}	(0.24,0.66)	1.49	(0.28,0.72)	1.49	(0,0)	1.83	No	Yes
10^{-7}	(0.62,1.64)	1.32	(0.36,0.64)	1.50	(0,0)	1.56	Yes	No
10^{-7}	(0.68,1.54)	0.95	(0.34,0.66)	1.46	(0,0)	1.83	Yes	Yes
10^{-7}	(0.48,0.90)	1.50	(0.36,0.64)	1.51	(0,0)	1.56	No	No
10^{-7}	(0.48,0.90)	1.44	(0.34,0.66)	1.50	(0,0)	1.83	No	Yes
10^{-8}	(0.60,1.00)	1.50	(0.36,0.64)	1.50	(0,0)	1.56	Yes	No
10^{-8}	(0.58,1.00)	1.43	(0.34,0.66)	1.49	(0,0)	1.83	Yes	Yes
10^{-8}	(0.60,1.00)	1.50	(0.36,0.64)	1.51	(0,0)	1.56	No	No
10^{-8}	(0.54,0.96)	1.45	(0.34,0.66)	1.49	(0,0)	1.83	No	Yes

Table 6.1: Best fit values of Ω_m and Ω_Λ overall; for a flat universe; and for a $\Omega_\Lambda = 0$ universe with lensing taken into account

values of $\mathcal{V}_{CMB}$.

The allowed regions of parameter space are heavily dependent on $\mathcal{V}_{CMB}$, as may be seen from figure 6.16 which is a contour plot showing 1σ to 4σ confidence regions calculated with the data put into 20 bins. The solid lines are the confidence regions obtained using the FRW magnitude-redshift relationship and are shown for comparison. The dashed lines are calculated with $\mathcal{V}_{CMB} = 10^{-5}$; the dotted-dashed lines are calculated with $\mathcal{V}_{CMB} = 10^{-6}$; the dotted lines are calculated with $\mathcal{V}_{CMB} = 10^{-7}$; and the dot-dot-dot-dashed lines are calculated with $\mathcal{V}_{CMB} = 10^{-8}$. Lower values of $\mathcal{V}_{CMB}$ than 10^{-8} result in confidence regions indistinguishable from the FRW plot. Figure 6.17 is similar to figure 6.16 but the χ^2 values are calculated without taking the model uncertainty into account.

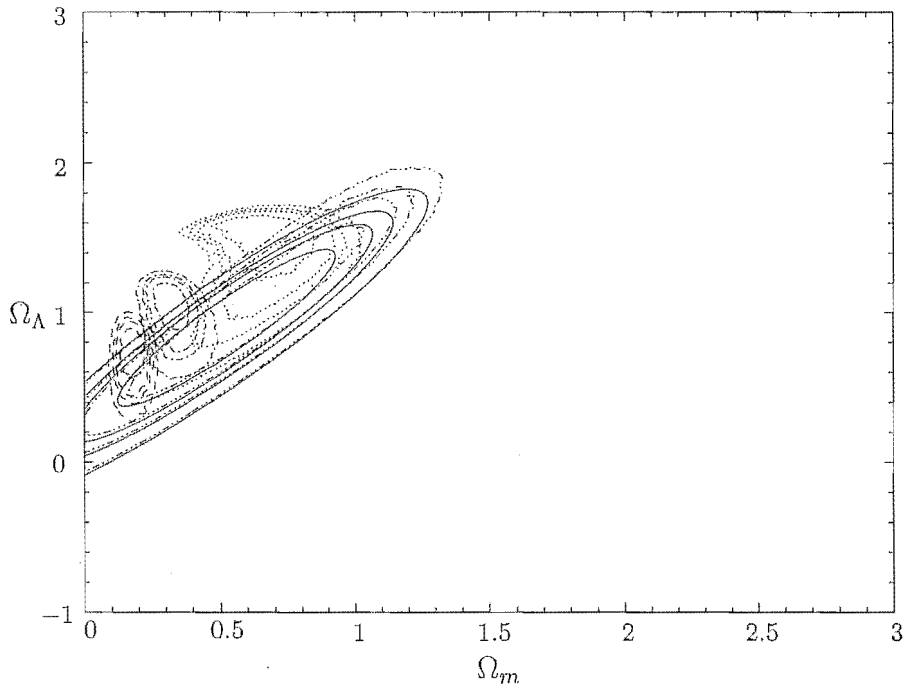

Figure 6.16: Contour plot showing 1σ to 4σ confidence regions for Ω_m and Ω_Λ calculated using lensed magnitudes with various values for $\mathcal{V}_{CMB}$

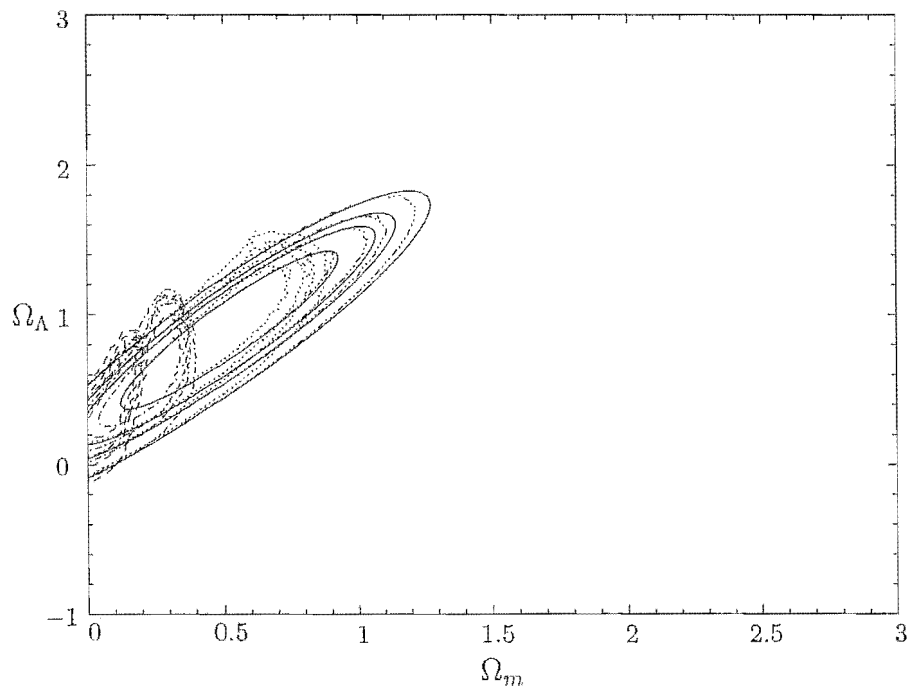

Figure 6.17: As for figure 6.16 but not including model uncertainties in the χ^2 calculation

Comparing figures 6.16 and 6.17 allows us to separate the two different influences on the confidence regions. Firstly, matter inhomogeneities affect the mean observed magnitude of objects at given redshift. Secondly, there is an inherent uncertainty in calculating the theoretical magnitude of an object at a given redshift due to light paths undergoing gravitational lensing to a differing degree. Figure 6.17 shows contour plots calculated without taking the model uncertainty into account. Close to $\Omega_m = 0$ the contours are very similar to the FRW contours as there is no lensing with no matter. The lensed contours are smaller than the FRW contours, especially for high values of $\mathcal{V}_{CMB}$. If $\mathcal{V}_{CMB}$is large, high values of Ω_m are ruled out which are accepted in the analysis using the FRW magnitude-redshift relationship. Figure 6.16 is quite different, as models with high values of Ω_m and Ω_Λ have higher model uncertainties and therefore tend to have lower χ^2 values. Low values of Ω_m and Ω_Λ are ruled out at a high confidence level for high values of $\mathcal{V}_{CMB}$ and a flat universe is ruled out at 3σ for $\mathcal{V}_{CMB} = 10^{-6}$ and more than 4σ for $\mathcal{V}_{CMB} = 10^{-7}$. The confidence regions are small, being heavily dominated by the area of parameter space where the model fits the data moderately well and where the model uncertainties are also large.

The magnitude-redshift relationship is also calculated using the modified Dyer-Roeder distance over a grid of parameters and the χ^2 value calculated for each one according to (6.18). This is done for the values of $\mathcal{V}_{CMB}$ which appear to best represent our universe, that is $\mathcal{V}_{CMB} = 10^{-6}$ and $\mathcal{V}_{CMB} = 10^{-7}$, and for several values of α. The results are shown in figures 6.18 to 6.21 and table 6.2. Table 6.2 shows the best fit parameters under a variety of different scenarios. The best fit parameters are found for values of α from 0.5 to 0.9; for both binned data points and raw data points; and both including and ignoring the model uncertainty. Two different best fits are shown for each scenario, the overall best fit and the best fit to a flat universe. The best fit to a universe with no cosmological constant in each scenario is $\Omega_m = 0$ as it is in table 6.1. For each best fit the normalised χ^2 value is shown. The best flat universe fits are again moderately close to $\{\Omega_m, \Omega_\Lambda\} = \{0.35, 0.65\}$ although with the lower values for α, a higher Ω_m of around 0.4 is favoured.

		Best fit parameters $(\Omega_m, \Omega_\Lambda)$ and χ^2_ν				Model	
$\mathcal{V}_{CMB}$	α	Overall best fit		Flat universe		uncertainty	Binned
10^{-6}	0.9	(0.34,1.18)	1.24	(0.36,0.64)	1.42	Yes	No
10^{-6}	0.9	(0.32,1.12)	0.63	(0.34,0.66)	1.09	Yes	Yes
10^{-6}	0.9	(0.32,1.02)	1.50	(0.32,0.68)	1.50	No	No
10^{-6}	0.9	(0.32,1.02)	1.47	(0.32,0.68)	1.50	No	Yes
10^{-6}	0.7	(0.46,1.30)	1.22	(0.40,0.60)	1.44	Yes	No
10^{-6}	0.7	(0.42,1.22)	0.58	(0.32,0.68)	1.17	Yes	Yes
10^{-6}	0.7	(0.36,0.78)	1.51	(0.32,0.68)	1.51	No	No
10^{-6}	0.7	(0.36,0.90)	1.51	(0.32,0.68)	1.53	No	Yes
10^{-6}	0.5	(0.68,1.60)	1.20	(0.42,0.58)	1.46	Yes	No
10^{-6}	0.5	(0.60,1.42)	0.56	(0.42,0.58)	1.25	Yes	Yes
10^{-6}	0.5	(0.42,0.92)	1.51	(0.36,0.64)	1.52	No	No
10^{-6}	0.5	(0.42,0.92)	1.49	(0.36,0.64)	1.57	No	Yes
10^{-7}	0.9	(0.64,1.70)	1.26	(0.38,0.62)	1.50	Yes	No
10^{-7}	0.9	(0.70,1.60)	0.81	(0.34,0.66)	1.47	Yes	Yes
10^{-7}	0.9	(0.64,1.02)	1.50	(0.36,0.64)	1.51	No	No
10^{-7}	0.9	(0.60,1.02)	1.45	(0.34,0.66)	1.50	No	Yes
10^{-7}	0.7	(0.68,1.84)	1.19	(0.40,0.60)	1.51	Yes	No
10^{-7}	0.7	(0.76,1.80)	0.59	(0.38,0.62)	1.51	Yes	Yes
10^{-7}	0.7	(0.86,1.32)	1.50	(0.38,0.62)	1.51	No	No
10^{-7}	0.7	(0.86,1.32)	1.43	(0.38,0.62)	1.54	No	Yes
10^{-7}	0.5	(1.06,2.18)	1.16	(0.44,0.56)	1.52	Yes	No
10^{-7}	0.5	(0.96,2.06)	0.48	(0.40,0.60)	1.55	Yes	Yes
10^{-7}	0.5	(1.18,1.46)	1.50	(0.44,0.56)	1.52	No	No
10^{-7}	0.5	(1.18,1.46)	1.46	(0.40,0.60)	1.57	No	Yes

Table 6.2: Best fit values of Ω_m and Ω_Λ overall and for a flat universe calculated according to the modified Dyer-Roeder distance

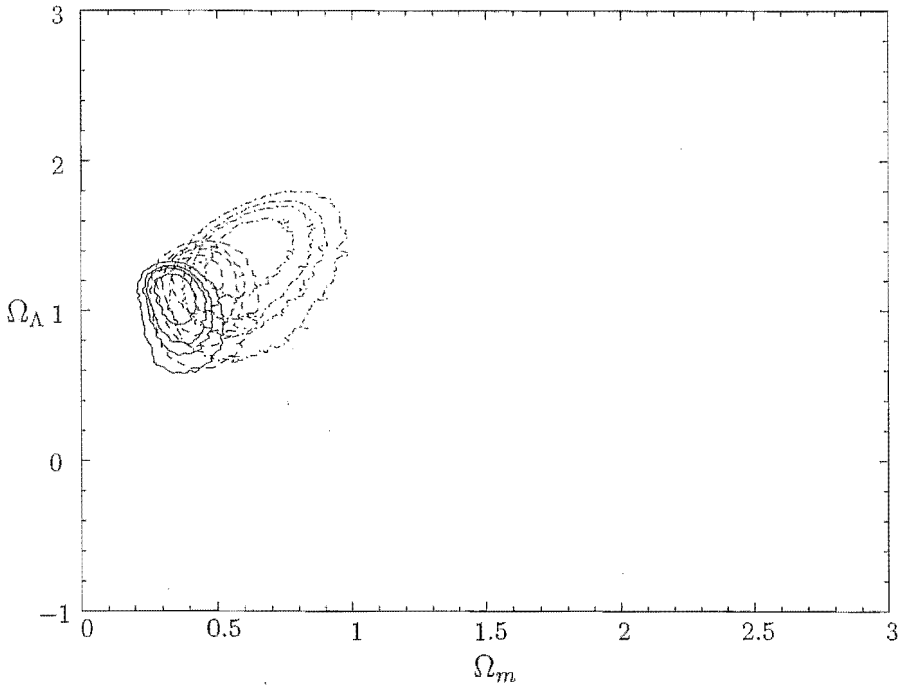

Figure 6.18: Contour plot showing 1σ to 4σ confidence regions for Ω_m and Ω_Λ calculated using the modified Dyer-Roeder distance with various values for α and with $\mathcal{V}_{\mathcal{CMB}} = 10^{-6}$

The allowed regions of parameter space calculated using the modified Dyer-Roeder distance are heavily dependent on both α and $\mathcal{V}_{\mathcal{CMB}}$. A relatively high value of $\mathcal{V}_{\mathcal{CMB}} = 10^{-6}$ results in small confidence regions as may be seen in figure 6.18, whereas a relatively low value of $\mathcal{V}_{\mathcal{CMB}} = 10^{-7}$ results in large confidence regions (figure 6.20). Both scenarios rule out low values of both Ω_m and Ω_Λ at a confidence level of greater than 4σ with even a flat universe disfavoured. In each plot the solid lines are calculated with $\alpha = 0.9$; the dashed lines are calculated with $\alpha = 0.7$; and the dotted-dashed lines are calculated with $\alpha = 0.5$. As α decreases the allowed regions of parameter space increase with higher values of Ω_m preferred. This is not unexpected as the lower α is, the less Ω_m contributes to the calculation of the magnitude-redshift relationship. The lensing effect in the modified Dyer-Roeder distance manifests itself mostly through the model uncertainty, as can be seen in figures 6.19 and 6.21 in which the model uncertainty has been ignored. The confidence regions are similar to the FRW confidence regions although higher values of Ω_m are again preferred for low α.

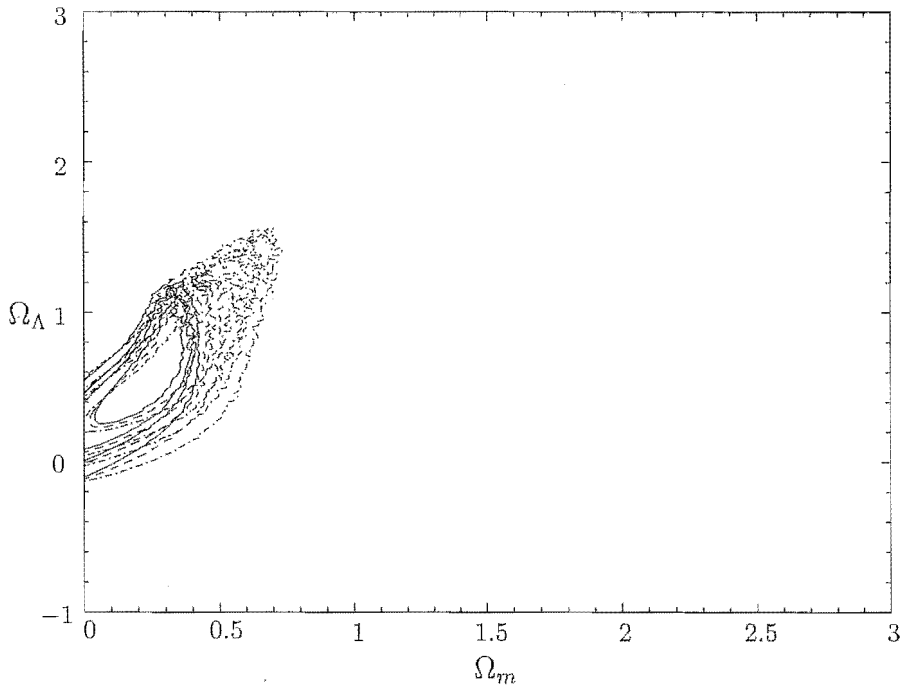

Figure 6.19: As for figure 6.18 but not including model uncertainties in the χ^2 calculation

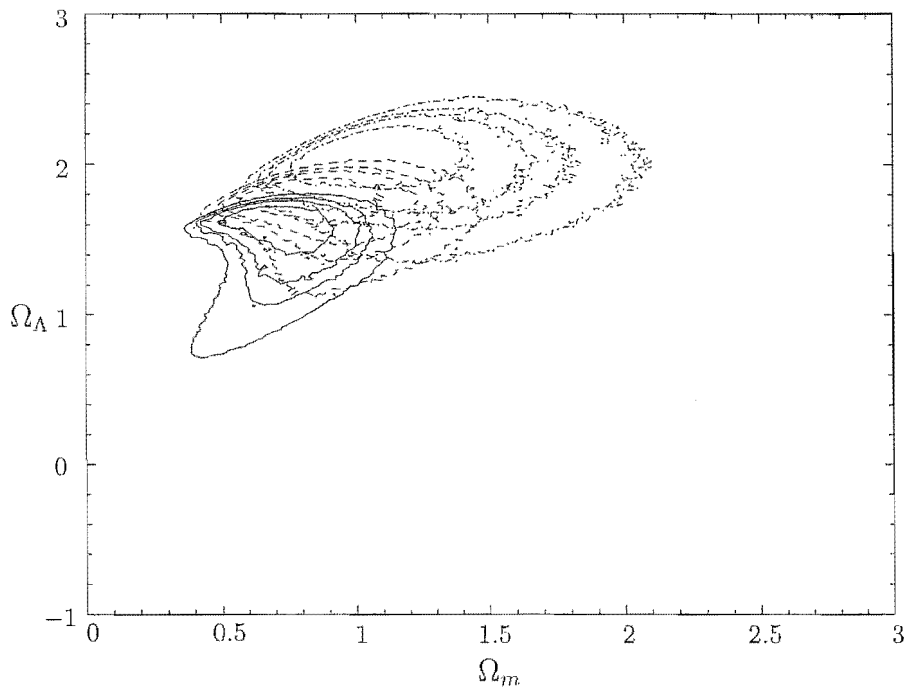

Figure 6.20: Contour plot showing 1σ to 4σ confidence regions for Ω_m and Ω_Λ calculated using the modified Dyer-Roeder distance with various values for α and with $\mathcal{V}_{CMB} = 10^{-7}$

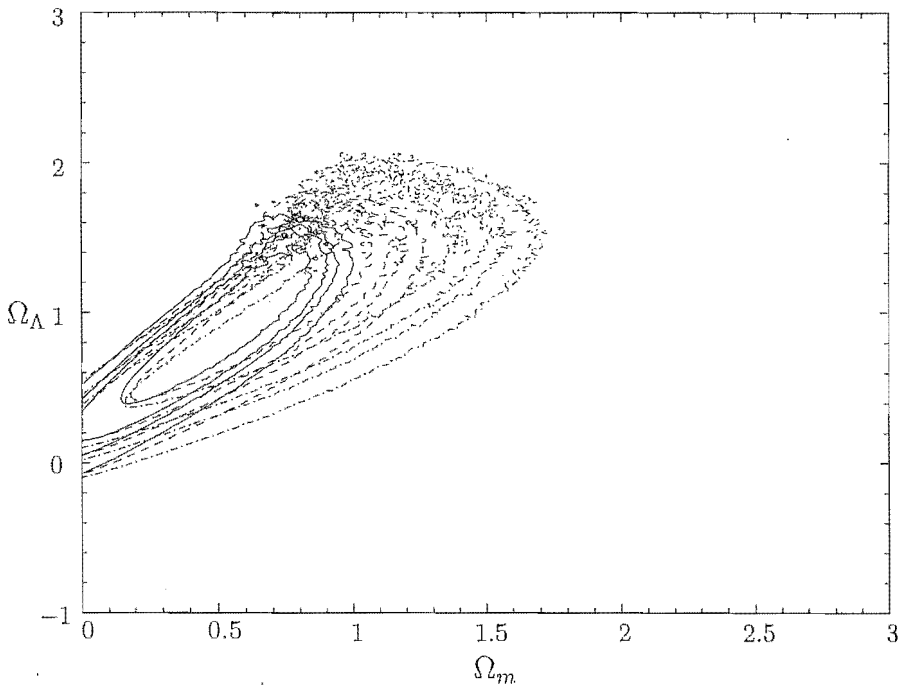

Figure 6.21: As for figure 6.20 but not including model uncertainties in the χ^2 calculation

6.6 Conclusions

A magnitude-redshift relationship has been developed which takes into account the local expansion rate of space being dependent on the local matter density. This lensed magnitude-redshift relationship was found to be only marginally different to the unlensed relationship if the cosmological parameters Ω_m and Ω_Λ are between 0 and 1 and the distribution of lensed magnitudes is narrow. If Ω_Λ is large, the lensed magnitudes may be different to the unlensed magnitudes by about 0.1 magnitudes and the distribution of magnitudes is broader. The effect of inhomogeneities is in general greatest at low redshift, in contrast to Holz and Wald (1998) and Bergström *et al.* (2000). These studies are complementary to the method and results presented in this chapter as they investigate lensing effects not considered here – the effect of shear and of strong Ricci focusing.

When used to estimate cosmological parameters in conjunction with the supernovæ data, scenarios with high Ω_Λ dominate the confidence region plots. The

most likely flat universe found here is not significantly different to the most likely flat universe found by Riess *et al.* (1998) and Perlmutter *et al.* (1998) but the likelihood that the universe is flat is found to be low according to the lensed magnitude-redshift relationship.

The assumptions behind the Dyer-Roeder distance, namely that a fraction of the matter in the universe is bound in clumps and therefore does not affect weak gravitational lensing, were re-examined and a modified Dyer-Roeder distance developed that incorporates a density dependent expansion rate of space. The modified Dyer-Roeder distance differs less from the FRW relationship than does the unmodified Dyer-Roeder distance. If the proportion of matter bound in clumps is high and the modified Dyer-Roeder distance is used to estimate cosmological parameters then the most likely flat universe is found to have a matter content slightly higher than that found by Riess *et al.* (1998) and Perlmutter *et al.* (1998).

Under no circumstances considered here is the primary finding of Riess *et al.* (1998) and Perlmutter *et al.* (1998), that our universe appears to have a non-zero cosmological constant, brought into doubt.

Chapter 7

Conclusions

Recent observations of high redshift supernovæ have allowed a tremendous breakthrough in extracting information about the make-up of the universe. In this thesis we were principally concerned with the effects of taking into account the inhomogeneity of the universe on these results.

We have shown that a perturbed FRW universe which has the same global behaviour as an exact FRW universe does not have the same light propagation behaviour. This is due to the relationship between redshift and the radial coordinate being influenced by the inhomogeneities introduced. While other authors have come to the same conclusions, the method by which the result is arrived at here benefits from its extreme simplicity. The effect of inhomogeneities on the redshift of distant objects has not been studied as extensively as the influence of inhomogeneities on the magnitude of distant objects. We have shown that it is advantageous to study both effects concurrently. The change in redshift along a light beam depends on the rate of expansion of space so an understanding of the effect of inhomogeneities on the local rate of expansion of space is necessary in order to study the effect of inhomogeneities on redshift.

Taking into account a non-uniform expansion rate of space, we have developed a new method of calculating the relationship between the angular diameter distance and the redshift of a distant object. The method results in magnitudes that are little different to the FRW magnitude for moderate cosmological parameters at a redshift of $z = 1$. At high Ω_Λ the magnitude differences can be significant. The

predicted magnitude of a distant object in an inhomogeneous universe should not be a single number but rather a range of numbers that encompass the possibilities. The spread of expected magnitudes at moderate cosmological parameters is small and at high Ω_Λ the spread of expected magnitudes is significant.

We have used the new magnitude-redshift relationship in conjunction with the supernovæ data to estimate cosmological parameters and found that

- to a high level of confidence Ω_Λ is non-zero
- the most likely flat universe is one with cosmological parameters close to $\{\Omega_m, \Omega_\Lambda\} = \{0.3, 0.7\}$.

The method introduced here for calculating the magnitude-redshift relationship considers different effects to the method presented in Holz and Wald (1998). The two methods are well suited to being combined and there are clear benefits to doing so. The method of Holz and Wald incorporates the effect of an occasional Weyl focusing (shear) and Ricci focusing "kick" but ignores the effect of inhomogeneities on the redshift whereas the method presented here ignores shear but incorporates the effect of inhomogeneities on redshift. They are well suited to being combined as they both divide the universe into regions which may have differing average densities and solve the light propagation equations across those regions.

In order to investigate the effect of a non-uniform expansion rate, a new description of the evolution of matter fluctuations in the weakly non-linear regime was developed which features not only the matter distribution but also a relationship between the matter density and the local expansion rate of space. It was shown that the matter distribution is close to a log-normal distribution which has a number of both theoretical and observational justifications (Coles and Jones, 1991).

It was noted that the available supernova magnitude-redshift data covers poorly the redshift region $0.1 \lesssim z \lesssim 0.3$. We have shown by simulating the effect of gathering additional data in this region that it is unlikely that observing more intermediate redshift supernovæ will result in tighter constraints on the cosmo-

logical parameters Ω_m and Ω_Λ.

The effect of inhomogeneities on the redshift of distant objects is not large enough to influence the results of current cosmological experiments. As cosmology becomes a more high-precision science, smaller effects will need to be considered and our view of lensing must widen to encompass the effect of inhomogeneities on the redshift of distant objects.

Bibliography

Bergström, L., Goliath, M., Goobar, A. and Mörtsell, E., *Astronom. and Astrophys.* **358**:13, 2000.

Bevington, P. R. and Robinson, D. K., *Data Reduction and Error Analysis for the Physical Sciences* (McGraw-Hill, New York, 1992), second edition.

Boersma, J., *Phys. Rev. D (3)* **57**:798, 1998.

Buchert, T., *Gen. Rel. Grav.* **32**:105, 2000.

Carroll, S. M., Press, W. H. and Turner, E. L., *Annual Review of Astronomy and Astrophysics* **30**:499, 1992.
URL `http://nedwww.ipac.caltech.edu/level5/Carroll/frames.html`

Claudel, C., *Proc. Roy. Soc. London Ser. A* **465**:1455, 2000.

Coles, P. and Jones, B., *Monthly Notices Roy. Astronom. Soc.* **248**:1, 1991.

Dyer, C. C. and Roeder, R. C., *Astrophys. J.* **174**:L115, 1972.

Ellis, G. F. R., Bassett, B. A. C. C. and Dunsby, P. K. S., *Class. Quantum Grav.* **15**:2345, 1998.

Hamuy, M., Phillips, M. M., Maza, J., Suntzeff, N. B., Schommer, R. A. and Aviles, R., *Astronom. J.* **109**:1, 1995.

Hawking, S. W. and Ellis, G. F. R., *The Large Scale Structure of Space-Time*, Cambridge Monographs on Mathematical Physics (Cambridge University Press, London, 1973).

Hogg, D. W., *astro-ph/9905116* , 1999.
URL `http://arxiv.org/abs/astro-ph/9905116`

Holz, D. E. and Wald, R. M., *Phys. Rev. D (3)* **58**:63501, 1998.

Hubble, E., *Proceedings of the National Academy of Science* **15**:168, 1929.

Kantowski, R., *Astrophys. J.* **155**:89, 1969.

Kantowski, R. and Thomas, R. C., *Astrophys. J.* **561**:491, 2001.

Kantowski, R., Vaughan, T. and Branch, D., *Astrophys. J.* **447**:35, 1995.

Kochanek, C., *Astrophys. J.* **419**:12, 1993.

Krasiński, A., *Inhomogeneous Cosmological Models* (Cambridge University Press, 1997).

Kurki-Suonio, H. and Liang, E., *Astrophys. J.* **390**:5, 1992.

Lake, K., *Astrophys. J.* **401**:L1, 1992.

Linder, E. V., *astro-ph/9801122* , 1998.
URL `http://arxiv.org/abs/astro-ph/9801122`

Mavrides, S., *Monthly Notices Roy. Astronom. Soc.* **177**:709, 1976.

Moffat, J. and Tatarski, D., *Phys. Rev. D (3)* **45**:3512, 1992.

Mörtsell, E., Goobar, A. and Bergström, L., *Astrophys. J.* **559**:53, 2001.

Mustapha, N., Bassett, B. A., Hellaby, C. and Ellis, G. F. R., *Class. Quant. Grav.* **15**:2363, 1998.

Netterfield, C. B., Ade, P. A. R., Bock, J. J., Bond, J. R., Borrill, J., Boscaleri, A., Coble, K., Contaldi, C. R., Crill, B. P., de Bernardis, P., Farese, P., Ganga, K., Giacometti, M., Hivon, E., Hristov, V. V., Iacoangeli, A., Jaffe, A. H., Jones, W. C., Lange, A. E., Martinis, L., Masi, S., Mason, P., Mauskopf, P. D., Melchiorri, A., Montroy, T., Pascale, E., Piacentini, F., Pogosyan, D., Pongetti, F., Prunet, S., Romeo, G., Ruhl, J. E. and Scaramuzzi, F., *Astrophys. J.* **571**:604, 2002.

Nottale, L., *Astronom. and Astrophys.* **110**:9, 1982.

Nusser, A. and Haehnelt, M., *Monthly Notices Roy. Astronom. Soc.* **303**:179, 1999.

Padmanabhan, T., *Structure Formation in the Universe* (Cambridge University Press, Cambridge, New York, 1993).

Peacock, J., *Cosmological Physics* (Cambridge University Press, Cambridge, UK, 1999).

Peacock, J. A. and Dodds, S. J., *Monthly Notices Roy. Astronom. Soc.* **280**:L19, 1996.

Peebles, P., *Principles of Physical Cosmology*, Princeton Series in Physics (Princeton University Press, Princeton New Jersey, 1993).

Perlmutter, S., Aldering, G., Goldhaber, G., Knop, R. A., Nugent, P., Castro, P. G., Deustua, S., Fabbro, S., Goobar, A., Groom, D. E., Hook, I. M., Kim, A. G., Kim, M. Y., Lee, J. C., Nunes, N. J., Pain, R., Pennypacker, C. R., Quimby, R., Lidman, C., Ellis, R. S., Irwin, M., McMahon, R. G., Ruiz-Lapuente, P., Walton, N., Schaefer, B., Boyle, B. J., Filippenko, A. V., Matheson, T., Fruchter, A. S., Panagia, N., Newberg, H. J. M., Couch, W. J. and Project, T. S. C., *Astrophys. J.* **517**:565, 1998.

Press, W. H., *Numerical Recipes in C: the Art of Scientific Computing* (Cambridge University Press, New York, 1992), second edition.

Riess, A. G., Press, W. H. and Kirshner, R. P., *Astrophys. J.* **473**:88, 1996.

Riess, A. G., Filippenko, A. V., Challis, P., Clocchiatti, A., Diercks, A., Garnavich, P. M., Gilliland, R. L., Hogan, C. J., Jha, S., Kirshner, R. P., Leibundgut, B., Phillips, M. M., Reiss, D., Schmidt, B. P., Schommer, R. A., Smith, R. C., Spyromilio, J., Stubbs, C., Suntzeff, N. B. and Tonry, J., *Astronom. J.* **116**:1009, 1998.

Riess, A. G., Nugent, P. E., Gilliland, R. L., Schmidt, B. P., Tonry, J., Dickinson, M., Thompson, R. I., Budavári, T., Casertano, S., Evans, A. S., Filippenko,

A. V., Livio, M., Sanders, D. B., Shapley, A. E., Spinrad, H., Steidel, C. C., Stern, D., Surace, J. and Veilleux, S., *Astrophys. J.* **560**:49, 2001.

Rose, H. G., *Astrophys. J.* **560**:L15, 2001.

Sasaki, M., *Monthly Notices Roy. Astronom. Soc.* **228**:653, 1987.

Schmidt, B. P., Suntzeff, N. B., Phillips, M. M., Schommer, R. A., Clocchiatti, A., Kirshner, R. P., Garnavich, P., Challis, P., Leibundgut, B., Spyromilio, J., Riess, A. G., Filippenko, A. V., Hamuy, M., Smith, R. C., Hogan, C., Stubbs, C., Diercks, A., Reiss, D., Gilliland, R., Tonry, J., Maza, J., Dressler, A., Walsh, J. and Ciardullo, R., *Astrophys. J.* **507**:46, 1998.

Schneider, P. and Weiss, A., *Astrophys. J.* **330**:1, 1988.

Schneider, P., Ehlers, J. and Falco, E., *Gravitational Lenses*, A&A library (Springer-Verlag, New York, 1992).

Sugiura, N., Nakao, K.-I. and Harada, T., *Phys. Rev. D (3)* **60**:103508, 1999.

Tomita, K., *Progr. Theoret. Phys.* **106**:929, 2001a.

Tomita, K., *Monthly Notices Roy. Astronom. Soc.* **326**:287, 2001b.

Tomita, K., Premadi, P. and Nakamura, T. T., *Progr. Theoret. Phys. Suppl.* **133**:85, 1999.

Turner, E. L., Cen, R. and Ostriker, J. P., *Astronom. J.* **103**:1427, 1992.

Wald, R. M., *General Relativity* (University of Chicago Press, Chicago, 1984).

Wambsganss, J., Cen, R. and Ostriker, J. P., *Astrophys. J.* **494**:29, 1998.

Wang, Y., *Astrophys. J.* **536**:531, 2000.

Weinberg, S., *Gravitation and Cosmology: Principles and Applications of the General Theory of Relativity* (Wiley, New York, 1972).

Weinberg, S., *Astrophys. J.* **208**:L1, 1976.

Wu, X., *Astronom. and Astrophys.* **239**:29, 1990.

Zech, G., *EPJdirect C* 4(12):1, 2002.
URL `http://tinyurl.com/3f4s`

Zotov, N. and Stoeger, W., *Class. Quantum Grav.* **9**:1023, 1992.